O. Y. Usikov Institute for RadioPhysics and Electronics
National Academy of Sciences of Ukraine

Qualifying research work in the form of manuscript

FEDIR O. YEVTUSHENKO

UDC 537.86: 535.417.2

DISSERTATION

RESONANT SCATTERING AND ABSORPTION OF ELECTROMAGNETIC WAVES BY INFINITE GRATINGS OF GRAPHENE STRIPS ON DIELECTRIC SUBSTRATES

104 – Physics and Astronomy
10 - Natural Sciences

submitted in partial fulfillment of the requirements
for the degree Doctor of Philosophy

The dissertation contains the results of original research of the author. The use of ideas, results and texts of other authors is accompanied with corresponding references.

_____ F.O. Yevtushenko

Supervisors: S.V. Dukhopelnykov, Candidate of Technical Sciences, Senior Researcher and K.V. Ilyenko, Candidate of Physical and Mathematical Sciences, Senior Researcher

Kharkiv – 2023

ABSTRACT

Yevtushenko F.O. **Resonant scattering and absorption of electromagnetic waves by infinite gratings of grapheme strips on dielectric substrates. –** Qualifying research work in the form of a manuscript.

This thesis is submitted in fulfillment of conditions for obtaining the degree of Doctor of Philosophy in specialization #104 – Physics and Astronomy (10 - Natural Sciences). - O. Y. Usikov Institute for RadioPhysics and Electronics NAS of Ukraine, Kharkiv, 2023.

The thesis undertakes a comprehensive theoretical analysis of the scattering, absorption and emission of electromagnetic waves by infinite gratings of graphene strips lying on dielectric substrates. The practical significance of this research lies in its implications for electromagnetic-wave devices and systems working in the terahertz, infrared, and visible-light ranges. In this connection, the appearance of graphene has opened many new and exciting opportunities. This is because graphene has high electron mobility, controlled with the aid of DC biasing (via the graphene chemical potential), and displays plasmonic effects.

The goal of the work is, first, the study of resonance effects in the H- and E-polarized electromagnetic wave scattering and absorption by infinite grating of graphene strips lying on dielectric substrate. Such a metasurface is expected to behave as a composite periodic open resonator. Its high frequency selectivity follows from the existence of three types of natural modes: low-Q slab modes and ultrahigh-Q lattice modes, which exist in either polarization provided that the substrate is present, and moderate-Q plasmon modes of graphene strips that appear only in the H-polarization. Second, another important goal is to study the threshold conditions for the H- and E-polarized lasing modes of infinite flat grating of graphene strips lying on the gain-material substrate. Here, special attention is paid to the tunability of the plasmon modes and ultrahigh-Q lattice modes with the aid of graphene’s chemical potential.

To achieve these goals, the following **tasks are considered:**

- Derivation of the well-conditioned matrix equations for the plane wave scattering and absorption by infinite grating made of zero-thickness graphene strips placed on dielectric substrate in the cases of the E- and H-polarizations. This derivation is based on the full-wave formulation of the corresponding boundary value problems of the wave scattering. The matrix equations obtained yield the basis of the numerical algorithms.

- Writing and testing the full-wave meshless codes in the Matlab environment and validating them by comparison with the published earlier results of the other convergent numerical methods, when available.

- Study of the behavior of the computational error depending on the order of truncation of the matrix equations, to confirm the convergence of the algorithms and visualize the effect of various parameters on the rate of convergence.

- Systematic use of the developed computer codes for the analysis of the scattering and absorption characteristics of the considered graphene-strip metasurfaces, especially their tunability with the aid of graphene's chemical potential.

- Derivation of approximate formulas for the frequencies and Q-factors of the plasmon, lattice and dielectric substrate modes.

- Adapting the derived well-conditioned matrix equations to the case of substrate, maid of the gain material. Combining these equations with iterative search of the roots of determinantal equations. Systematic full-wave analysis of threshold conditions for the modes of infinite graphene strip grating located on gain-material substrate in the cases of the E- and H-polarizations.

At the preliminary step, the study deals with auxiliary problems of the plane E and H-polarized wave scattering from an infinite flat grating of the perfectly electrically conducting (PEC) zero-thickness strips, placed on the interface of a dielectric slab. Following the approach first developed in the 1960s, we reduce this problem, for either polarization, to a dual series equation (DSE) for the complex amplitudes of the scattered field Floquet spatial harmonics. Then we perform analytical regularization of this equation, based on the inversion of the static part of the problem, associated with

grating in free space, with the aid of the Riemann-Hilbert Problem (RHP) technique. In each case, this yields Fredholm second-kind infinite matrix equation, numerical solution of which has a guaranteed convergence. We cast these equations to the form, convenient for computations. Then, we perform numerical experiments demonstrating how the rate of convergence of our meshless code depends on the thickness and dielectric permittivity of the slab. The scattering characteristics reveal the resonances on the slab modes and the lattice modes of the whole grating as a periodic open resonator.

Subsequently, the investigation extends to the scattering of the E and H-polarized plane waves by the similar grating however with graphene strips on the surface of a dielectric-slab substrate. The complex conductivity of graphene is modelled using the Kubo formulas. Due to finite conductivity, the boundary conditions on the strips turn to the two-side resistive conditions. In the case of the H-polarization, our treatment is based on the analytical semi-inversion, using the RHP solution, thus it is a modification of the PEC-strip regularization. However, in the case of the E-polarization, the RHP technique is not applicable. Instead, we make analytical regularization using the Inverse Discrete Fourier Transform (IDFT). These techniques are known since the 2000s for the free standing imperfect strip gratings, however, we adapt them to the case of on-substrate strip grating. In the either polarization, we obtain a Fredholm 2-nd kind matrix equation for the Floquet harmonic amplitudes that guarantees the convergence of the full-wave meshless codes based on these equations. The computational error can be controlled and reduced even to machine precision. In either polarization, the matrix elements involve only elementary functions and therefore the codes are not only accurate but very economic. Using such a trusted instrument, we perform detailed numerical analysis of the wave scattering and absorption and focus on the rich interplay between the resonances on various natural modes. In the case of the H-polarization, new phenomenon, with respect to the PEC-strip grating, is the existence of the plasmon modes of graphene strips. Their frequencies are tunable in wide range (within a factor of two or three) with the aid of the graphene's chemical potential. In both polarizations, we demonstrate multiple ultrahigh-Q resonances on the lattice modes, which do not exist in

the absence of the substrate and are caused, jointly, by the periodicity and the existence of the guided waves of the substrate. New effect is the regime of the electromagnetically induced transparency, which takes place when enhanced reflection at the plasmon resonance is spoiled by the quasi-total transmission in the sharp lattice-mode resonance.

Finally, the thesis explores the threshold conditions for the H and E-polarized lasing modes of the graphene-strip grating on substrate. The substrate material is assumed to have the gain that offsets the radiation and ohmic losses and allows the modes to reach the lasing threshold. We look for the frequency and the gain-index threshold value, specific to each mode, as eigenvalues. To find them, we reduce the field problem to a DSE for the complex amplitudes of the Floquet spatial harmonics, which we analytically regularize using the RHP technique in the H-mode case and IDFT in the E-mode case. In the either case, this yields a Fredholm second-kind infinite determinantal equation for the eigenvalues. Increasing the matrix truncation number guarantees the convergence of these quantities to their exact values.

The following **new scientific results** have been obtained in the work:

- In the plane-wave scattering, we have visualized the rate of convergence of the corresponding numerical algorithms and its dependence on various parameters of the substrate and the grating, including the graphene parameters.

- Our computations have shown the existence of the ultrahigh-Q resonances on the lattice modes in both polarizations, red-shifted from the Rayleigh Anomalies due to the guided waves of the substrate. If the periodicity vanishes, their frequencies tend to the purely real values so that Q-factors grow unlimitedly. These resonances do not exist on the PEC-strip and graphene-strip gratings placed in the free space.

- In the H-polarization case, we have quantified the resonances on the plasmon modes and found the effect of electromagnetically induced transparency (EIT) that appears thanks to the tunability of the plasmon modes with the aid of graphene's chemical potential. As shown, it is possible to realize the electrostatic-bias controlled EIT in the THz range on the metasurface of microsize period. This can be useful in the design of novel tuneable sensors, filters, modulators and absorbers that use periodically

patterned graphene.

- In the E-polarization case, we have studied the lattice-mode resonances numerically and have shown analytically how the corresponding complex poles migrate to the non-physical sheet of the Rayleigh-Anomaly Riemann surface if the substrate vanishes.

- In the analysis of threshold conditions, we have computed the emission frequencies and threshold values of the substrate gain for the lasing modes of the considered metasurface nanolaser, visualized their near fields, and discussed their characteristics. The lowest thresholds are found for the lattice modes of the odd symmetry in each polarization, while the best tunability is demonstrated by the H-polarized plasmon modes. These findings open the way to design large-area tunable low-threshold micro- and nano-lasers of the terahertz and infrared ranges.

Keywords: strip grating, dielectric, scattering, regularization, resonance, plasmon mode, lattice mode, threshold, nanolaser.

АНОТАЦІЯ

Євтушенко Ф.О. **Резонансне розсіяння та поглинання електромагнітних хвиль нескінченними решітками з графенових стрічок на діелектричних підкладках**. – Кваліфікаційна наукова праця на правах рукопису.

Дисертація на здобуття наукового ступеня доктора філософії за спеціальністю 104 – фізика та астрономія (10 – природничі науки). - Інститут радіофізики та електроніки ім. О. Я. Усикова НАН України, Харків, 2023.

У дисертації проведено комплексний теоретичний аналіз розсіяння, поглинання та випромінювання електромагнітних хвиль нескінченними решітками з графенових стрічок, що лежать на діелектричних підкладках. Практичне значення цього дослідження полягає в тому, що воно має застосування в електромагнітно-хвильових пристроях і системах, які працюють у терагерцевому, інфрачервоному та видимому діапазонах світла. У цьому контексті поява графену відкриває багато нових і захоплюючих можливостей. Це пов'язано з тим, що графен має високу рухливість електронів, що може перестроюватися за електростатичним чином (через хімічний потенціал графену), і проявляє плазмонні ефекти.

Метою роботи є, по-перше, вивчення резонансних ефектів у розсіянні та поглинанні H- та E-поляризованих електромагнітних хвиль нескінченною решіткою з графенових стрічок, що лежать на пасивній діелектричній підкладці. Можна очікувати, що така метаповерхня поводиться як композитний періодичний відкритий резонатор. Її висока частотна селективність випливає з існування трьох типів власних мод: низькодобротних мод підкладки і надвисокодобротних мод решітки, які існують в обох поляризаціях за умови наявності підкладки, а також помірковано-добротних плазмонних мод графенових стрічок, які існують тільки в H-поляризації. По-друге, ще однією важливою метою є вивчення порогових умов

для H- і E-поляризованих мод лазерного випромінювання нескінченної плоскої решітки з графенових стрічок, що лежать на підкладці з підсилюючого матеріалу. При цьому особливу увагу приділено перестроюванню плазмонних мод і надвисокодобротних мод решітки за допомогою хімічного потенціалу графену.

Для досягнення поставленої мети **розглядаються наступні задачі**:

- Виведення добре обумовлених матричних рівнянь для розсіяння та поглинання плоских хвиль нескінченною решіткою з графенових стрічок нульової товщини, розміщених на діелектричній підкладці, у випадках E- та H-поляризацій. Це ґрунтується на строгому формулюванні відповідних крайових задач розсіяння хвиль. Отримані матричні рівняння становлять основу чисельних алгоритмів.

- Написання й тестування повнохвильових безсіткових кодів у середовищі Матлаб та їхня перевірка шляхом порівняння з опублікованими раніше результатами інших збіжних чисельних методів за їхньої наявності.

- Дослідження поведінки обчислювальної похибки в залежності від порядку усікання матричних рівнянь для підтвердження збіжності алгоритмів і візуалізації впливу різних параметрів на швидкість збіжності.

- Систематичне використання розроблених комп'ютерних кодів для аналізу характеристик розсіяння та поглинання хвиль на розглянутих графенових стрічкових метаповерхнях, особливо з точки зору можливості їхнього налаштування за допомогою хімічного потенціалу графену.

- Виведення наближених формул для частот і добротностей плазмонних мод, решіткових мод та мод діелектричної підкладки.

- Адаптація отриманих добре обумовлених матричних рівнянь до випадку підкладки, що складається з матеріалу з посиленням. Поєднання цих рівнянь з ітераційним пошуком коренів детермінантних рівнянь. Систематичний строгий аналіз порогових умов для власних мод нескінченної графенової решітки на підкладці з матеріалу з посиленням у випадках H- і E-поляризацій.

На попередньому етапі дослідження розглянуто допоміжні задачі розсіяння плоских H- і E-поляризованих хвиль на нескінченній плоскій решітці з ідеально

провідних стрічок нульової товщини, розміщених на поверхні діелектричної підкладки. Дотримуючись підходу, вперше розробленого в 1960-х роках, ми зводимо цю задачу для кожної з двох поляризацій до рівняння в парних рядах для комплексних амплітуд просторових гармонік розсіяного поля Флоке. Потім ми виконуємо аналітичну регуляризацію цього рівняння, засновану на оберненні статичної частини задачі, пов'язаної з решіткою у вільному просторі, за допомогою методу задачі Рімана-Гілберта. У кожному випадку це дає нескінченне матричне рівняння Фредгольма другого роду, чисельний розв'язок якого має гарантовану збіжність. Ми приводимо ці рівняння до вигляду, зручного для обчислень, і порівнюємо результати з контрольними результатами. Далі ми проводимо чисельні експерименти, які демонструють, як швидкість збіжності нашого безсіткового коду залежить від товщини та діелектричної проникності підкладки. Характеристики розсіяння виявляють резонанси на модах підкладки та на решіткових модах сруктури в цілому як періодичного відкритого резонатора.

Згодом дослідження поширено на розсіяння H- і E-поляризованих плоских хвиль подібною решіткою, але з графеновими стрічками на поверхні діелектричної підкладки. Комплексна провідність графену моделюється за допомогою квантових формул Кубо. Через скінченну провідність граничні умови на стрічках перетворюються на резистивні умови. У випадку H-поляризації наш повнохвильовий безсітковий код базується на аналітичному напівоберненні, що використовує розв'язок задачі Рімана-Гілберта, – таким чином, він є модифікацією регуляризації для ідеально провідних стрічок. Однак, у випадку E-поляризації, модифіковане рівняння у парних рядах, до якого зводиться задача розсіяння, не дозволяє скористатися методом задачі Рімана-Гілберта для побудови збіжного алгоритму. Замість цього ми регуляризуємо це рівняння за допомогою зворотного дискретного перетворення Фур'є. Це призводить до матричного рівняння Фредгольма 2-го роду для амплітуд гармонік Флоке, що гарантує збіжність коду. Завдяки збіжності обчислювальну похибку можна контролювати й зменшити навіть до машинної точності. В обох поляризаціях елементи матриць включають

лише елементарні функції, і тому наші коди є не лише точними, але й дуже економічними. Використовуючи такий надійний інструмент, ми проводимо детальний чисельний аналіз розсіяння та поглинання хвиль і зосереджуємо увагу на взаємодії між резонансами на різних власних модах. Новим явищем, порівняно з решіткою з ідеально провідних стрічок, є існування H-поляризованих плазмонних мод графенових стрічок. Якщо частота плазмонної мод співпадає з частотою надвисокодобротної решіткової моди, то має місце режим електромагнітно індукованої прозорості метаповерхні, яка досліджується.

Насамкінець у дисертації досліджено порогові умови для H- і E-поляризованих мод лазерного випромінювання графенової стрічкової решітки на підкладці. На відміну від попереднього тут припускається, що матеріал підкладки має посилення, яке компенсує випромінювальні й омічні втрати і дозволяє модам досягти порогу самозбудження. Ми шукаємо частоту і порогове значення показника посилення, специфічне для кожної моди, як власні значення. Щоб їх знайти, ми зводимо задачу поля до парних рядів для комплексних амплітуд просторових гармонік Флоке, які ми аналітично регуляризуємо за допомогою методу задачі Рімана-Гілберта для H-мод і за допомогою зворотного дискретного перетворення Фур'є для E-мод. Окрім цього, ми розділяємо моди на парні і непарні класи симетрії відносно середини стрічки. В кожному з випадків це призводить до нескінченного детермінантного рівняння, що відповідає матричному рівнянню Фредгольма другого роду для власних значень. Збільшення числа усікання матриці гарантує збіжність цих величин до точних власних значень. Візуалізовано портрети полів усіх мод, що вивчаються.

В роботі отримано наступні **нові наукові результати**:

- У випадку розсіяння плоских хвиль вивчено швидкість збіжності відповідних чисельних алгоритмів та її залежність від різних параметрів підкладки й решітки, в тому числі від параметрів графена.

- Наші розрахунки показали існування високодобротних резонансів на решіткових модах обох поляризацій, що пов'язані з аномаліями Релея, але не

існують на решітках з ідеально провідних чи графенових стрічок, розміщених у вільному просторі. У випадку H-поляризації ми вивчили резонанси на плазмонних модах, яких немає у E-поляризації

- У випадку H-поляризації виявлено ефект електромагнітно індукованої прозорості, який виникає завдяки переналаштуванню плазмонних мод за допомогою хімічного потенціалу графену. Як показано, можна реалізувати цей ефект, керований електростатичним чином, у терагерцевому діапазоні на метаповерхні з мікророзмірним періодом. Це може бути корисним при розробці нових фільтрів, модуляторів і поглиначів, які використовують графен з періодичною структурою й можуть бути переналаштовані.

- В рамках аналізу порогових умов для випромінювання мод розглянутих метаповерхонь як нанолазерів ми розраховували частоти випромінювання і порогові значення показника посилення підкладки та відшукували їхні ближні поля для різних класів симетрії. Найнижчі пороги виявлено для решіткових мод кожної поляризації з непарною симетрією, тоді як найкращу переналаштованість демонструють H-поляризовані плазмонні моди. Ці результати відкривають шлях до створення низькопорогових мікро- й нанолазерів терагерцевого та інфрачервоного діапазонів, які можуть переналаштовуватися.

Ключові слова: стрічкова решітка, графен, розсіяння хвиль, аналітична регуляризація, резонанс, плазмонна мода, решіткова мода, поріг, нанолазер.

LIST OF PUBLICATIONS RELATED TO THESIS

Papers in international journals

1. F.O. Yevtushenko, S.V. Dukhopelnykov, Y.G. Rapoport, T.L. Zinenko, R. Sauleau, and A.I. Nosich, " Tunability of non-plasmon resonances in the E-polarized terahertz wave scattering from microsize graphene strip-on-substrate gratings," Optical Materials Express, vol. 13, no 8, pp. 2274-2287, 2023. (Scopus, Q2). https://doi.org/10.1364/OME.496037
2. F.O. Yevtushenko, S.V. Dukhopelnykov, Y.G. Rapoport, T.L. Zinenko, and A.I. Nosich, “Spoiling of tunability of on-substrate graphene strip grating due to lattice-mode-induced transparency,” Royal Society of Chemistry Advances, vol. 12, pp. 4589–4594, 2022. (Scopus, Q2). https://doi.org/10.1039/d1ra08287f
3. F.O. Yevtushenko, S.V. Dukhopelnykov, Y.G. Rapoport, and T.L. Zinenko, "Electromagnetic characterization of tuneable graphene-strips-on-substrate metasurface over entire THz range: Analytical regularization and natural-mode resonance interplay," IET Microwaves, Antennas and Propagation, vol. 15, no 10, pp. 1225-1239, 2021. (Scopus, Q2). https://doi.org/10.1049/mia2.12158
4. F.O. Yevtushenko, S.V. Dukhopelnykov, and T.L. Zinenko, "E-polarized plane-wave scattering from a PEC strip grating on a dielectric substrate: analytical regularization and lattice-mode resonances," Journal of Electromagnetic Waves and Applications, vol. 35, no 10, pp. 1388–1405, 2021. (Scopus, Q3). https://doi.org/10.1080/09205071.2021.1887001
5. F.O. Yevtushenko, S.V. Dukhopelnykov, and A.I. Nosich, " H-polarized plane-wave scattering by a PEC strip grating on top of a dielectric substrate: analytical regularization based on the Riemann-Hilbert Problem solution," Journal of Electromagnetic Waves and Applications, vol. 34, no 4, pp. 483-499, 2020. (Scopus, Q3). https://doi.org/10.1080/09205071.2020.1722258

Papers in proceedings of international conferences, indexed in Scopus

6. F.O. Yevtushenko, "Threshold analysis for the modes of microsize graphene strip grating laser," Proc. Int. Conference Applied Electromagnetics and Communications (ICECOM-2023), Dubrovnik, 2023.

7. F.O. Yevtushenko, S.V. Dukhopelnykov, "Emission frequencies and thresholds for microsize graphene strip grating on gain substrate," Proc. European Microwave Conference (EuMC-2023), Berlin, 2023, pp. 548-551.

8. F. O. Yevtushenko, "Resonance scattering and absorption of the E-polarized plane wave by graphene strip on-substrate grating" International Conference on Electronics and Nanotechnology (ELNANO-2022), Kyiv, 2022, pp. 196-201.

9. F. O. Yevtushenko, S. V. Dukhopelnykov, "Resonances in the E-polarized terahertz wave scattering and absorption by a graphene strip on-substrate grating" Proc. European Microwave Conference (EuMC-2022), Milan, 2022, pp. 736-739.

10. F. O. Yevtushenko, "Role of substrate in the H-polarized terahertz wave scattering and absorption by a graphene strip on-substrate grating," Proc. Int. Conf. EEE International Conference on Information and Telecommunication Technologies and Radio Electronics, Proceedings, (UkrMiCo 2021), Kyiv, 2021, pp. 279-282.

11. F. O. Yevtushenko, "H-polarized terahertz wave scattering from on-substrate graphene strip grating: electromagnetically induced transparency," Proc. Int. Conference Microwaves, Communications, Antennas, and Electronic Systems (COMCAS-2021), Tel Aviv, 2021, art. no 21483684

12. F. O. Yevtushenko, S. V. Dukhopelnykov, and T. L. Zinenko, "Basic equations of the lasing eigenvalue problem for a graphene strip on-substrate grating, H-polarization," Proc. IEEE Ukrainian Conference Electrical Computer Eng. (UKRCON-2021), Lviv, 2021.

13. F. O. Yevtushenko, "Convergence study for the method of analytical regularization applied to the E-plane-wave scattering from a PEC strip grating on a

dielectric substrate," Proc. Int. Conference Ukrainian Microwave Week (UKRMW-2020), Kharkiv, 2020, pp. 504-506.

14. F. O. Yevtushenko, S. V. Dukhopelnykov, and T. L. Zinenko, “Fano-shape lattice-mode resonances and near fields in the E-polarized wave scattering by a PEC strip grating on a dielectric substrate,” Proc. Int. Conference Ukrainian Microwave Week (UKRMW-2020), Kharkiv, 2020, pp. 516-519.

15. F. O. Yevtushenko and S. V. Dukhopelnykov, "Method of analytical regularization based on the static part inversion in the H-wave scattering by a PEC strip grating on top of a dielectric substrate," Proc. Int. Conference Microwaves, Communications, Antennas, and Electronic Systems (COMCAS-2019), Tel Aviv, 2019, art. no 8958263.

16 F. O. Yevtushenko, S.V. Dukhopelnykov, and A. I. Nosich, "Plane-wave scattering by a PEC strip grating on top of a dielectric substrate: basic equations, regularization, and convergence," Proc. IEEE Ukrainian Conference Electrical Computer Eng. (UKRCON-2019), Lviv, 2019, pp. 797–801.

CONTENTS

LIST OF NOTATIONS…….. 17

INTRODUCTION……. **18**

CHAPTER 1 LITERATURE REVIEW AND ANALYSIS……. **30**

1.1 Diffraction gratings in electromagnetic wave physics and engineering **30**

1.2 Problems of wave scattering from flat strip gratings……. **33**

1.3 Methods of diffraction theory used in the thesis…… **38**

1.4 Quantum Kubo model of graphene conductivity and impedance **43**

1.5 Plasmonic lasers and Lasing Eigenvalue Problem …….. **46**

Conclusions to Chapter 1……. **51**

CHAPTER 2 AUXILIARY PROBLEM: SCATTERING OF PLANE WAVES FROM PERFECTLY ELECTRICALLY CONDUCTING STRIP GRATING ON DIELECTRIC SUBSTRATE **52**

2.1 Scattering problem formulation…… **52**

2.2. Analytical regularization using the Riemann-Hilbert Problem method **55**

2.2.1 H-polarization, basic equations ……. **57**

2.2.2. E-polarization, basic equations ……. **59**

2.3. Validation and results of numerical study of wave scattering ……. **62**

2.3.1. H-polarization: resonances on substrate and lattice modes….. **62**

2.3.2. E-polarization: resonances on substrate and lattice modes… **71**

Conclusions to Chapter 2……. **81**

CHAPTER 3 SCATTERING AND ABSORPTION OF PLANE WAVES BY GRAPHENE STRIP GRATING ON DIELECTRIC SUBSTRATE ... **83**

3.1 Scattering problem formulation ……..……... **84**

3.2 H-case: regularization by the Riemann-Hilbert problem method ….. **85**

3.3. E-case: regularization using the inverse Fourier transform……... **89**

3.4. Analytical study of the Rayleigh Anomalies and natural modes ….. **90**

3.5. Results of numerical study of wave scattering and absorption **95**

3.5.1. H-case: resonances on substrate, plasmon and lattice modes **95**

3.5.2. E-case: resonances on substrate and lattice modes……. **105**

3.6. Regime of electromagnetically induced transparency……..... **114**

Conclusions to Chapter 3……. **120**

CHAPTER 4 LASING THRESHOLD CONDITIONS FOR GRAPHENE STRIP GRATING ON GAIN-MATERIAL SUBSTRATE ……. **122**

4.1 Modified eigenvalue problem formulation ..……. **123**

4.2. Reducing eigenvalue problems to determinantal equations…… **125**

4.2.1. H-polarization case…… **125**

4.2.2. E-polarization case …….. **127**

4.3. Results of numerical study of mode threshold conditions …… **128**

4.2.1. H-polarized laser modes …… **128**

4.2.2. E-polarized laser modes …… **138**

Conclusions to Chapter 4……. **146**

CONCLUSIONS……... **148**

REFERENCES……. **149**

APPENDIX A LIST OF PUBLICATIONS RELATED TO THESIS ….. **161**

LIST OF NOTATIONS

CVD = Chemical Vapor Deposition

DG = Diffraction Gratings

DSE = Dual Series Equation

EIT = Electromagnetically Induced Transparency

IDFT = Inverse Discrete Fourier Transform

IE = Integral Equation

LEP = Lasing Eigenvalue Problem

LM = Lattice Mode

MAR = Method of Analytical Regularization

OT = Optical Theorem

PEC = Perfect Electrically Conducting

PM = Plasmon Mode

RA = Rayleigh Anomaly

RIIT = Residual Inverse Iteration Technique

RHP = Riemann-Hilbert Problem

SIE = Singular IE

SM = Slab Mode

THz = Terahertz

2-D = Two-Dimensional

INTRODUCTION

Justification of the choice of research topic. In computational electromagnetics, important place is occupied by the study of electromagnetic wave scattering from two-dimensional, i.e., single-periodic, diffraction gratings. Among the most important shapes of gratings, besides of the periodically grooved metallic and dielectric interfaces, e.g. echelette, and periodic wire grids, one can frequently see arrays of long and thin strips located on the surface of flat dielectric substrates. This is because of several reasons. First, various sophisticated technologies enable fabrication of such strip configurations - printing, wet and dry deposition, sputtering, molecular-bean epitaxy, and others. Secondly, this is cheaper and better controlled than cutting the grooves or winding the wires on a frame. The spacing, or periodicity, is necessarily comparable or smaller than the wavelength – this means that today, when nanotechnologies routinely work with nanoscale objects, it is possible to fabricate on-substrate gratings of nanometer-wide gold or silver or graphene strips or other flat shapes. This opens many exciting opportunities for the development of novel and efficient wave-forming devices, components and sub-systems of the terahertz (THz), infrared and visible light ranges.

Still, nanotechnologies are very expensive – so expensive that in Ukraine, there is no any laboratory or industry, which can fabricate nanoscale photonic circuits or even much simpler objects such as patterned graphene. This circumstance calls for reliable pre-fabrication modeling of the micro and nano-scale configurations in general and various strip gratings in particular. As it is obvious, to be reliable and predictive, such modeling must be based on the full-wave (i.e. rigorous) formulations of the wave-scattering problems and lead to the convergent numerical algorithms.

By today, the best developed chapter of the theory of wave scattering from strip gratings concerns the infinite gratings of PEC strips. This is because since the 1950s to the 1990s the main application area was the microwave circuits, where the metals can be safely considered as perfect conductors. Apart of many approximate techniques, the

main achievements here are associated with the development of two methods: the analytical regularization or semi-inversion based on the Riemann-Hilbert Problem (RHP) solution and the numerical quadratures or Nystrom method. This is because the algorithms developed on the basis of these methods have mathematically guaranteed (i.e. proven by theorems) convergence and thank to this controlled accuracy.

Still, a general trend in electromagnetic wave technology is the development of more and more high-frequency ranges, in particular, terahertz and infrared. However, in these ranges, the PEC model is not suitable even for scatterers made of noble metals such as silver or gold. Besides, new "2-D" materials of single-atom thickness have emerged, such as graphene, which is also imperfect conductor [1,2]. Moreover, it is known that the surface impedance of graphene is a complex quantity with a negative imaginary part. This leads to the resonant effects in the scattering and absorption of waves by graphene objects due to the excitation of surface plasmon resonances, which have a wide range of practical applications [3-9]. As all resonances, they appear thanks to the plasmon modes (PM), which have very small radiation losses but moderate ohmic losses. When the H-polarized waves are scattered by the graphene strip gratings, PM resonances are excited. Thus, for example, in the development of biosensors, plasmonic effects can significantly enhance the ability to detect and identify biological substances by increasing the intensity of fluorescence. Moreover, thanks to modern technologies, micro- and nanoscale graphene strips, disks and other flat shapes (i.e. the patterned graphene) are incorporated into many novel THz and infrared devices.

Note that the plasmon resonances on the noble-metal particles and strips, in the visible-light range, have long history of analysis and applications in bio and chemo-sensors [10-12]. Still, their use has been always corrupted by the considerable ohnic losses, which spoil the Q-factors. In contrast to metals, graphene displays plasmon effects at two orders lower frequencies and has at least by order lower losses.

Due to the ultra-small thickness, even if lying on dielectric substrates, periodic arrays of such flat shapes are customarily called *metasurfaces*. The gratings made of hundreds or thousands of graphene micro- and nano-strips are attracting special

attention in the development of refractive index sensors and absorbers [13-24]. This is closely related to the recently discovered phenomena of anomalous reflection, transmission, and emission of light, as well as near-field enhancement, giant Kerr and Faraday effects and some others. In the most general case, such phenomena have the form of asymmetric Fano-type resonances and are observed near the so-called Rayleigh Anomalies (RA) of the corresponding infinite gratings. Within the past 10 years, all of them have been linked to the so-called lattice-mode (LM) resonances [24]. In the literature, one can find contradictory statements on the nature of LMs – they are frequently mixed up with RAs and, if traced on arrays of noble-metal particles, with exotic forms of PMs. These resonances have by orders higher Q-factors that the PM resonances that makes them very attractive for the sensing applications, however, entails great difficulties in their accurate modeling. Indeed, to study the ultrahigh-Q resonances, one needs very fine numerical algorithms, able to deliver many correct digits in the obtained results. This makes usual commercial codes, such as COMSOL, HFSS, Microwave Studio, or FEKO, essentially pointless – they are not based on the convergent algorithms and provide results with low accuracy of a few first digits.

Thus, the task of studying the resonance effects in the scattering and absorption of the H- and E-polarized plane waves by infinite on-substrate graphene strip gratings, using the algorithms with guaranteed convergence and controlled accuracy is timely and relevant. Still, to study them accurately, one cannot simply use the MAR techniques developed earlier for the PEC strip gratings because imperfect conductivity changes the boundary conditions on the strips to the so-called two-side resistive conditions.

As discussed in [20], in the H-polarization case such a change is only a smooth perturbation of the PEC condition – therefore, the MAR-RHP technique can be adapted to treat this case. In contrast, in the E-polarization case this change is a singular perturbation to the PEC condition and the RHP technique becomes inapplicable. However, there is a good side – the non-zero impedance of graphene plays the role of the regularizing parameter. Thanks to this circumstance, the analytical regularization is achieved by the application of the Inverse Discrete Fourier Transform. These techniques

are known since [25], however, only for the imperfect strip gratings suspended in the free space. Therefore, it is necessary to modify these techniques and adapt them to the on-substrate grating case. This is performed in the thesis. Having such a trusted and efficient computational instrument, we can conduct systematic numerical investigation of the scattering and absorption, focusing our study on the resonances on PMs, their electrostatic tunability, and revealing the characteristics of ultrahigh-Q resonances on LMs both in the H and E-polarization cases.

Additionally, casting a wave scattering problem to a Fredholm second kind matrix equation opens the way for the accurate analysis of the so-called “natural modes” of the considered scatterer as an open resonator. The complex-valued natural mode frequencies are then the roots of the determinantal equation. The Fredholm theorems tell that such frequencies are discrete in the whole complex domain. They depend continuously on the other parameters and can appear or disappear only at the branching points and at infinity.

This circumstance gives an interesting idea to investigate the natural modes of the graphene-strip grating lying on dielectric substrate, from new point of view – namely, to consider them as the laser modes at the threshold of stationary emission. Here, the lasing is understood as existence of real-frequency modes of the open resonator – because the residue in such a pole is a non-attenuating in time outgoing electromagnetic wave. This implies assuming the presence of the active region, i.e. a domain filled in with the gain material.

As can be seen from the literature, within the past several years, one of the most promising trends in the development of micro and nanoscale lasers is associated with arrays of noble-metal particles or strips [26]. Although this is not always well understood and acknowledged, the working modes in such lasers are the LMs. However, they have rather high thresholds that is understandable because of the lossy nature of metals. Here, taking into account that the graphene has lower losses than the metals, it is reasonable to suggest a replacement of noble-metal elements of arrays with the graphene ones. Guided by these considerations, we undertook the investigation of

the threshold conditions (i.e. the emission frequencies and associated threshold values of the gain-material index) for the natural modes of the graphene-strip grating lying on the gain-material substrate.

The object of research is the electromagnetic field scattered and absorbed by the infinite graphene strip grating on dielectric substrate and emitted by such a grating on non-magnetic gain-material substrate.

The subject of the study is the resonance effects in the scattering and absorption by the graphene strip grating on dielectric substrate that appear due to the natural modes of such a periodic open resonator, and the threshold conditions for these natural modes in the case of the gain-material substrate.

The goals of the work are two-fold:

- to study, using the convergent algorithms, the resonance effects, which arise due to the natural modes, in the H- and E-polarized electromagnetic wave scattering and absorption by graphene strip grating on passive dielectric substrate,

- to study, using the convergent algorithms, the threshold conditions for the H- and E-polarized natural modes of graphene strip grating on the gain-material substrate.

To achieve these goals, the following **tasks are considered:**

– Derivation of the Fredholm second kind matrix equations for the scattering and absorption of plane wave by graphene strips grating on substrate in the case of the H- and E-polarization,

– Writing and testing codes and validating them by comparison with results of the other convergent numerical methods, when available,

– Study of the error behavior depending on the matrix truncation order to confirm convergence,

– Use of developed codes for the analysis of the scattering and absorption characteristics of the considered graphene-strip metasurfaces, especially their tunability with graphene’s chemical potential,

– Derivation of approximate formulas for the frequencies and Q-factors of the plasmon, lattice and dielectric substrate modes,

– Adapting the derived equations and codes to the case of substrate, maid of the gain material. Combining these equations with iterative search of the roots of determinantal equations,

– Systematic full-wave analysis of threshold conditions for the modes of graphene strip grating on gain-material substrate in the cases of the H- and E-polarizations.

On the choice of parameters. In the numerical analysis, we had decided to focus on metasurfaces featuring strips made of graphene with the strip width, grating spacing, i.e. period, and substrate thickness all measured in micrometers. This is because in such case all the resonances are found in the THz range, which is actively developed today. These metasurfaces can be viewed as composite periodic open resonators. They are expected to exhibit strong frequency selectivity due to the interplay of three distinct natural mode types: low-Q slab modes (SM), moderate-Q plasmon strip modes (PM), and ultrahigh-Q lattice modes (LM), which do not exist in the absence of the substrate.

In view of the current trends in micro and nano optics and photonics and gaining on the accurate analysis of the wave scattering and absorption, we had decided additionally to turn to the equally accurate analysis of the lasing threshold conditions for the plasmon and non-plasmon modes of graphene strip grating on the gain-material substrate, in the H and E-polarizations. As the gain materials are rare in the THz range and better known in the infrared, here we take the strip dimensions, in part of analysis, in nanometers – this shifts the plasmon-mode resonances to the far-infrared range.

In the numerical analysis, our objective is to identify the most interesting and/or optimal configurations for the graphene-strip metasurfaces. It involves a systematic numerical analysis of various promising cases, exploring how parameters like period, substrate thickness, and especially the chemical potential impacts the metasurfaces' electromagnetic characteristics. The latter parameter, being not restricted in theory, is known to vary from zero to 1 eV with today’s best graphene samples. These samples show the electron relaxation time up to 0.5 ps. Hence, we use these values in our computations. Besides, we routinely assume that the room-temperature conditions are maintained, with 300 K temperature.

These mentioned above tasks are solved in **4 chapters of the work**.

The first chapter discusses briefly the phenomenon and concept of diffraction gratings in electromagnetic wave physics and engineering, as well as some of their applications and the associated modelling problems. Then, one can consider the basic problems of wave diffraction on flat gratings of PEC and graphene strip on a dielectric substrate, namely the wave scattering and eigenvalue problem. Here, essential details are given for the methods of the scattering theory used in this thesis in the analysis of imperfect strip gratings. The last thing considered in this chapter, but no least important, is the Kubo description of the graphene conductivity and surface impedance.

The second chapter is devoted to the auxiliary problems of the plane-wave scattering from an infinite grating of the PEC strips on dielectric substrate. This implies mathematical formulation of BVP, basic equations, convergence, validation, and numerical experiments focused on the LM resonances in such a configuration.

The third section deals with the scattering and absorption of the H- and E-polarized plane waves by infinite flat grating of graphene strips lying on dielectric substrate. This implies mathematical formulation of BVP, basic equations, convergence, validation, and numerical experiments focused on the tunability of the PM resonances with the chemical potential and on the LM resonances. Besides, we study the effect called electromagnetically induced transparency where both a plasmon mode and a lattice mode are involved.

The forth chapter presents the analysis of the H and E-polarized lasing modes of the infinite flat grating of graphene strips on the active substrate. The substrate material is assumed to have gain that offsets the radiation and ohmic losses and allows the modes to reach the lasing threshold. We look for the frequency and the gain index threshold value, specific to each mode, as eigenvalues.

The obtained results are summarized in Conclusions and Recommendations.

Research methods. The research methods include the time-harmonic wave scattering theory, i.e. the 2-D boundary value problems (BVP) of classical electromagnetics, and the theory of associated eigenvalue problems. These BVPs

consist of the following conditions: (I) the Helmholtz equation, (II) the graphene boundary condition on the strips and the tangential-components continuity conditions across the material boundaries, (III) the radiation condition, (IV) the local power finiteness condition (the same as edge condition). In the wave-scattering problems, conditions (I)-(IV) ensure the uniqueness of the solution at any real-valued frequency. They are inherited in the eigenvalue problems, if these problems are modified to access the lasing, which is understood as existence of the real-valued natural frequencies. As known, this is possible only in the presence of the active regions, i.e. domains filled in with the gain materials. Such materials are modeled as “active dielectrics” via the use of the negative imaginary part of the complex-valued permittivity or refractive index. Further, the conductivity of the graphene is characterized with the aid of the known Kubo formalism based on the quantum theory. Due to this fact, the whole treatment becomes *semi-classical*, i.e. a classical electromagnetic BVP combined with quantum description of one of involved materials.

To build a robust and meshless full-wave algorithm, we use the Floquet expansions, transform each scattering problem into a double series equation, and apply a MAR approach. In the H-polarization case, our treatment is based on the RHP technique, adapted to the resistive boundary conditions on the strips. In the E-polarization case, we use the Inverse Discrete Fourier Transform. In each case, the resulting infinite matrix equations are of the Fredholm second kind type. Thanks to this, Fredholm theory guarantees the convergence of their numerical solutions, if the matrix size is taken larger. This allows us to calculate wave scattering and absorption characteristics with controlled accuracy.

In the eigenvalue problems, they are reduced to the determinantal equations generated by the same matrix operators as in the scattering problems. Here, the Fredholm theory guarantees the convergence of the approximate root to the exact ones, if the matrix size is taken larger.

Scientific novelty of obtained results. Modification of the RHP technique to the resistive boundary conditions on the strips in the H-polarization case, and the IDFT

technique, used in the E-polarization case, have been known since 1998 when the paper [25] was published. Later, these techniques were applied to the scattering from the graphene strip grating in the free space [20]. However, they have not been applied to the analysis of the graphene strip gratings lying on top of dielectric substrate. As on-substrate strip configurations are the most frequent in real life, this lack of accurate analysis and trusted results appeared too significant to be ignored.

Therefore, in terms of the novelty the center of gravity in this dissertation is in the accurate analysis of the physics of the wave scattering and natural-mode phenomena.

The following new results have been personally obtained by the author:

- The rate of convergence of the resulting meshless numerical algorithms have been demonstrated and validation of the computed results has been performed by the comparison with data obtained using another convergent technique, MAR-Galerkin. As we have shown, thicker and higher dielectric permittivity substrates request solving larger matrices for the same accuracy. This is the consequence of the fact that the inverted part is the static limit of the grating-on-interface problem.
- Using this accurate and efficient modelling tool, we have analyzed the interplay, in the range from zero to 10 THz, of the scattering and absorption resonances, caused by the H-polarized natural modes of three types and different Q-factors: SMs of the substrate, PMs of the graphene strips, and LMs. Remarkably, the LM Q-factors (if the grating is infinite), grow up infinitely if the substrate gets thinner or its contrast with host medium vanishes.
- We have demonstrated that thanks to the tunability of the H-polarized plasmon modes with the aid of graphene's chemical potential, it is possible to realize an EIT. This can be useful in the design of novel tunable filters, modulators and absorbers that use periodically patterned graphene.
- Our computations have confirmed the presence of the high-Q resonances on LMs, in the either polarization, that do not exist on the strip grating placed in the free space. In the E-polarization case, we have derived analytical expressions for the complex

frequencies of LMs. These expressions, for the first time, demonstrate how the LM poles hide to the non-physical sheet of the RA Riemann surface and migrate to the physical sheet thanks to finite-thickness substrate.

- We have accurately studied the threshold conditions for the modes of the graphene strip grating on the gain-material substrate. As we have found, the modes split into two classes according to the symmetry or anti-symmetry relatively to the strip middle line. The lowest thresholds are found for the LMs in each symmetry class, while the best tunability in frequency, within a factor of 2 to 3, is demonstrated by the PMs.

Practical value of obtained results.

The practical significance of the developed algorithms is seen in their ability to provide trusted modeling of the performance of corresponding sensors, absorbers and filters based on the graphene strip gratings in the THz and infrared frequency ranges.

The analysis of the PMs electrostatic tunability and their hybridization with LMs, accompanied with the effect of electromagnetically induced transparency, helps establish safe frequency limits in the design of frequency-tunable devices.

As shown, the LM resonance effects are so fine that their accurate characterization calls for adequately refined numerical approaches. Indeed, even if the substrate is moderately thin, say, has the thickness of 1 μm, the LM Q-factors can reach 10^6, so that the numerical solutions must deliver 6 or more correct digits. Such high accuracy is not accessible with existing today commercial codes. In contrast, the MAR-based codes can easily provide this accuracy, controlled by the matrix truncation order.

The results related to the threshold conditions for the modes of the graphene-strip gratings on gain-material substrates can be used in the pre-design and evaluation of low-threshold tunable nanolasers in the THz and infrared frequency ranges.

Thanks to the combination of high speed and accuracy, the developed codes can be used as the engines in the numerical multi-parametric optimization routines that are based on the local (e.g. gradient-type) and global minimization of target functions.

Personal contribution of the author. The main results presented in this thesis

have been obtained by the author himself. In the case of papers with co-authors [1A-16A], the author's contribution consists in deriving the basic equations, developing the numerical algorithms, writing and testing the codes in Matlab environment, as well as in the systematic calculation of the results obtained, preparation of the publication drafts, and presentation of results at international conferences.

Dissemination of results. The results of the work were presented and discussed at the scientific seminar of IRE NASU (Prof. P. M. Melezhyk).

Besides, they were presented at the following international conferences:

– IEEE Ukrainian Conferences on Electrical and Computer Engineering (UKRCON), Lviv, 2019, 2021;

– IEEE International Conference on Microwaves, Communications, Antennas, and Electronic Systems (COMCAS), Tel Aviv, 2019, 2021;

– IEEE International Conference Ukrainian Microwave Week (UKRMW), Kharkiv, 2020, 2 presentations;

– IEEE International Conference on Information and Telecommunication Technologies and Radio Electronics, Proceedings, (UkrMiCo) Kyiv, 2021;

– European Microwave Conferences (EuMC), Milan, 2022, Berlin, 2023;

– IEEE International Conference on Electronics and Nanotechnology (ELNANO), Kyiv, 2022;

– International Conference on Applied Electromagnetics and Communications (ICECOM), Dubrovnik, 2023.

Publications. The results of research have been published in 16 refereed papers indexed in Scopus, including 5 papers in international journals [A1-A5] and 11 papers in the proceedings of international conferences [A6-A16].

Relation to scientific programs, projects and grants. The research within this thesis has been performed at the Laboratory of Micro and Nano Optics of the Quasioptics Department of IRE NASU, in the framework of the following projects:

1. Research project of NASU "Development and application of methods of optics and quasioptics for generation and transforming the electromagnetic waves of

terahertz, infrared and visible ranges", code "Oreol-1". #0117U004036, (2019-2022)

2. Research project of NASU "The research of interaction processes of electromagnetic radiation in terahertz, infrared and visible ranges with various natural or artificial materials, mediums and structures", code "Oreol-2", #0122U001710 (2022-2026)

3. Competitive research project of NASU, "Radiophysical phenomena in nanoelectronic systems based on graphene, unconventional superconductors and magnetized semiconductors", code "Nanograph", #0122U200724 (2022)

4. Research project of the National Research Foundation of Ukraine (NRFU) "Electromagnetic modeling of micro and nano lasers with resonant graphene elements, at the threshold of stationary emission", code "Sonata", #2020-02-0150 (2020-2022)

5. Joint research project with Universite de Rennes 1, “Dnipro” Programme of the Ministry of Education and Science, Ukraine and the Ministry of European and Foreign Affairs, France, code "Vilen" #0119U102172 (2019), #0120U104419, (2020)

6. Tender research project with Taras Shevchenko National University of Kyiv, code "Universum", #0120U104925 (2020), #0121U113145 (2021)

It has been also partially supported by the IEEE Antennas and Propagation Society Doctoral Research award for the project «Resonant scattering and absorption of terahertz waves by infinite gratings of graphene strips on dielectric substrate: analytical regularization based analysis» (2021).

Structure and size of thesis. The dissertation consists of an abstract, an introduction, 4 chapters, general conclusions, 1 appendix, a list of used sources with 120 titles. The volume of the total text of the dissertation is 163 pages, of which the main text is 147 pages. The work is illustrated with 62 figures and 3 tables.

CHAPTER 1
LITERATURE REVIEW AND RESEARCH METHODS

1.1 Diffraction gratings in electromagnetic wave physics and engineering

Diffraction gratings (DG), fundamental in optics and spectroscopy, play significant role in the analysis and shaping of electromagnetic waves. These optical devices were first proposed by D. Rittenhouse in [27]. They consist of a surface etched with an array of closely spaced, parallel grooves or slits. The distance between these slits, known as the "grating spacing" or period, is typically on the order of the wavelength of the incident light. When electromagnetic waves, such as visible light, encounter DG, they are scattered from the grating's periodic structure.

As light passes through the slits of DG, it undergoes a phenomenon known as diffraction. This process occurs because DG acts as an obstacle to the incident waves and the periodic structure causes the waves to interfere with each other. The interference results in the light being deflected or spread out into its constituent colors or wavelengths, creating what is known as a spectrum. This dispersion is a consequence of the wave nature of light and is described by Huygens' principle, which explains how each point on the DG surface can be thought of as a source of secondary waves.

The angular dispersion of the light is a key characteristic of a DG and depends on the wavelength of the incident light and the grating periodicity. This dispersion is governed by the grating equation, which was developed by A.-J. Fresnel in the early 19th century. The grating equation relates the angle, at which the different wavelengths of light are diffracted, to the DG parameters, specifically the period and the order of diffraction. Higher diffraction orders correspond to different angular directions for the dispersed light.

The concept of DGs dates back to the early 19th century, however, it is widely considered that it was J. von Fraunhofer who made groundbreaking contributions to their development. He invented the spectroscope, a device that employed DGs, revolutionizing the field of spectroscopy. His innovations allowed for the precise

measurement and analysis of spectral lines in the light emitted or absorbed by various materials. This marked the inception of DG applications in scientific research, where they became indispensable tools for understanding the composition, temperature, and properties of materials by splitting the light spectrum into its distinct components.

DGs have numerous applications in the fields of physics and engineering related to electromagnetic waves. Here are some specific applications:

Spectral filters: DGs are used to create spectral filters or monochromators that can isolate specific wavelengths or frequency ranges. These filters have applications in remote sensing, optical and microwave communication, and laser-based technologies where precise wavelength control is crucial.

Polarizers. Many types of DGs demonstrate remarkable polarization selectivity, i.e. transmit or reflect the waves of only one of two orthogonal polarizations or electric-field vector directions. In particular, this is true for a DG of metal wires or strips with the period smaller than the length of microwaves, as demonstrated by H. Hertz.

Spectral analysis: In physics and engineering, DGs are employed for detailed spectral analysis of electromagnetic waves. They help in identifying and quantifying the spectral lines, which are characteristic of different chemical elements and materials. This information is vital in various research and industrial applications. Spectrometers with DGs are critical tools in chemistry, astronomy, and materials science.

Interferometry: In fields like optics, THz quasi-optics, and radio astronomy, interferometers use DGs to measure the interference patterns produced by electromagnetic waves. This technique allows for high-precision measurements and is essential for diverse applications such as plasma diagnostics in Tokamak fusion machines and radio telescope calibration.

Holography: In the field of holography, DGs play a key role. They are used to create holograms by splitting laser light into various beams, which interfere to form a three-dimensional image. Holography is utilized in art, security, and data storage.

Optical communication: DGs are integral to the wavelength-division multiplexing in optical communication systems. Wavelength-division multiplexing

allows multiple data channels with different wavelengths to be transmitted simultaneously over optical fibers, greatly increasing data capacity and speed.

Vacuum electronics: several important types of microwave sources, such as traveling-wave tubes and orotrons, use DGs as components that slow down the electromagnetic wave phase velocity that is needed to provide efficient interaction with non-relativistic electron beams.

Antennas and radar: In microwave and millimeter-wave engineering, DGs can be used in phased-array antenna design to control the radiation pattern and hence improve the directionality of electromagnetic wave transmission and reception. They are also used in radar systems to analyze and manipulate radar signals.

Lasers: distributed-feedback laser systems incorporate DGs as the elements that provide light emission from the configurations without classical or Bragg-type mirrors.

These are just a few examples of how DGs are essential tools in physics and engineering for working with electromagnetic waves. Researchers and engineers continue to explore innovative ways to use DGs to advance our understanding of electromagnetic wave behavior and develop new technologies.

Here are some examples of problems related to different types of DGs in the physics of electromagnetic waves:

Diffraction efficiency optimization: Given a specific wavelength of incident wave, what are the parameters (such as period, material, and incidence angle) that maximize the diffraction efficiency of a DG, i.e. the intensity of a given diffraction order? This is essential for designing high-performance spectroscopy instruments.

Blazing angle calculation: For a specific DG, how can you calculate the blazing angle, which is the angle at which maximum diffraction efficiency occurs? Solving this problem is crucial in the design of monochromators and spectrometers.

Grating dispersion: Given the properties of a DG, how can you calculate the angular dispersion, which describes how different wavelengths spread apart when diffracted? This is important in designing systems for separating spectral lines in spectroscopy and for providing narrow-bad operation of radar and comunications.

Design of grating-based optical filters: How can you design a DG-based optical filter to selectively transmit or reflect specific wavelengths while blocking others? This problem is relevant in creating filters for various applications, including imaging and laser protection.

Diffraction grating polarization effects: How do DGs affect the polarization state of diffracted light? Understanding and mitigating polarization effects are crucial in applications where maintaining or manipulating polarization is essential.

Ultra-high resolution spectroscopy: What are the limitations and challenges in designing DGs for achieving ultra-high spectral resolution in spectroscopy? Solving this problem is pertinent in advanced scientific research where fine spectral features need to be resolved.

"Anomalous phenomena" linked to the lattice-mode resonances: How one can accurately determine the frequencies and Q-factors of such resonances of various DGs? They can be used in the design of sensors and filters with improved performance.

These problems encompass a range of challenges in the physics of electromagnetic waves when dealing with DGs. Researchers and engineers work on solving these problems to improve the performance of various optical systems and advance our understanding of electromagnetic wave behavior.

Some of the above tasks will be partially considered in this dissertation. In particular, the resonance phenomena and polarization selectivity of graphene-strip gratings are discussed, which is relevant to their application in sensors, filters, antennas, and lasers.

1.2 Problems of wave scattering from flat strip gratings

It should be noted that it was R. Wood in the beginning of the 20^{th} century who noticed that the light is "anomalously" (i.e. with much larger or smaller intensity) diffracted by DGs at certain wavelengths [28]. These wavelengths gave rise to the term "Wood Anomalies." Soon after that, Lord Rayleigh built the foundations of the wave

theory of DGs based on the Floquet expansions [29]. He found that some of the Wood Anomalies could be explained via the “passing over horizon” of the diffraction orders – such wavelengths obtained the name “Rayleigh-Wood Anomalies” or simply “Rayleigh Anomalies” (RA). They are caused solely by the periodicity and depend on the grating period-to-wavelength ratio and the incidence angle. Still, other Wood Anomalies did not follow Rayleigh’s rule and were linked to the fine structure of the grating period, also called “elementary cell” [30].

Important step ahead in the understanding of the electrometric characteristics of DGs was made by A. Hessel and A. Oliner who considered the plane-wave reflection from a periodically modulated impedance plane [31]. In this work they discovered sharp resonances near the RA frequencies. However, they did not understand that these resonances were caused by the complex poles of the field function; they simply did not notice these poles, which correspond to the LMs.

It should be noted that the theory of wave scattering from various DGs have been developed in the 1960s-1990s by many researchers [32-35]. Among them, a remarkable place is occupied by the books by the Kharkiv scientists [32-34]. Zero-thickness strip gratings are only one of many known DGs - they are briefly reviewed below.

The scattering of plane waves from the infinite flat grating made of PEC strips is a canonical problem of computational electromagnetics since the pioneering paper of H. Lamb over a hundred years ago [36]. Within this time, two mathematically grounded approaches that lead to the algorithms possessing the convergence have been developed. The first of them is based on the method of analytical regularization (MAR) and uses explicit inversion of the most singular part of the problem (this is its static part). The inversion can be performed in several equivalent ways.

According to one of them, MAR-Galerkin, the problem is reduced to a singular electric-field SIE for the strip current and then discretized using a Galerkin projection on the weighted Chebyshev polynomials, which form the set of orthogonal eigenfunctions of the IE static part [37,38]. The other way is to reduce the problem to the DSE for the amplitudes of the Floquet harmonics. In the early 1960s, it was found

that the DSE static part is equivalent to the RHP method [39], which can be solved analytically. In each case, the resulting infinite-matrix equation is a Fredholm second kind equation. This guarantees the convergence in the sense that the larger the matrix truncation order, the closer the solution to exact one, in a certain norm.

As a numerical alternative to MAR, the second approach has been developed since the 1970s. It is starting from the log-singular or hyper-singular IE as well, however, the numerical solution, with guaranteed accuracy, is obtained via a Nystrom-type interpolation. Here, unknown current function is approximated with a polynomial, the coefficients of which are found using the numerical quadratures [40,41]. Then, the resulting matrix equations possesses so-called strict diagonal dominance, which guarantees the convergence.

The MAR solutions for the PEC-strip gratings in the free space were further adapted to treat the imperfect gratings, made of resistive, impedance, and dielectric or metal strips [25,42-45]. This needed the use of the impedance boundary condition or the generalized boundary condition. As a result, the MAR techniques had to be modified and supplemented with IDFT for new type of DSE or its SIE analog. Later, the resistive strip grating solution was adapted to the graphene-strip grating in the free space [20].

Still, in the practical situations strip gratings are most frequently placed on a dielectric layer as a substrate. In the presence of a substrate, the corresponding modification of the mentioned above approaches and methods needs some analytical work however is always possible. This is because the singularities (related always to the static parts) remain the same. On the one hand, the MAR-RHP technique was extended to on-substrate PEC strip grating by Tretyakov [46], however, this work did not have any numerical results and, generally, is not directly suitable for programing. A numerical example can be found in the book [33], however, without the equations.

On the other hand, the MAR-Galerkin was applied to the on-substrate PEC-strip gratings by A. Matsushima [47,48] (in Fourier-transform domain) and J. Volakis [42] Cho [49] and Medina [50,51] and R. Hwang [52]. In [53,54], considered with AR-RGP were PEC-strip grating on more complicated material substrates. In these works,

extremely high-Q resonances were reported near to RAs, however, they remained unexplored.

As a consequence, when studying the auxiliary for us case of the plane-wave scattering from an infinite grating of PEC strips, located on the interface of a dielectric substrate, we had to write the basic equations of MAR-RHP technique "from scratch." Still, this was a necessary stage as it allowed us to validate the codes by a comparison with the reference results, obtained by MAR-Galerkin technique for PEC strips [51].

Unfortunately, there are no reference data for the graphene-strip grating case. Still, such data, obtained with MAR-Galerkin technique, is available for the permanent-resistivity strip grating on substrate [42]. Note that the data obtained with COMSOL [55] cannot be used as a reference because the authors admit that they had troubles with the convergence.

As mentioned, the main goals of the thesis are related to the wave scattering and emission by the graphene-strip DG on dielectric substrate.

Recent progress in nanotechnologies has attracted wide attention to graphene as a novel material, able to provide new functionalities to devices and systems, which use electromagnetic waves, especially in the terahertz, infrared, and visible-light ranges. This is explained by the fact that graphene is not only well conductive but has the conductivity tunable with the aid of DC electric biasing [1-4]. Besides, it can support surface plasmon guided wave with electric field, orthogonal to its surface, in the terahertz and infrared ranges, i.e. at two orders lower frequencies than the noble metals [16,17]. These properties make graphene very promising in the design of novel tuneable antennas, filters, sensors, and absorbers, to mention only a few possible devices.

Today, the focus of research into the applications of graphene in electronics and photonics shifts from wide-area sheets to the patterned configurations in the form of strips, disks and other flat forms [4,6]. Here, one of the most frequently considered configurations is a grating of parallel graphene strips [3,6-8]. In principle, such strips can be fabricated without substrate (suspended in air) that even improves their chemical stability [56]. However, typically patterned graphene configurations are located on the

surface of flat dielectric substrates. For instance, chemical vapor deposition (CVD) technology is able to produce a controlled number of high quality graphene monolayers on large area of high-refractive index substrate. It was used in [8] for manufacturing of double-layer gratings of nanosize, in width, CVD-graphene strips on a substrate of polished float-zone silicon, for infrared sensing. To pattern the strips out of graphene sheet, 100-keV electron beam lithography and etching in oxygen plasma were applied.

Still, the mentioned above technologies are expensive. In order to reduce the cost and the time of research and development, scientists use the preceding modelling of the electromagnetic properties of the patterned graphene. Here, of crucial importance is the availability of the surface conductivity of non-patterned zero-thickness graphene in analytical form, known as Drude model or more sophisticated Kubo formalism [16]. Still, several aspects are non-trivial for an accurate modelling and must be fully accounted for: extremely small (1-2 nm) thickness of graphene, its finite and frequency-dependent conductivity, presence of sharp edges, and presence of dielectric substrates and superstrates. Comparative reviews of techniques, employed for such a modelling, can be found in [57] together with discussions of their limitations. In particular, it is emphasized that the Fourier-expansion technique (also known as “rigorous coupled-wave analysis”) is divergent in the H-polarization case [25], while commercial codes require introduction of nanoscale thickness of graphene that entails unnecessarily fine meshing and prohibitively large computation time [19]. Two analytical-numerical approaches stand out in this area: the method of SIE solved using the Nystrom discretisations [22,58,59] and the MAR-Galerkin applied to SIE or to other equivalent equations, casting them to the Fredholm second-kind matrix equations [24,60].

As mentioned above, our goals are related to the analysis of electromagnetics of graphene-strip DG on the substrate. Here, at first we have to adapt the MAR-RHP and MAR-IDFT techniques to the wave scattering by a grating of flat graphene strips lying on a flat dielectric substrate. Such a modification for the graphene strips has not been done; it has also a great advantage before MAR-Galerkin technique in the absence of numerical integrations needed to fill in the matrix equation.

Second, with the aid of such a trusted and efficient instrument, we can accurately analyze the fine resonance effects. In the H-polarization case (magnetic field being parallel to the strips), we can study the resonances on PMs of graphene strips that are electrostatically tunable and appear at low frequencies. Note that these resonances are already exploited in the mid-infrared bio and chemo-sensors [3,8]. In the E-polarization (electric field being parallel to the strips), no such modes exist.

Besides, in the both polarizations, we can focus our research on the so-called LM resonances, which do not exist on suspended strip gratings.

The LMs, which are in the focus of our study, need a short introduction. They exist in nearly all periodic open resonators, however, have received no attention or been overlooked until the 2000s; sometimes, they have been misinterpreted because of their ultra-large Q-factors and extreme closeness to the RAs. Most probably, they were first time revealed in [31] on the periodically modulated impedance plane, however, they were largely forgotten later. Now, they are intensively studied [24,58-68] and find important applications. This is because they are found responsible for several remarkable effects, greatly enhancing them due to huge Q-factors [65-68]. As known, if the periodicity is vanishing, their complex-valued natural frequencies approach the purely real-valued values and hence their Q-factors tend to infinity. As a consequence, accurate quantification of the ultra-fine LM resonances is a huge challenge for the existing commercial codes. In contrast, our MAR-RHP based full-wave meshless algorithm is fully adequate to that task.

1.3 Methods of diffraction theory used in the thesis

Essentials of MAR. Recent progress in the fields of nano-optics and photonics, driven by innovations in materials like graphene, have sparked significant interest in developing robust electromagnetic solvers for applications in THz and infrared technologies. Among these solvers, IE formulations and associated discretization techniques have gained prominence. They offer the advantage of automatically

satisfying radiation conditions and often defining unknown functions within finite supports. However, one can see that results obtained using commercial software typically require post-validation, comparing them against closed-form expressions, experimental measurements, or asymptotic solutions. This is necessary because, in general, it is impossible to establish the existence of a solution for arbitrary IE or the convergence of arbitrary discretization schemes beforehand [69,70].

An exception to this rule is the Fredholm second-kind IE, for which the convergence of discretization schemes that keep the compressing nature of IE operator, can be confidently stated, and truncation errors can be controlled. Examples are the Magnetic Field IE for closed PEC smooth objects and the Muller Boundary IE for dielectric smooth objects.

A broad class of wave propagation, radiation, and scattering problems, especially those involving open scatterers, objects with wedges, or planar surfaces, can be equivalently reformulated as singular IE. However, the Fredholm theory does not apply in these cases. This challenge can be surmounted through the use of the MAR. MAR encompasses a family of methods that transform first-kind weakly singular and various strongly SIE into second-kind integral or matrix equations, to which the generalized Fredholm theory, as advanced by Steinberg, is applicable. The term "Method of Analytical Regularization" was first introduced in Muskhelishvili's 1953 book 'Singular Integral Equations' and is sometimes interchangeably called the semi-inversion method. The fundamental concept is relatively straightforward yet intriguing: identify an appropriate operator that encapsulates the most singular aspect of the integral operator in question and conduct its analytical inversion. This operator can be chosen in various ways, depending on the specific problem, such as the static component, the high-frequency component, or a frequency-dependent canonical-shaped part.

Functional techniques, like Titchmarsh, Wiener-Hopf, Cauchy, Abel, and RHP methods, can be employed to achieve the analytical inversion of the static or the high-frequency part of the integral operator. In contrast, canonical-shaped problems can be tackled through the separation of variables that delivers the inversion of selected part.

In certain scenarios, both analytical regularization and the discretization of the IE are carried out simultaneously, known as analytical preconditioning. By selecting the eigenfunctions of a suitable singular part of the integral operator as expansion functions and applying Galerkin projection, a perfect preconditioner is established, rendering the resulting matrix operator of the Fredholm second kind. In general, the Fredholm theory can be applied if the discretized operator can be expressed as the sum of an invertible operator (with a doubly continuous inverse operator) and a completely continuous operator. When convergence is guaranteed, the precision of computations can be readily controlled by adjusting the matrix truncation order, theoretically achieving machine precision. This surpasses the capabilities of commercial software available today [70].

Although the MAR-based algorithms offer guaranteed convergence according to general theory, practical validation of the results is essential. While validation through comparison with commercial software is feasible, it is often impractical due to the superior accuracy of MAR-based codes. Consequently, adequate validation must rely on results obtained by other equally accurate techniques. Such techniques are limited, and typically, only two are available:

1) The method of separation of variables, applicable to simple-shaped scatterers like circular cylinders and spheres, which yields convergent series in terms of explicitly given special functions.
2) The Nystrom-type discretization, a well-grounded approach to numerically solving SIE. In this case, convergence is not derived from the Fredholm theory but from the theorems on the interpolation-type quadrature formulas, which account for both the IE singularities and the edge behavior of the unknowns.

In this thesis, we reduce the wave-scattering problems to certain dual series equations (DSE) for the Floquet harmonic (i.e. diffraction order) amplitudes and convert them to the Fredholm second kind infinite-matrix equations. In the case of graphene-strip grating, such DSEs are of two different forms.

In one of them appearing in the H-polarization case, after singling out the singular (divergent) part, the unknown coefficients have a weight in one of two series equations,

this weight is $|n|$. In the early 1960s, it was discovered that such a DSE is equivalent to the RHP, which can be solved analytically. This provides the semi-inversion for the DSE of the whole full-wave problem. In the other DSE, which appears in the E-polarization case, the mentioned weight is absent. Then, one can employ analytical regularization through the IDFT. In the either case, this yields a Fredholm second-kind matrix equation for the Floquet harmonic amplitudes.

DSE inversion using the Riemann-Hilbert Problem: Consider the DSE,

$$\begin{cases} \sum_{n=-\infty}^{\infty} x_n |n| e^{in\phi} = \sum_{n=-\infty}^{\infty} f_n e^{in\phi}, & \theta < |\phi| \le \pi \\ \sum_{n=-\infty}^{\infty} x_n e^{in\phi} = 0, & |\phi| \le \theta \end{cases} \tag{1.1}$$

where the coefficients f_n of the expansion of the right-hand side are known and belong to the class l_2, that is $\sum_{n=-\infty}^{\infty} |f_n|^2 < \infty$. Exact analytical solution of (1.1) is found as explained in [39,25,44,45] and can be conveniently written as

$$x_m = \sum_{n=-\infty}^{\infty} f_n T_{mn}(\theta), \quad m = 0, \pm 1, \pm 2, ... \tag{1.2}$$

$$T_{mn}(\theta) = \frac{-1^{m+n}}{2\,m-n} \left[P_m(-u)P_{n-1}(-u) - P_{m-1}(-u)P_n(-u) \right], \quad m \neq n, \tag{1.3}$$

$$T_{mn}(\theta) = \frac{1}{2|m|} \left\{ 1 + \sum_{s=1}^{|m|} t_s(-u)\, P_{s-1}(-u) \right\}, \quad m \neq 0 \tag{1.4}$$

$$T_{00}(\theta) = -\ln \frac{1-\cos\theta}{2}, \tag{1.5}$$

where $u = \cos\theta$, $t_0(-u) = 1$, $t_1(-u) = u$, $t_{s\ge 2}(-u) = P_s(-u) + 2uP_{s-1}(-u) + P_{s-2}(-u)$, and P_n are the Legendre polynomials.

Note that (1.2) is a numeric sequence of the class l_2, that is $\sum_{m=-\infty}^{\infty} |x_n|^2 < \infty$.

Details of the analytical derivation of closed forms (1.3) - (1.5) can be found in [39].

In Chapter 3, we apply the rigorous solution of RHP to invert analytically the static part of the full-wave scattering problem, associated with the graphene strip grating located in the free space and illuminated with the H-polarized plane wave. In Chapter 4, the same is done in the analysis of the eigenvalue problem for the H-polarized natural modes of the same configuration.

DSE inversion using the Inverse Discrete Fourier Transform: Consider the following DSE:

$$\sum_{n=-\infty}^{\infty} x_n e^{in\phi} = \begin{cases} \sum_{n=-\infty}^{\infty} f_n e^{in\phi}, & \delta < |\phi| \le \pi \\ 0, & |\phi| < \delta \end{cases} \tag{1.6}$$

Unlike the previous case, here we multiply both sides by $e^{-i\omega\phi}$ and integrate from 0 to 2π – see [25,44,45]. The result is

$$x_m = \sum_{n=-\infty}^{\infty} f_n S_{mn}\ (\delta)\quad ,\quad m = 0, \pm 1, \pm 2, \ldots \tag{1.7}$$

$$S_{mn}\ (\delta) = -\frac{\sin\delta\ (m-n)}{\pi\ (m-n)}, \quad m \neq n, \quad S_{mn}\ (\delta) = 1 - \frac{\delta}{\pi}. \tag{1.8}$$

Note that if $f_n,\ n = 0, \pm 1, \ldots$ is a number sequence of the class l_2, then x_n belongs to that class as well.

In Chapter 3, we apply the IDFT to invert analytically the static part of the full-wave scattering problem, associated with the graphene strip grating located in the free space and illuminated with the E-polarized plane wave. In Chapter 4, the same is done in the eigenvalue problem for the E-polarized natural modes of the same configuration.

The main merit of the briefly explained MAR techniques is the guaranteed convergence of the final code with progressively larger matrix truncation orders. If the convergence takes place, then it offers precise control over computational errors, allowing them, in principle, to be minimized to the level of machine precision.

Computational errors definition. In this work, we will visualize the rate of convergence computing the relative error, in the l_2-norm, of the solution found with varying truncation order N as compared to certain $N_{\max} >> N$, for various grating and slab parameters,

$$e(N) = \sum_{n=-N\max}^{+N\max} \left| x_n^{(N)} - x_n^{(N\max)} \right|^2 \left(\sum_{n=-N\max}^{+N\max} \left| x_n^{(N\max)} \right|^2 \right)^{-1}, \tag{1.9}$$

where $x_n^{(N)}$ and $x_n^{(N\max)}$ are the amplitudes of the Floquet harmonics, calculated with a variable truncation order N and at some large value of this order, $N_{\max}$, respectively (for instance, $N_{\max} = 400$), and the first of these sequences must be supplemented with zeros to the size of the second.

In the analysis of the wave scattering from gratings, normally the phenomena of reflection and transmission, in terms of the power, are interested in. Therefore, we define and compute the far-field error as a function of N,

$$e_\sigma(N) = \left| \sigma_N - \sigma_{400} \right| / \sigma_{400}, \tag{1.10}$$

where σ is either transmittance or reflectance.

1.4 Quantum Kubo model of graphene conductivity and impedance

The most widely adopted today quantum model of the electron mobility in graphene monolayer is the Kubo model [16]. Here, the graphene thickness is considered zero, and its surface conductivity $\sigma(\omega, \mu_c, \tau, T)$ depends on the cyclic frequency ω, chemical potential μ_c, electron relaxation time τ and temperature T. The conductivity consists of the intraband term,

$$\sigma_{\text{intra}} = \frac{i q_e^2 k_B T}{\pi \hbar^2 \left(\omega + i\tau^{-1} \right)} \left\{ \frac{\mu_c}{k_B T} + 2 \ln \left[1 + \exp\left(-\frac{\mu_c}{k_B T} \right) \right] \right\}, \tag{1.11}$$

where q_e is the charge of the electron, k_B is the Boltzmann constant, and $\hbar$ is the reduced Planck constant and the interband one, which is expressed as integral of known functions, however, has a simple approximation valid at $\mu_c >> k_B T$ [16],

$$\sigma_{\text{inter}} = \frac{iq_e^2}{4\pi\hbar} \ln \frac{2\mu_c - \left(\omega + i\tau^{-1}\right)\hbar}{2\mu_c + \left(\omega + i\tau^{-1}\right)\hbar} \tag{1.12}$$

Note that at the room temperature, T = 300 K, $k_B T = 0.026$ eV.

As well known, the fine structure of graphene has hexagonal cells, the size of which is around 10 nm. Therefore, non-local effects in conductivity can be neglected if a finite sample of graphene is wider than 100 nm. Besides, anisotropy of conductivity can be neglected if the cell size is negligible in comparison to the wavelength, i.e. to the frequencies that are as high as in the X-ray range.

The graphene complex-valued surface impedance, Z, is the inverse of the surface electron conductivity

$$\bar{Z} = Z_0 Z, \quad Z = Z_0^{-1}\left(\sigma_{\text{intra}} + \sigma_{\text{inter}}\right)^{-1} \tag{1.13}$$

Inspection of (1.11) and (1.12) shows (see [16]) shows that the interband conductivity, in absolute value, is much smaller than the intraband one, which is also called the Drude term, in the wide range from the statics to the far infrared light where the upper frequency bound, f_c, scales with the chemical potential. For instance, if $\tau = 1$ ps, $T = 300$ K, and $\mu_c = 0.25$ eV, then $|\sigma_{\text{inter}}| \le 0.1|\sigma_{\text{intra}}|$ at the frequencies up to 40 THz, while if $\mu_c = 0.39$ eV, then the same is valid at the frequencies up to 60 THz. Still, at the near infrared and visible light frequencies, the description of the surface conductivity of graphene should take into account both types of conductivity.

Provided that σ_{inter} can be neglected, the normalized surface impedance (or resistivity) of graphene can be taken as follows:

$$Z(\omega) \approx \left(Z_0 \sigma_{\text{intra}}\right)^{-1} = -i\left(\omega + i\tau^{-1}\right)\Omega^{-1}, \tag{1.14}$$

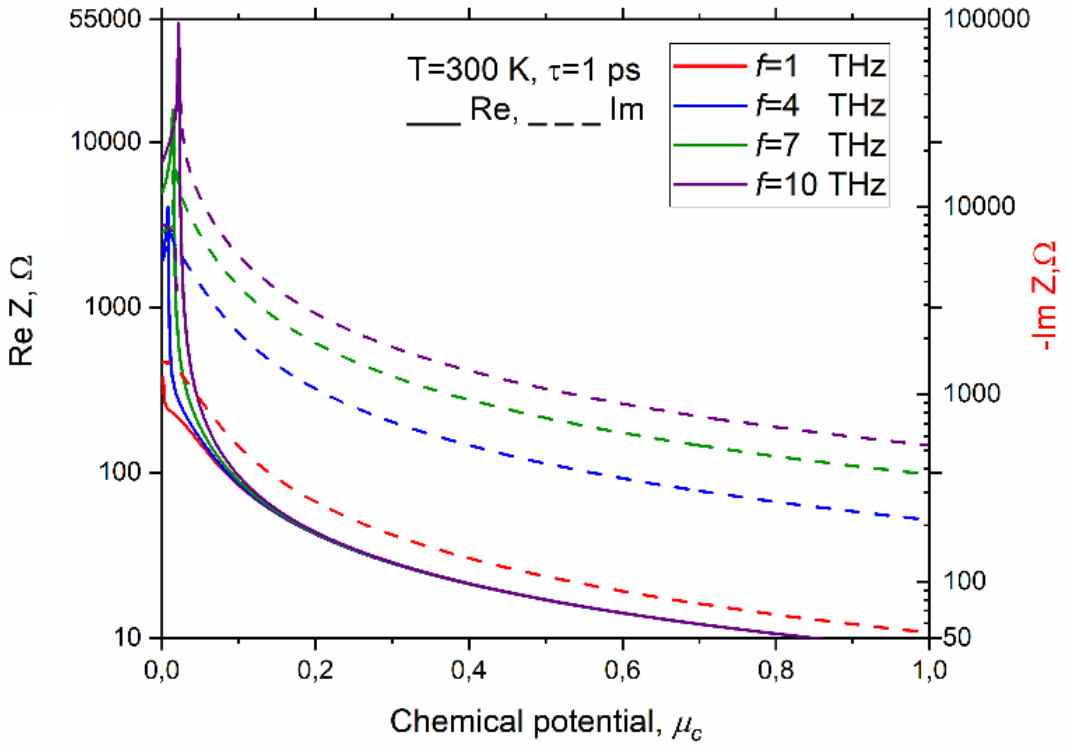

Figure 1.1. Real and imaginary parts of the graphene surface impedance Z_0Z versus the chemical potential at several frequencies in the THz range.

where

$$\Omega = \frac{q_e^2 k_B T Z_0}{\pi \hbar^2}\left\{\frac{\mu_c}{k_B T} + 2\ln\left[1+\exp\left(-\frac{\mu_c}{k_B T}\right)\right]\right\}, \qquad (1.15)$$

and Z_0 is the free-space impedance.

Here, the quantity Ω has dimensionality of the frequency, however, does not depend on the cyclic frequency.

The variation of the real and imaginary parts of Z with chemical potential, at several frequencies in the THz range, is demonstrated in Fig. 1.1.

Below, we will use full expression (1.13) in the numerical analysis and simplified expression (1.16) in the analytical description of the natural-mode frequencies.

Note that if the time dependence is chosen as $e^{-i\omega t}$ and $\mathrm{Im}\, Z < 0$ as is true for (1.14) that is known as inductive impedance behavior - then infinite sheet of graphene

can support the propagation of the plasmon wave [16]. However, close inspection of the Kubo expressions (1.11) and (1.12) shows that the imaginary parts of intraband and interband conductivities have opposite signs. Therefore, in principle, at extremely high frequencies where the latter one overweighs the former (see above), the plasmonic nature of graphene gets spoiled.

1.5 Plasmonic lasers and Lasing Eigenvalue Problem

In this thesis, the author studies the natural modes of the graphene-strip grating lying on the gain-material substrate, using the lasing eigenvalue problem (LEP). Therefore, both the topic of plasmonic lasers based on PMs of the arrays of plasmonic particles and the essentials of the LEP approach are introduced here.

DGs has been used in laser technology since long ago, however, as components, needed to manipulate the output light beam, e.g. improve its directionality [71].

Today, visible and infrared range lasers are various and since recently a promising trend in their development is the use, as working modes, the so-called LMs of various periodic arrays [72]. Such lasers are able to combine low emission thresholds and high directionality. Here, the most frequently met configuration is a two-periodic array of noble metal nanoparticles, laying on the flat substrate [73-78]. As a simpler alternative, one-periodic gratings, i.e. noble metal nanostrip arrays also attract attention [26]. It should be noted that in some of these works LMs are incorrectly called “lattice plasmon modes.” In reality, their nature is connected solely to the periodicity – so, no surprise that all-dielectric laser designs with LMs are also attracting great attention [79].

From the experiments, it is visible that finite gratings are able to demonstrate sharp resonances at the LM frequencies of infinite gratings, and the larger the gratings, the sharper the resonances. This observation is in line with theoretical analyses of the visible light scattering from finite arrays of noble-metal strips and wires [80-82,22]. To have high Q-factors of LMs on these arrays, the number of periods in finite grating should be counted in tens or hundreds.

Examining the publications on LM lasers, one can find the active regions shaped as either substrates or superstrates, which contain either internal quantum wells or quantum dot layers or the layers with dye molecules. Experiments show that in the presence of the pumping, the natural modes of such open cavities can be brought to the threshold of the lasing. Still, they have rather high thresholds because of the lossy nature of metals. Hence, keeping in mind that the graphene has lower losses than the metals, one can suggest a replacement of noble-metal elements with graphene ones.

In fact, the patterned graphene has already become attractive for building the lasers. One of the first proposals of such type was published in [83]; other potentialities are found in review [84]. More recently, spherical-particle and circular-wire laser configurations fully covered with graphene have been considered in [85,86]. Further, the LEP for a dimer made of two graphene-covered circular quantum wires has been studied in [87]. These works have demonstrated that such configurations are composite open resonators, which support natural modes of two families – PM of graphene covers and dielectric modes of non-graphene elements. The former modes have lower frequencies that the latter ones, and their thresholds are also lower if the cavity size is less than a few micrometers.

For a periodic open resonator, PMs co-exist with the LMs, which have escaped a systematic study so far. Although this gap can be filled using a variety of numerical techniques, the MAR-based ones occupy special place as they guarantee the convergence of the final code with progressively larger matrix truncation orders.

As the PMs are absent in the E-polarization case, it is especially interesting to study the LM frequencies and thresholds in that case and compare the to the H-case.

A usual approach to study the natural modes of the laser cavities has been the classical complex-frequency eigenvalue problem, where the presence of active regions is neglected and considered are the modes of passive open resonators. This approach is, however, not fully adequate because the existence of the threshold gain in the active region is not characterized.

From the viewpoint of the Maxwell theory of time-harmonic EM waves, the

lasing can be adequately modeled as the existence of the real-valued eigenfrequency (natural mode frequency) of an open resonator.

As known, the Complex Poynting Theorem, applied to the modes of arbitrary passive open resonator, the eigenfrequencies can be only complex [88], with non-zero imaginary parts – this follows from the radiation condition that entails finite radiation losses. Therefore, in order to have a real-valued eigenfrequency (no attenuation in time), an open resonator must contain a region, filled in with the gain material – active region.

The gain materials are "quantum" ones, in the sense that they rely on the quantum mechanisms to be able to demonstrate the inverse population of electronic levels and the stimulated emission of light. Various semiconductors, dye-doped polymers, or crystalline materials doped with ions of erbium or some other rare-earth elements display this type of behavior, under the pumping. In terms of macroscopic electromagnetic theory, this behavior can be conveniently expressed as single parameter - the imaginary part of the dielectric permittivity, $\mathrm{Im}\,\varepsilon$, or, equivalently, the refractive index $\mathrm{Im}\sqrt{\varepsilon}$ (for nonmagnetic materials). To correspond to the "negative losses" the sign of these values must be properly chosen. If the time dependence is $e^{-i\omega t}$, then the gain material has $\mathrm{Im}\,\varepsilon < 0$ and $\mathrm{Im}\sqrt{\varepsilon} < 0$.

Guided by these considerations, we can imagine arbitrary open cavity as shown in Fig. 1.2 where either the whole cavity or its part is filled in with a gain material and placed into a lossless outer medium. All such materials are nonmagnetic and therefore can be safely characterized with not ε but a complex refractive index with nonzero negative imaginary part, $\nu = \alpha - i\gamma$, where α is known refractive index and $\gamma > 0$ is unknown threshold gain index [88]. As already mentioned, arbitrary open cavity possess a discrete and infinite set of complex-valued natural frequencies (wavenumbers) k_s, each associated with certain non-zero field, $\{\mathbf{E}_s, \mathbf{H}_s\}$ (s = 1,2, …). These fields are the residues in the poles, which have no-zero negative imaginary parts, $\mathrm{Im}\,k_s(\gamma) < 0$, for the passive cavities with $\gamma < 0$. The gain material in the active region

enables compensation for the radiation and ohmic losses that yields the real-valued natural frequencies ($k_s = \mathrm{Re}\, k_s$).

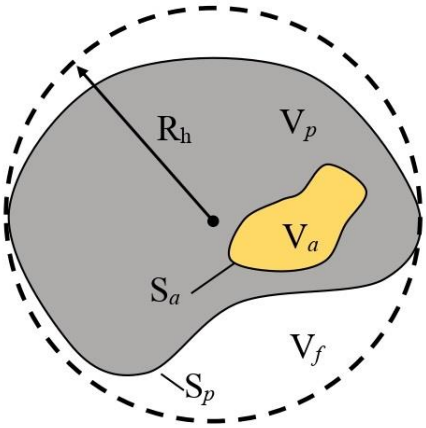

Fig. 1.2. Cross-sectional geometry of arbitrary open resonator containing active region, V_a. Here, R_h is the radius of the open resonator, i.e. the sphere containing all its components, V_p and V_f are the passive-dielectric and free-space domains of the resonator - see [88].

The related threshold gain value $\gamma_s > 0$ is mode-specific, i.e. depends on the mode type. From the mathematical point of view, the pair of ordered numbers k_s and γ_s, and the associated modal fields solve the source-free eigenvalue problem, which is the same as the scattering problem but without the incident field. This problem is the LEP. The modes as solutions to LEP automatically satisfy the classical definition of the lasing threshold, “total gain = total loss” [88].

Here, the fact that the LEP is linear problem should not be a surprise because at the threshold the field amplitude of a real laser as dynamic source is zero.

As mentioned, real value for k_s indicates that the natural mode at the lasing threshold does not experience time decay. What is worth mentioning is that the node field does not grow at infinity as $e^{-\mathrm{Im} k_s(\gamma) R} < 0$. Instead, it behaves as a cylindrical wave, in 2-D, or a spherical wave, in 3-D, and satisfies usual Sommerfeld or Silver-Muller condition of radiation, respectively.

Since 2004, the LEP has been applied to the analysis of the threshold conditions for the modes of various 1-D and 2-D cavities with active regions: Fabry-Perot active cavity between two Bragg reflectors [89], stand-alone circular ones [90], dimers of them [91] and cyclic photonic molecules [92], kite-shaped [93], elliptic [94], and other ones. Important result was the proof that the threshold is inverse proportional to the product of the Q-factor and the overlap factor between the mode electric field and the active region [88].

Periodic laser configurations have also been studied: this was an infinite grating of circular quantum wires [95] and a binary grating of alternating circular quantum wires and silver wire [96]. In particular, it was found that the LMs can have lower thresholds than the PMs on the silver wires.

More recently, LEP approach has been applied to the modes of 2-D noble-metal nanolasers in the shape of silver strip [97] and silver tube [98] inside the circular "quantum wire." A graphene nanotube laser and a dimer of such nanotubes, with the gain-material inner filling, were considered in [88].

For the proper positioning, one can keep in mind that the other LEP-like approaches exist, see [99-103], where the threshold gain is characterized, instead of γ, with the aid of $\mathrm{Im}\,\varepsilon < 0$ or so-called "gain per wavelength," that is the product, $g = k\gamma$.

As a final remark, we point out to the fact that the gain actually always depends on the frequency, with a maximum at a certain central frequency, say, ω_c, which depends on the material. To reflect this dependence, one can introduce the gain index into the LEP as $\gamma = \tilde{\gamma}\exp[-C(\omega^2 - \omega_c^2)]$ and search for the mode-specific eigenvalue pairs as $(k_s, \bar{\gamma}_s)$.

Conclusions to Chapter 1

In this chapter, we have reviewed briefly the role of diffraction gratings in optics and microwaves and emphasized their applications in sensors, filters, and antennas.

We have also presented some essentials on the theoretical descriptions of wave scattering from *flat strip gratings*, assuming their infinite extent. Being a chapter of the general theory of DGs, research into the scattering from strip gratings and associated eigenvalue problems, including two orthogonal polarizations, started from the PEC-strip DGs. Here, two variations of MAR are pivotal: MAR-RHP and MAR-Galerkin, which provide mathematically guaranteed convergence and have other merits. Later, the both were modified to treat the imperfect-strip DGs. We emphasize the LM resonances in both polarizations, underlining their significance in diverse applications.

Further, we have briefly explained the versions of MAR methods used in the thesis. Namely, the Riemann-Hilbert Problem and the Inverse Discrete Fourier Transform applied further in wave scattering from graphene-strip gratings are discussed, resulting in the Fredholm second-kind matrix equations for the field Floquet harmonics.

In addition, we present a summary on the quantum Kubo formalism, which provides analytical description of the dependence of graphene's conductivity on the frequency, electron relaxation time, and chemical potential.

Finally, the chapter discusses the Lasing Eigenvalue Problem (LEP) for open resonators equipped with active regions. The LEP relies on the already established discreteness of the complex frequencies of the open resonator natural modes. However, noting that the lasing can be understood as a stationary emission, LEP is tailored specifically to access not only the real-valued frequency but also the value of the gain in the active region, needed to make the natural frequency real.

Combining LEP with MAR's benefits, such as guaranteed convergence and precise error control, the threshold conditions for the modes of graphene-strip grating on the gain-material substrate can be accurately studied.

CHAPTER 2
AUXILIARY PROBLEM: SCATTERING OF PLANE WAVES FROM PERFECTLY ELECTRICALLY CONDUCTING STRIP GRATING ON DIELECTRIC SUBSTRATE

This chapter discusses the H- and E-polarized plane-wave scattering from an infinite flat grating of PEC strips, placed on the interface of a dielectric slab. We reduce each of these problems to a DSE for the complex amplitudes of the Floquet spatial harmonics. Then we perform analytical regularization of that equation, based on the inversion of the static part of the problem with the aid of the RHP analytical solution. In either case this yields a Fredholm second-kind infinite matrix equation, numerical solution of which has a guaranteed convergence. Numerical results obtained demonstrate how the rate of convergence depends on the geometrical parameters and then concentrate on the resonance effects in the reflection and transmission. The results of chapter 2 were published in [A4, A5, A13-A16].

2.1 Scattering problem formulation

Consider infinite flat grating of PEC strips with zero thickness and width d, located in the plane $y = 0$ with period p (Fig. 2.1). This plane is the top interface of a homogeneous dielectric layer (substrate) of the thickness h and relative dielectric permittivity ε. The H or E-polarized plane wave is incident at the angle α and depends on time as $e^{-i\omega t}$, where ω is the cyclic frequency.

The field components are $(E_x, E_y, 0)$ and $(0, 0, H_z)$ in the case of the H-polarization, however, $(0, 0, E_z)$ and $(H_x, H_y, 0)$ in the case of the E-polarization. It is convenient to choose H_z for the H-polarization and E_z for the E-polarization as the "basic" component; we denote it $U(\mathrm{x}, \mathrm{y})$ in both cases.

Thus, thee given incident field is a plane wave,

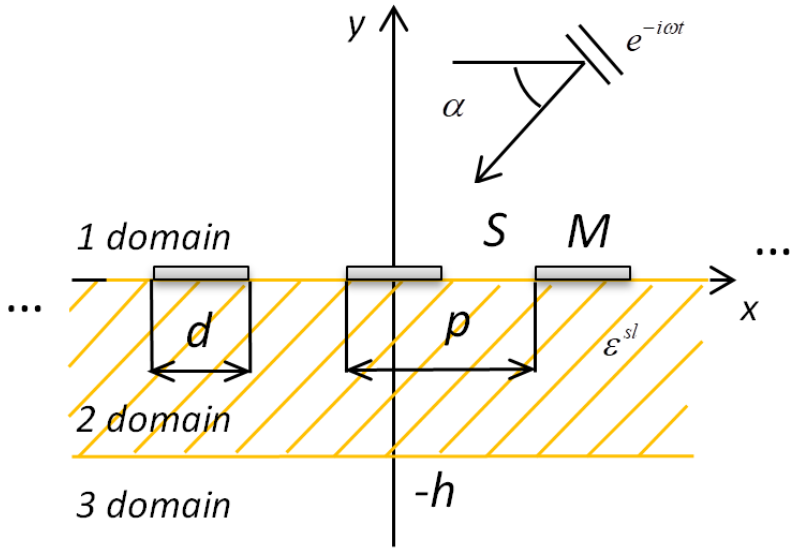

Figure 2.1. The cross-sectional geometry of a flat PEC strip grating on top of a dielectric layer, illuminated by a plane wave.

$$U^{in}(x,y)=\mathrm{e}^{-ik_0 y\sin\alpha-ik_0 x\cos\alpha},\quad y>0, \tag{2.1}$$

where $k_0=\omega/c=\omega(\varepsilon_0\mu_0)^{1/2}$ and $c=1/(\varepsilon_0\mu_0)^{1/2}$, $\kappa=p/\lambda$.

Then the total field is a sum, $U^{tot}=U^{in}+U^{(1)}$, in the domain #1, and $U^{tot}=U^{(2,3)}$ in the domains ##2,3. Thus, we obtain the following boundary value problem for $U=U^{(j)}$, $j=1,2,3$:

(I) it must satisfy the 2-D Helmholtz equation everywhere outside the strips and the slab interfaces,

$$\left(\nabla^2+k_0^2\varepsilon^{(j)}\right)U^{(j)}(\vec{r})=0,\quad y\neq 0, y\neq -h,\ \ j=1,2,3, \tag{2.2}$$

where we mean $\varepsilon^{(1)}=\varepsilon^{(3)}=1$, $\varepsilon^{(2)}=\varepsilon$.

(II) the PEC boundary condition at the strips, i.e. $\vec{E}_{tg}(\vec{r})=0$ at $\vec{r}\in M:\{y=0,|x-np|<d/2, n=0,\pm1,\pm2,...\}$, that means $\vec{E}_{tg}$, or

in the case of the H-polarization, $E_x=0$, or

$$\partial U^{(1)} / \partial y + \partial U^{in} / \partial y = 0, \quad \partial U^{(2)} / \partial y = 0, \tag{2.3-a}$$

in the case of the E-polarization, $E_z = 0,$ or

$$U^{(1)} + U^{in} = 0, \quad U^{(2)} = 0, \tag{2.3-b}$$

and at the slots $\vec{r} \in S = \mathrm{Re} \backslash M$ of the upper interface,
in the case of the H-polarization, H_z and E_x are continuous,

$$U^{(1)} + U^{in} = U^{(2)}, \ (\partial U^{(1)} + \partial U^{in}) / \partial y = \varepsilon^{-1} \partial U^{(2)} / \partial y, \tag{2.4-a}$$

in the case of the E-polarization, E_z and H_x are continuous,

$$U^{(1)} + U^{in} = U^{(2)}, \ (\partial U^{(1)} + \partial U^{in}) / \partial y = \partial U^{(2)} / \partial y, \tag{2.4-b}$$

the transmission conditions at the whole lower interface, y = - h, $x \in \mathrm{Re} : \{-\infty < x < +\infty\}$, i.e. H_z and
in the case of the *H*-polarization, H_z and E_x are continuous,

$$U^{(2)} = U^{(3)}, \ \varepsilon^{-1} \partial U^{(2)} / \partial y = \partial U^{(3)} / \partial y \,, \tag{2.5-a}$$

in the case of the E-polarization, E_z and H_x are continuous,

$$U^{(2)} = U^{(3)}, \partial U^{(2)} / \partial y = \partial U^{(3)} / \partial y \,, \tag{2.5-b}$$

(III) the radiation condition, which means that at $y \to \pm\infty$ the scattered field must contain only "outgoing" waves, and (IV) the condition of local finiteness of power: the power, stored in any finite space domain *D* tends to zero if $D \to 0$; this condition determines the edge behavior of the function *U*: it must tend to zero as a square root of the distance to the edge.

Additionally, the periodicity of the domain *M*, together with the shape of (2.1), entails the quasi-periodicity property,

$$U(x+p)=\mathrm{e}^{-ik_0 p\cos\alpha}U(x) \tag{2.6}$$

which enables reducing the analysis to single period of the scatterer.

Conditions (I)–(IV) provide the uniqueness of the solution: if the function U exists, then it is unique.

2.2 Analytical regularization using the Riemann-Hilbert Problem method

We choose H_z for the *H*-polarization and E_z for the *E*-polarization as the "basic " component, we denote it as $U(x,y)$ in both cases.

Thanks to the quasi-periodicity, the scattered field in the upper half-space (domain #1) is sought as a Floquet series. By introducing dimensionless notations,

$$\phi=2\pi x/\ p,\quad \psi=2\pi y/\ p,\quad \theta=\pi d/\ p,\quad \xi=2\pi h/\ p,\quad \kappa=p/\lambda, \tag{2.7}$$

this is

$$U^{(1)}=\sum_{n=-\infty}^{\infty}a_n e^{i(\gamma_n\psi+\beta_n\phi)},\quad \psi>0. \tag{2.8}$$

Here, the exponents that depend on the spatial coordinates *x* and *y* are called Floquet harmonics or diffraction orders. The field in the dielectric slab (domain #2) and the field in the lower half-space (domain #3) can be represented in a similar way, respectively,

$$U^{(2)}=\sum_{n=-\infty}^{\infty}\left(b_n e^{i\gamma_n^{sl}\psi}+c_n e^{-i\gamma_n^{sl}\psi}\right)e^{i\beta_n\phi},\ \ 0>\psi>-\xi, \tag{2.9}$$

$$U^{(3)}=\sum_{n=-\infty}^{\infty}d_n e^{i(-\gamma_n\psi+\beta_n\phi)},\ \ \psi<-\xi. \tag{2.10}$$

The coefficients a_n,b_n,c_n and d_n are as yet unknown complex numbers (amplitudes of Floquet harmonics); other notations are as follows:

$$\gamma_n=\left(\kappa^2-\beta_n^2\right)^{1/2},\ \gamma_n^{sl}=\left(\kappa^2\varepsilon-\beta_n^2\right)^{1/2},\ \beta_n=n-\beta_0, \tag{2.11}$$

where $\gamma_0 = \kappa \sin\alpha$, $\beta_0 = \kappa \cos\alpha$, and the root branch for γ_n is chosen such that $\mathrm{Re}\,\gamma_n \geq 0$ or $\mathrm{Im}\,\gamma_n \geq 0$. Then, as it is easy to see, the field $U(x,y)$ satisfies equations (2.2) and the radiation condition.

The reflectance and transmittance are the power fractions reflected from and transmitted through the slab with grating. They are expressed via the Floquet harmonic amplitudes as

$$P_{ref} = \gamma_0^{-1} \sum_{|n-\kappa\cos\beta|<\kappa} \gamma_n |a_n|^2, \quad P_{tr} = \gamma_0^{-1} \sum_{|n-\kappa\cos\beta|<\kappa} \gamma_n |d_n|^2. \tag{2.12}$$

Note that the following law of power conservation applies: $P_{ref} + P_{tr} = 1$ (if the substrate is lossless) or $P_{ref} + P_{tr} + P_{abs} = 1$ (if it is lossy, with P_{abs} for the power absorbed by the substrate) – see Fig 2.2.

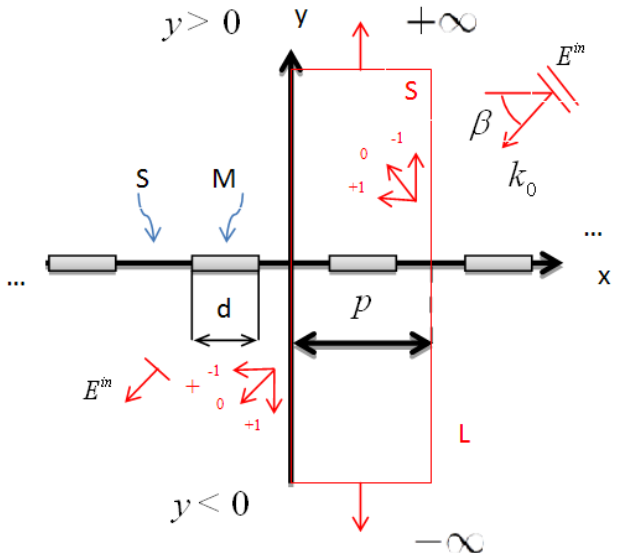

Figure – 2.2 Integration contour L in the derivation of the law of power conservation with the aid of the Complex Poynting Theorem.

To derive the power conservation law, it is necessary to apply the complex Poynting theorem to the total field function and its complex conjugate in the elementary period of the grating, bounded by the contour L.

Next, we consider the H and E polarizations separately.

2.2.1 H-polarization, basic equations

The problem is reduced to finding the amplitudes of the Floquet harmonics, for which we need to use the boundary conditions (2.3) - (2.5). Substituting (2.8) and (2.9) into the conditions (2.5a), we obtain

$$\begin{cases} \sum\limits_{n=-\infty}^{\infty}\left(b_n e^{-i\gamma_n^{sl}\xi}+c_n e^{i\gamma_n^{sl}\xi}\right)e^{i\beta_n\phi}=\sum\limits_{n=-\infty}^{\infty}d_n e^{i\gamma_n\xi+i\beta_n\phi} \\ \frac{i}{\varepsilon}\sum\limits_{n=-\infty}^{\infty}\left(\gamma_n^{sl}b_n e^{-i\gamma_n^{sl}\xi}-\gamma_n^{sl}c_n e^{i\gamma_n^{sl}\xi}\right)e^{i\beta_n\phi}=\sum\limits_{n=-\infty}^{\infty}-i\gamma_n d_n e^{i\gamma_n\xi+i\beta_n\phi} \end{cases} \tag{2.13}$$

Since these series coincide on the entire period, we replace them with term-wise equations for each value of the index $n = 0,\pm1,\pm2,\ldots$ and exclude the unknowns b_n and c_n, expressing them via d_n using the following expressions:

$$b_n=\frac{d_n}{2}\left(1-\frac{\gamma_n\varepsilon}{\gamma_n^{sl}}\right)e^{i(\gamma_n^{sl}+\gamma_n)\xi},\ c_n=\frac{d_n}{2}\left(1+\frac{\gamma_n\varepsilon}{\gamma_n^{sl}}\right)e^{-i(\gamma_n^{sl}-\gamma_n)\xi} \tag{2.14}$$

According to the PEC conditions (2.3a) on the strips, $\vec{r}\in M$, we have

$$-\kappa\sin\alpha e^{i\beta_0\phi}+\sum_{n=-\infty}^{\infty}\gamma_n a_n e^{i\beta_n\phi}=0, \tag{2.15}$$

$$\sum_{n=-\infty}^{\infty}\left(i\gamma_n^{sl}b_n-i\gamma_n^{sl}c_n\right)e^{i\beta_n\phi}=0. \tag{2.16}$$

On the slots, $\vec{r}\in S$, the conditions (2.4a) yield

$$e^{i\beta_0\phi}+\sum_{n=-\infty}^{\infty}a_n e^{i\beta_n\phi}=\sum_{n=-\infty}^{\infty}\left(b_n+c_n\right)e^{i\beta_n\phi} \tag{2.17}$$

$$-\kappa\sin\alpha e^{i\beta_0\phi}+\sum_{n=-\infty}^{\infty}a_n\gamma_n e^{i\beta_n\phi}=\frac{1}{\varepsilon}\sum_{n=-\infty}^{\infty}\left(\gamma_n^{sl}b_n-\gamma_n^{sl}c_n\right)e^{i\beta_n\phi} \tag{2.18}$$

Thanks to (2.15) and (2.16), equation (2.18) is satisfied on the entire period. Therefore, on substituting (2.14) into d_n and introducing new coefficients ($n = 0,\pm1,\ldots$),

$$M_n = -\delta_{n,0}\kappa\sin\alpha + \gamma_n a_n, \tag{2.19}$$

where $\delta_{n,0}$ is the Kroenecker symbol, we see that

$$d_n = M_n \varepsilon e^{i\gamma_n \xi}\left[i\gamma_n^{sl}\sin(\gamma_n^{sl}\xi) + \gamma_n \varepsilon\cos(\gamma_n^{sl}\xi)\right]^{-1} \tag{2.20}$$

then, introducing, for convenience,

$$\Gamma_n^H = \left[\frac{1}{\gamma_n} - \frac{\varepsilon}{\gamma_n^{sl}}\frac{\left(\gamma_n^{sl}-\gamma_n\varepsilon\right)e^{i\gamma_n^{sl}\xi} + \left(\gamma_n^{sl}+\gamma_n\varepsilon\right)^{-i\gamma_n^{sl}\xi}}{\left(\gamma_n^{sl}-\gamma_n\varepsilon\right)e^{i\gamma_n^{sl}\xi} - \left(\gamma_n^{sl}+\gamma_n\varepsilon\right)e^{-i\gamma_n^{sl}\xi}}\right]^{-1}, \tag{2.21}$$

$$x_0 = M_0\left(\Gamma_0^H\right)^{-1} + 2, \quad x_n = M_n\left(\Gamma_n^H\right)^{-1}, \tag{2.22}$$

$$\Delta_n^H = |n| + i(1+\varepsilon)\Gamma_n^H \tag{2.23}$$

the expression (2.17) enables us to derive DSE:

$$\begin{cases} \sum\limits_{n=-\infty}^{\infty} x_n |n| e^{in\phi} = \sum\limits_{n=-\infty}^{\infty} x_n \Delta_n^H e^{in\phi} - i(1+\varepsilon)2\Gamma_0^H, \theta < |\phi| \le \pi, \\ \sum\limits_{n=-\infty}^{\infty} x_n e^{in\phi} = 0, \quad |\phi| < \theta, \end{cases} \tag{2.24}$$

Analysis of behavior of (2.21) if $n \to \infty$ shows that the weight function (2.23), which is under the sum in the right part of DSE (2.24), behaves as $\Delta_n^H = O(\kappa\cos\alpha) + O(\kappa^2/|n|) + O(e^{-|n|2\pi h/p})$. This means that the left hand part of DSE, which does not depend on frequency and other parameters, corresponds to the static part for the problem of the plane wave scattering from a grating in free space.

The left hand part of (2.24) forms the RHP on the unit circle, solution of which is known and expressed via the Plemelij-Sokhotskii formulas. Details of this procedure can be found in section 1.3, note that it exploits explicitly the edge condition (IV). When applied to the full equation (2.24), this yields an infinite matrix equation,

$$x_m = \sum_{n=-\infty}^{+\infty} A_{m,n}^H x_n + B_m^H, \quad m = 0, \pm1, \pm2, \ldots \tag{2.25}$$

$$A_{m,n} = \Delta_n(k_0, \varepsilon, h/p) T_{mn}(\theta), \quad B_m = -i(1+\varepsilon) 2\Gamma_0 T_{m0}(\theta). \tag{2.26}$$

The functions $T_{mn}(\theta)$ are expressed via the Legendre polynomials P_m of the argument $u = -\cos\theta$, see equations (1.3)-(1.5) in Chapter 1 and [25,44]. The large-index asymptotics of the Legendre polynomials allow seeing that the following inequalities hold true:

$$T_{mn}(\theta) \le \frac{const}{|m|^{1/2} |n|^{1/2} |m-n+1|} \tag{2.27}$$

$$\sum_{m,n=-\infty}^{+\infty} \left|A_{mn}\right|^2 < \infty, \qquad \sum_{m=-\infty}^{+\infty} \left|B_m\right|^2 < \infty \tag{2.28}$$

Hence, equation (2.25) is a Fredholm second kind matrix equation in the space of number sequences l_2 and hence the convergence of its numerical solution for progressively larger truncation numbers is mathematically guaranteed. Note that expressions (2.26) are combinations of elementary functions, need no numerical integrations, and hence can be easily computed with machine precision. This is an advantage before the other MAR-Galerkin technique, such as [45,47-52].

As mentioned, inspection of (2.23) shows the regularization, i.e. semi-inversion of DSE, is performed via the analytical inversion of the static part of the scattering problem, associated with the strip grating on free space (i.e. in the absence of the substrate). As can be expected, this worsens the convergence rate of the code based on the solution of (2.25), truncated to finite order *N*, with respect to the free space case

2.2.2 E-поляризація, basic equations

In the case the *E*-polarization the problem is also reduced to finding the amplitudes of the Floquet harmonics, for which we need to use boundary conditions (2.3) - (2.5).

Substituting series (2.8) and (2.9) in the condition (2.5b), we can find the unknown amplitudes

$$\begin{cases} \sum\limits_{n=-\infty}^{\infty}\left(b_n e^{-i\gamma_n^{sl}\xi}+c_n e^{i\gamma_n^{sl}\xi}\right)e^{-i\beta_n\phi}=\sum\limits_{n=-\infty}^{\infty}d_n e^{i\gamma_n\xi-i\beta_n\phi} \\ \sum\limits_{n=-\infty}^{\infty}\left(\gamma_n^{sl}b_n e^{-i\gamma_n^{sl}\xi}-\gamma_n^{sl}c_n e^{i\gamma_n^{sl}\xi}\right)e^{-i\beta_n\phi}=-\sum\limits_{n=-\infty}^{\infty}\gamma_n d_n e^{i\gamma_n\xi-i\beta_n\phi} \end{cases} \tag{2.29}$$

These equations, as in the case of H-polarization, can be replaced with term-wise equations $n = 0,\pm1,\pm2,\ldots$ and exclude the unknowns b_n and c_n, expressing them via d_n,

$$b_n=\frac{d_n}{2}\left(1-\frac{\gamma_n}{\gamma_n^{sl}}\right)e^{i(\gamma_n^{sl}+\gamma_n)\xi},\ c_n=\frac{d_n}{2}\left(1+\frac{\gamma_n}{\gamma_n^{sl}}\right)e^{-i(\gamma_n^{sl}-\gamma_n)\xi} \tag{2.30}$$

From the PEC conditions (2.3b) on the strips, it follows that

$$e^{-i\beta_0\phi}+\sum_{n=-\infty}^{\infty}a_n e^{-i\beta_n\phi}=0, \tag{2.31}$$

$$\sum_{n=-\infty}^{\infty}\left(b_n+c_n\right)e^{-i\beta_n\phi}=0\,. \tag{2.32}$$

On the slots, the continuity conditions (2.4b) give us

$$e^{-i\beta_0\phi}+\sum_{n=-\infty}^{\infty}a_n e^{-i\beta_n\phi}=\sum_{n=-\infty}^{\infty}\left(b_n+c_n\right)e^{-i\beta_n\phi} \tag{2.33}$$

$$-\kappa\sin\alpha e^{-i\beta_0\phi}+\sum_{n=-\infty}^{\infty}a_n\gamma_n e^{-i\beta_n\phi}=\sum_{n=-\infty}^{\infty}\left(\gamma_n^{sl}b_n-\gamma_n^{sl}c_n\right)e^{-i\beta_n\phi} \tag{2.34}$$

As equation (2.34) holds on the entire period, we are allowed to substitute there b_n and c_n on d_n from (2.30). Then, after introducing new coefficients ($n = 0, \pm1$),

$$x_n=\delta_{n,0}+a_n, \tag{2.35}$$

we arrive at the expression allowing to exclude d_n,

$$d_n=2x_n\gamma_n^{sl}e^{-i\gamma_n\phi}\left[\left(\gamma_n^{sl}-\gamma_n\right)e^{i\gamma_n^{sl}\phi}+\left(\gamma_n^{sl}+\gamma_n\right)e^{-i\gamma_n^{sl}\phi}\right]^{-1} \tag{2.36}$$

For convenience, we introduce the notations,

$$\Gamma_n^E = \left[\gamma_n - \gamma_n^{sl} \frac{\left(\gamma_n^{sl} - \gamma_n\right) e^{i\gamma_n^{sl}\xi} - \left(\gamma_n^{sl} + \gamma_n\right) e^{-i\gamma_n^{sl}\xi}}{\left(\gamma_n^{sl} - \gamma_n\right) e^{i\gamma_n^{sl}\xi} + \left(\gamma_n^{sl} + \gamma_n\right) e^{-i\gamma_n^{sl}\xi}} \right], \tag{2.37}$$

$$\Delta_n^E = |n| + i\Gamma_n^E, \tag{2.38}$$

Then, using (2.36), we arrive at DSE,

$$\begin{cases} \sum\limits_{n=-\infty}^{\infty} x_n |n| e^{in\phi} = \sum\limits_{n=-\infty}^{\infty} x_n \Delta_n^E e^{in\phi} - 2i\gamma_0, \ \theta < |\phi| \le \pi, \\ \sum\limits_{n=-\infty}^{\infty} x_n e^{in\phi} = 0, \quad |\phi| < \theta, \end{cases} \tag{2.39}$$

It should be noted that in order to derive the second equation of (2.39) we can use any of the boundary conditions that hold on the strips, i.e. either (2.31) or (2.32). If $n \to \infty$, then the weight functions in the right-hand part of (2.39) behaves as $\Delta_n^E = O(\kappa \cos\alpha) + O(\kappa^2 |n|^{-1}) + O(e^{-|n|2\pi h/p})$.

The left-hand part of (2.39), which does not depend on the frequency, forms the RHP on the unit circle in complex plane. The analytical solution of this RHP can be found using the Plemelij-Sokhotskii formulas [36,37,59]; see also [51]. This yields an infinite matrix equation,

$$x_m = \sum_{n=-\infty}^{+\infty} A_{m,n}^E x_n + B_m^E, \quad m = 0, \pm 1, \pm 2, ... \tag{2.40}$$

$$A_{m,n}^E = \Delta_n^E(\kappa, \varepsilon, h/p) T_{mn}(\theta), \quad B_m^E = -i2\gamma_0 T_{m0}(\theta). \tag{2.41}$$

where functions T_{mn} are the combinations of the Legendre polynomials, see (1.3) - (1.5).

Similar to the case of the H-polarization, the estimations) of these polynomials for large indices allows us to establish the estimations (2.27), which, in turn, prove that the following inequalities hold:

$$\sum_{m,n=-\infty}^{+\infty} \left| A_{mn} \right|^2 < \infty, \qquad \sum_{m=-\infty}^{+\infty} \left| B_m \right|^2 < \infty \tag{2.42}$$

This means that (2.40) is a Fredholm second kind matrix equation in the space of sequences l_2. Then the Fredholm theorems guarantee the convergence of the numerical solution if one takes the matrix truncation number *N* larger. Basically, this fact is well known since [59]. Still, the rate of convergence has apparently not been studied in detail.

2.3 Validation and results of numerical study of wave scattering

In this section, we present numerical results of studying the scattering of the H and E-polarized plane waves from an infinite flat grating of PEC strips located on the surface of a dielectric substrate, as shown in Fig. 2.1. As explained in sub-section 2.2, those problems are reduced to infinite matrix Fredholm equations of the second kind. Earlier works of this kind can be found in [36-38], and the grating on a dielectric substrate was considered only in [46], but the equations given therein are too complicated and there are no numerical results.

It should be added that the MAR-Galerkin technique has also been used to study wave scattering from such gratings - see [47-51]. Therefore, their results can be used as a reference. In these works, one can notice extremely sharp resonances, which, unfortunately, have not been studied. Note that we are able to obtain reliable numerical results that retain their controlled accuracy even in the sharpest resonances.

2.3.1 H-polarization: resonances on substrate and lattice modes

First of all, we need to make sure that the solution to the problem converges. To visualize the rate of convergence, we consider normal and inclined incidence, $\alpha = 90^o$ and 45^o, and select two values of the normalized frequency $\kappa = p/\lambda$, namely 14.1 and 100.1. We compute the relative error, using the formula (1.9) from section 1.3. Typical results of such computations are shown in Fig. 2.3.

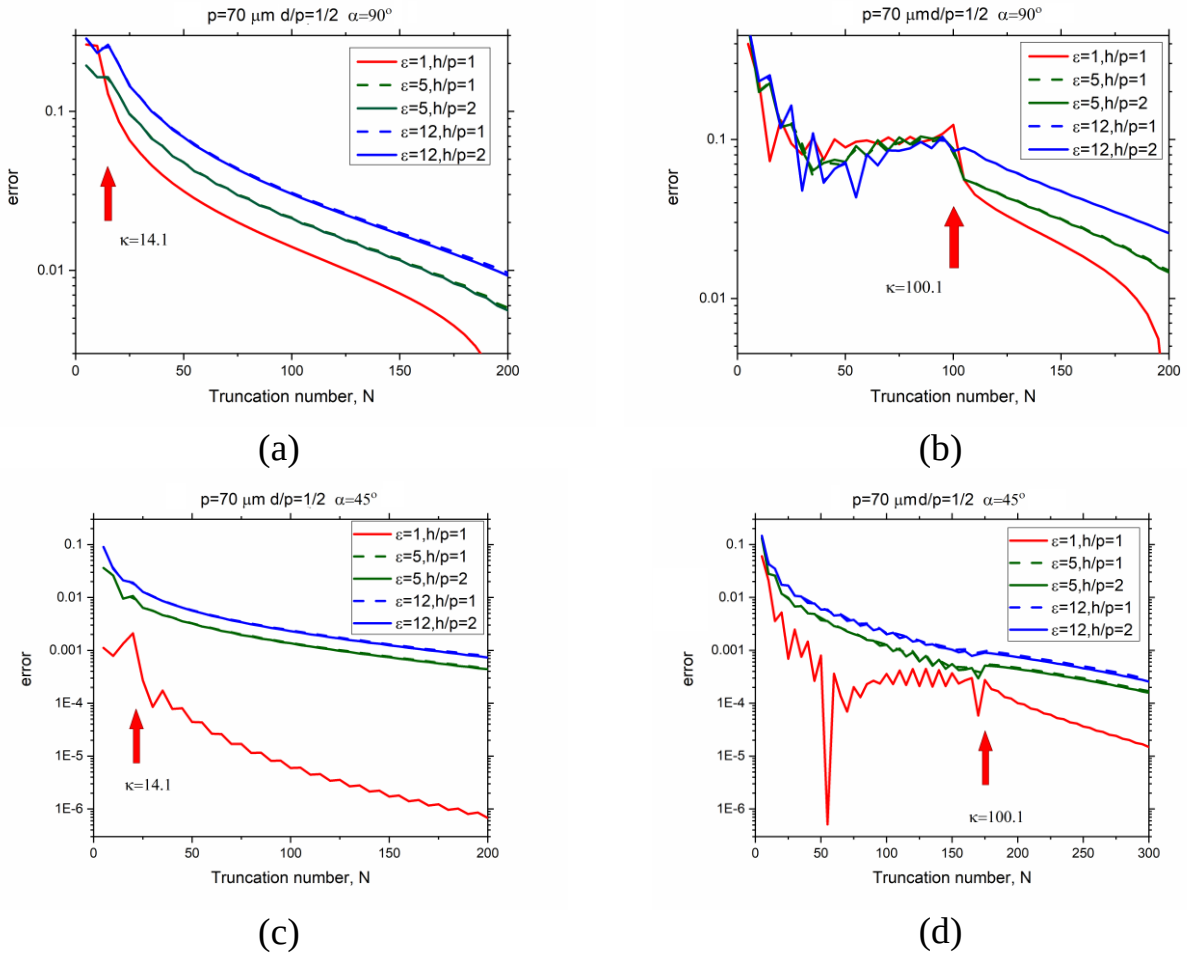

Figure. 2.3. The error, in the l_2-norm, in the computation of unknown coefficients versus the matrix truncation order for the grating with $\alpha = 90^o$ and 45^o, $d / p = 0.5$, and different parameters ε and h/p, as indicated in the inset. The normalized frequency is $\kappa = 14.1$ for (a) and (c), and $\kappa = 100.1$ for (b) and (d).

As can be seen, the computational error does indeed begin to decrease as the order N becomes larger than the normalized frequency, by an amount that slightly depends on h / λ and ε. It should be noted that since the reflectance of the grating and the transmittance through it have the form of finite sums (2.10), the error in their computation is not worse than the error in solution of the matrix equation.

We define and compute the far-field error as a function of N using the formula (1.10) from chapter 1. The results of computations are shown in Fig. 2.4. With an increase in the truncation order N over κ, marked by red arrows, the error decreases, i.e. the accuracy of the calculation increases.

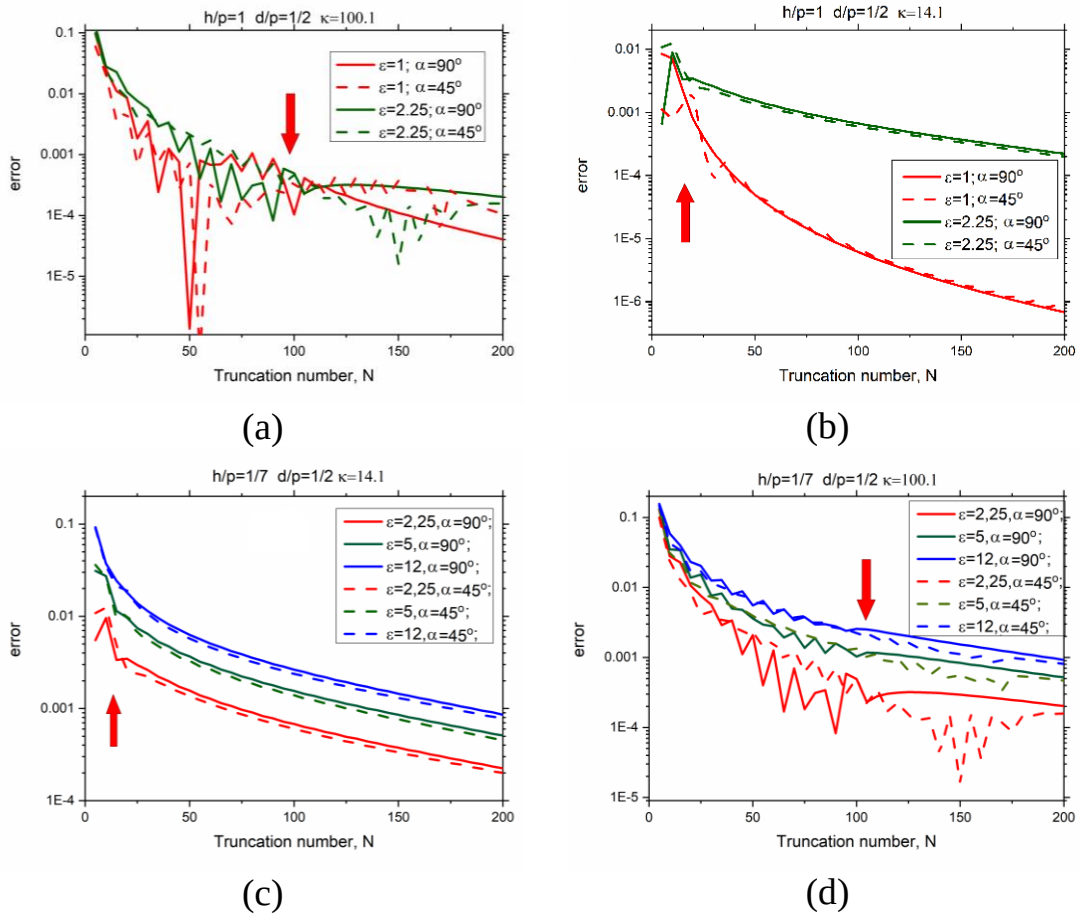

Figure 2.4. The far-field error versus the order of truncation for the grating with d/p = 0.5, angle of incidence $\alpha = 90^{o}$ and 45^{o}, and h/p and ε as indicated. $\kappa = 14.1$ (a), (c) and $\kappa = 100.1$ (b), (d).

As visible, the rate of convergence is the highest in the case of absence of dielectric layer, while thicker and optically denser slabs entail larger values of N to achieve the same accuracy. In contrast, the fill factor, d / p, and the incidence angle, α, do not change the rate of convergence.

Further, as a proof of validation, we present, in Fig. 2.5, a comparison of our results with those of [51], computed by a different accurate technique, MAR-Galerkin with Chebyshev's polynomials. Here, we show the absolute value of the H-polarization reflection coefficient (amplitude of the 0-th Floquest harmonic) of PEC strip grating on top of dielectric substrate versus the frequency in the range $\kappa \le 1$, where only the 0-th

Floquet harmonic of the scattered field is radiating. The data for freestanding strip array and for unloaded dielectric slab are also shown.

The corresponding curves visually overlap that is understandable because both methods are convergent and the orders of discretization provide 4-5 correct digits. A striking feature of the plot for the narrow-strip (d = 0.2p) grating on the thin (h = 0.2p) dielectric slab is a sharp total-reflectance peak at 57 GHz. This is a resonance on the LM, discussed below. Off resonance, the reflection is almost the same as for a bare slab.

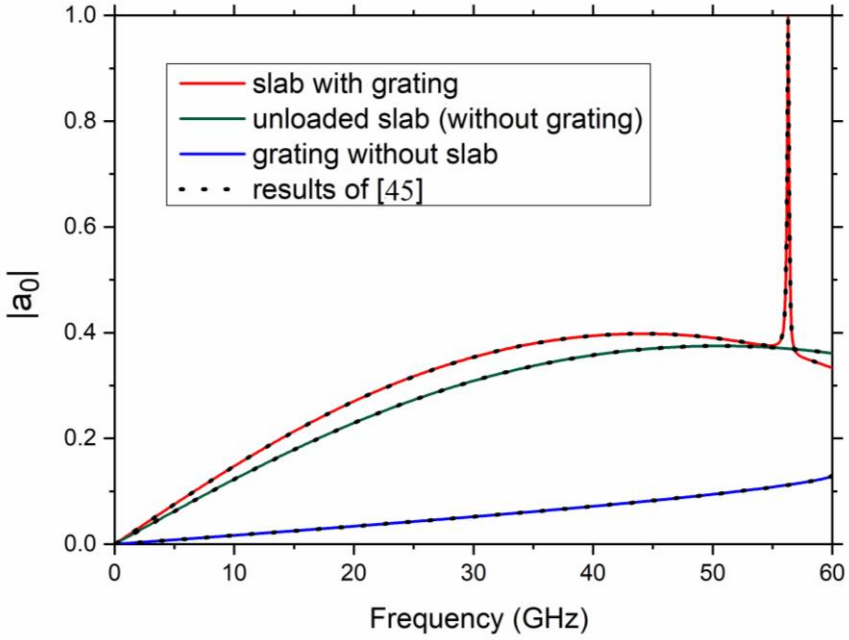

Figure 2.5. Comparison of the results of [51] and MAR-RHP using (2.47), for $p = 5$ mm, $d = 1$ mm, $h = 1$ mm, $\varepsilon = 2.2$ (i.e. d/p = h/p = 0.2). Absolute value of the amplitude reflection coefficient of strip grating on top of dielectric substrate versus the frequency in the single-mode range, $0 < \kappa < 1$, H-polarization. The plots for freestanding strip array and for bare dielectric slab are also shown.

After the verification of our code, we present, in Fig.2.6 (a), the plots of the reflectance (2.12) as a function of the normalized frequency, for three values of the strip width-to-period ratio, $d / p = 0.9, 0.5$ and 0.1, for the normal incidence. Note the sharp bends of all curves exactly at $\kappa = 1, 2, 3$ due to the RA of the $\pm n$-th index, which are the

roots of equations $\gamma_n = 0, \quad n = \pm 1, \pm 2, \ldots$ at $\cos\alpha = 0$. At lower frequency values, one can see the Fano-shape double extrema due to the resonances on the LM of the 1-st and higher orders, respectively.

Fig. 2.6 (b) is a zoom of the vicinity of the 1-st RA. As visible, if the PEC strips are narrow ($d/p << 1$), then the reflectance is low, however, in the resonance on the LM it becomes total, in a narrow range. Still, for half-period and wider strips ($d/p \geq 0.5$), the reflection is high everywhere except of the vicinity of the LM resonance, where it drops to a low value. Thus, a PEC-strip grating on a thin dielectric substrate is able to demonstrate both extraordinary full-reflection and extraordinary full-transmission effects, in the LM resonances.

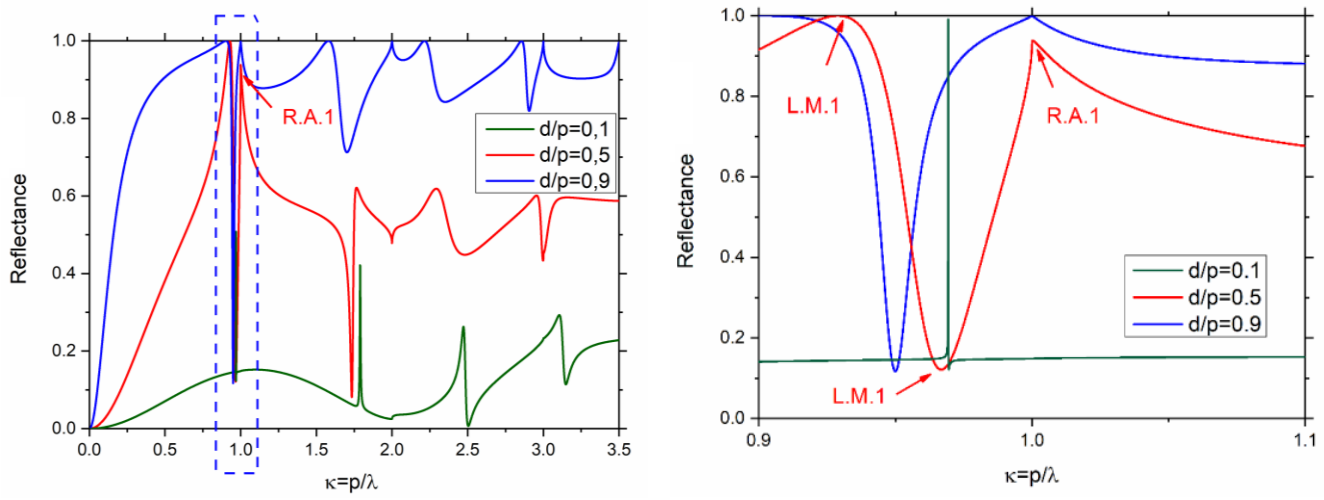

Figure 2.6. The reflectance of the on-substrate grating versus the normalized frequency for $h/p = 1/7$, $\varepsilon = 2.25$ (Teflon, Polyethylene), and 3 values of the filling factor, i.e. the strip-to-period ratio (a), and the zoom of (a) in the marked interval near $\kappa = 1$ (b).

These and other results presented below have been computed with truncation number N = 50 that provides 8 or more correct digits in the reflectance at all studied frequencies.

To investigate the resonances on the LM, we plot, in Fig. 2.7, the curves of the reflectance (2.12) as a function of the normalized frequency κ, for the H-polarized plane wave, normally incident on a grating with equal strips and slots and two values of relative dielectric permittivity, 2.2 (Teflon, Polyethylene) and 3.8 (fused quartz). The plot of the same quantity for a grating without substrate ($\varepsilon = 1$) is also shown for comparison.

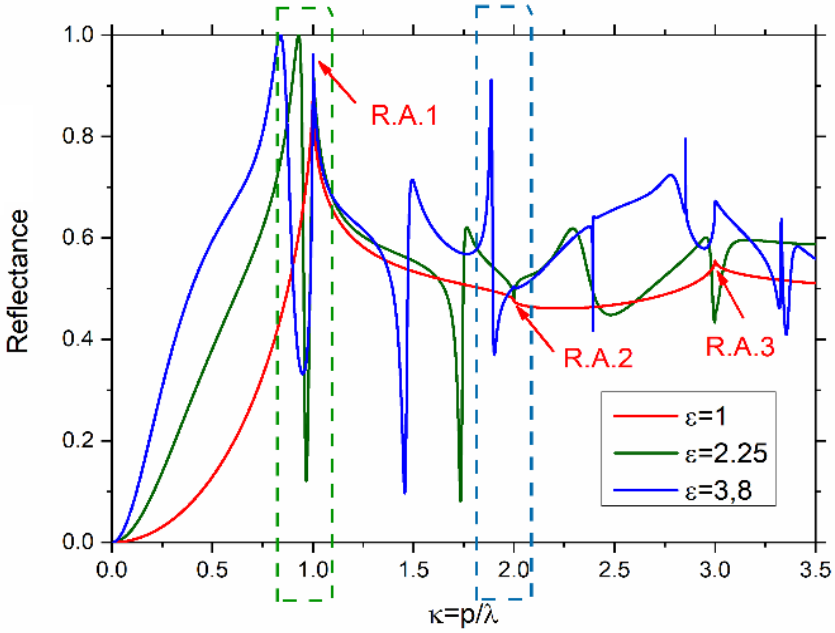

(a)

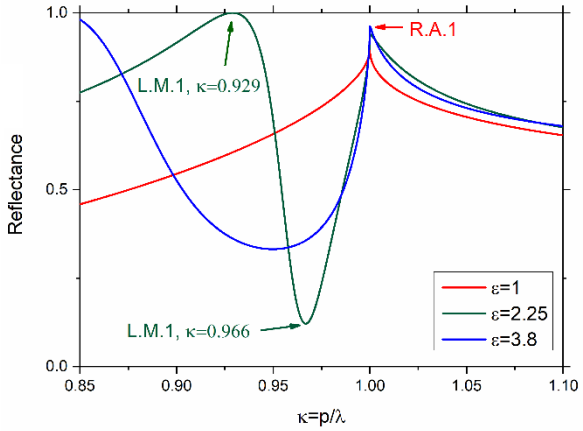

(b)

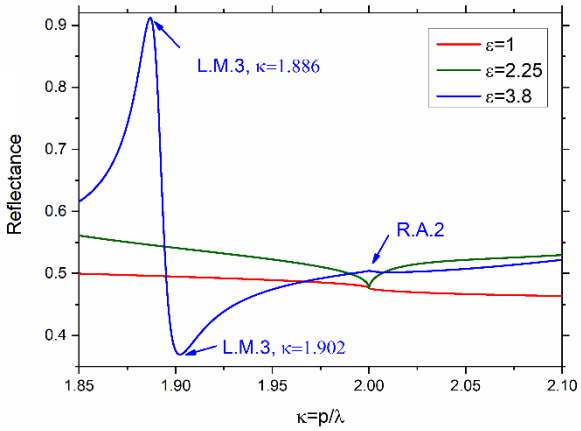

(c)

Figure 2.7. The same as in Fig. 2.5 however for $d/p = 0.5$, $h/p = 1/7$, and three values of the permittivity, $\varepsilon = 1$, 2.25, and 3.8 (fused quartz) (a), and the zooms of (a) in the marked intervals near $\kappa = 1$ (b), and $\kappa = 2$ (c).

Sharp resonances slightly below the RA wavelengths, at the normal incidence, are well visible. However, they are absent if the dielectric slab is absent, i.e. PEC strip grating is suspended in the free space. On panels (b) and (c), we show the zooms of the vicinities of the 1-st and the 2-nd RA, respectively.

At the frequencies, corresponding to the lattice resonances, we visualize the near field patterns – see Figs. 2.8 and 2.9. Here, as the resonances have Fano shapes, each pair of patterns corresponds to the frequencies of the maximum (a) and the minimum (b) reflectance. Therefore, on panels (a) one can see the standing wave created by the interference of the incident plane wave and the strongly reflected wave (i.e. the 0-th Floquet harmonic) in the upper half-space and deep shadow in the lower half-space. The slab is depicted using white dashes.

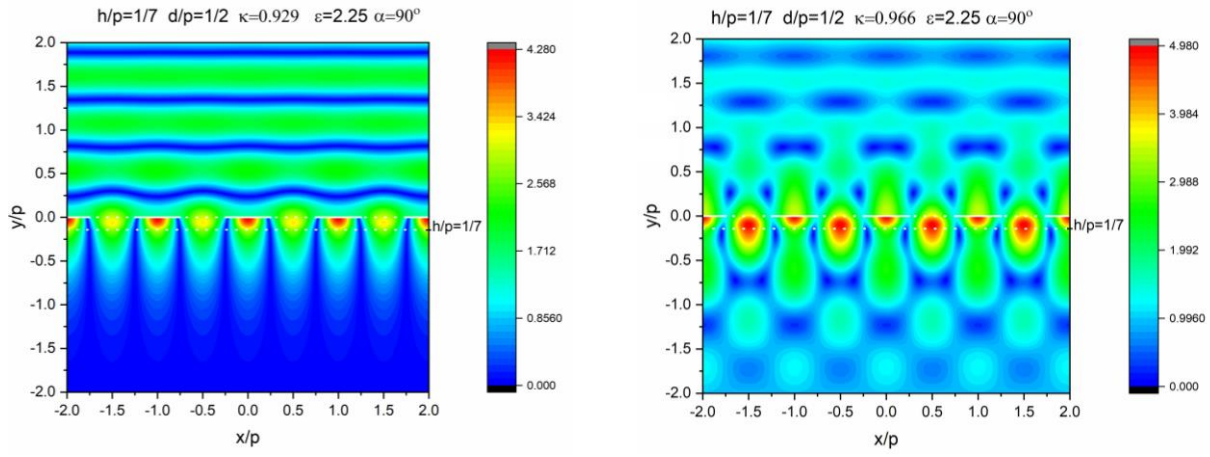

(a) (b)

Figure 2.8. Near magnetic field patterns on three periods of the PEC strip grating on top of dielectric slab with $\varepsilon = 2.25$, in the maximum $\kappa = 0.929$ (a) and in the minimum $\kappa = 0.966$ (b) of reflectance, corresponding to the Fano-shape resonance on the L_1 mode, see Fig.2.7 (b).

In the domain of slab, the LM contribution clearly dominates on both panels. In Fig. 2.8, there are two bright spots of the field on a period, while in Fig. 2.9 there are six spots. This indicates that the resonating modes are L_{10} and L_{30}, respectively.

The standing-wave pattern, characteristic for the LM, is created by the equal-amplitude +1-st and -1-st Floquet harmonics, and +3-rd and -3-rd, respectively. This happens because the mentioned harmonics dominate over all others, in the resonances.

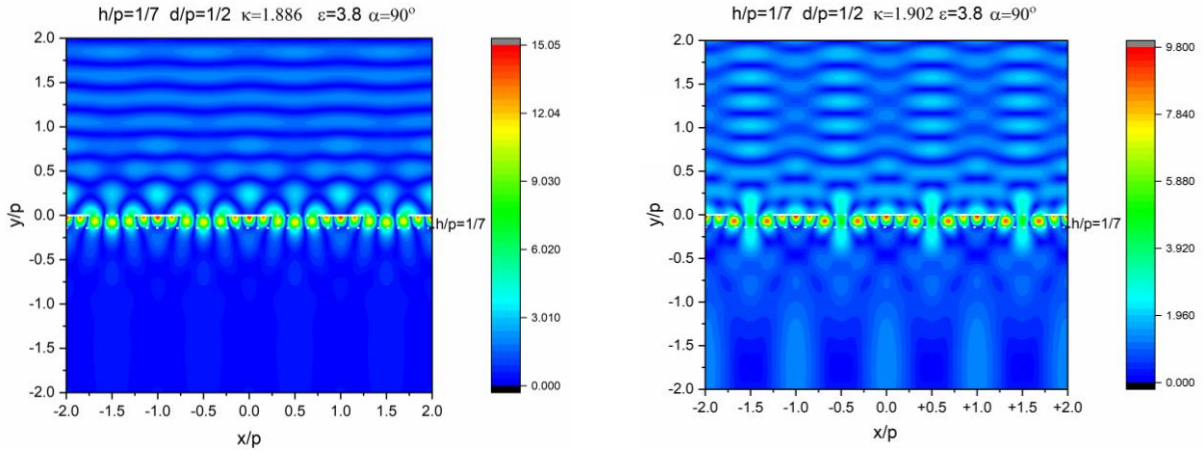

(a) (b)

Figure 2.9. The same as Fig. 2.8 however for $\varepsilon = 3.8$ and the resonance on the L_3 mode in the maximum $\kappa = 1.886$ (a) and in the minimum $\kappa = 1.902$ (b) of the reflectance, see Fig.2.7 (c).

It should be emphasized that the lattice or grating modes are attracting great attention today. This is because they are responsible for a number of amazing and sometimes counter-intuitive phenomena, such as "anomalous" transmission and, reciprocally, reflection, and enhanced absorption in the case of lossy gratings, plus giant Kerr, Kerker, and Faradey effects [65-68]. The existence of the LMs is caused by the periodicity. Their optical properties, for the strip and wire gratings in the visible-light wavelength range were recently reviewed in [62]; another review, with emphasis on experimental measurements, can be found in [63].

As already mentioned, the LMs, i.e. the poles of the field U as a function of the normalized frequency, κ, and associated with them resonances are absent in the case of zero-thickness PEC-strip grating in the free space, i.e. without finite-thickness dielectric substrate [34]. This is apparently the reason that the corresponding effects are sometimes called "guided-mode resonances." Still, as soon as the strips are assumed not

PEC, the resonances on the LMs emerge near to the RA as the dominant features in the scattering and absorption [24,58-60]. The same happens if the strips have however small but finite thickness.

Here, the existence of the natural guided waves of the dielectric substrate or non-PEC plane plays the role of mediator. They shift the LM poles further to the red from the RA values according to the wavelength of the natural wave, which is always shorter than the free-space wavelength.

Finally, we present the results related to the inclined incidence of the plane H-polarized wave on the PEC strip grating on top of a dielectric substrate layer, see Fig. 2.10.

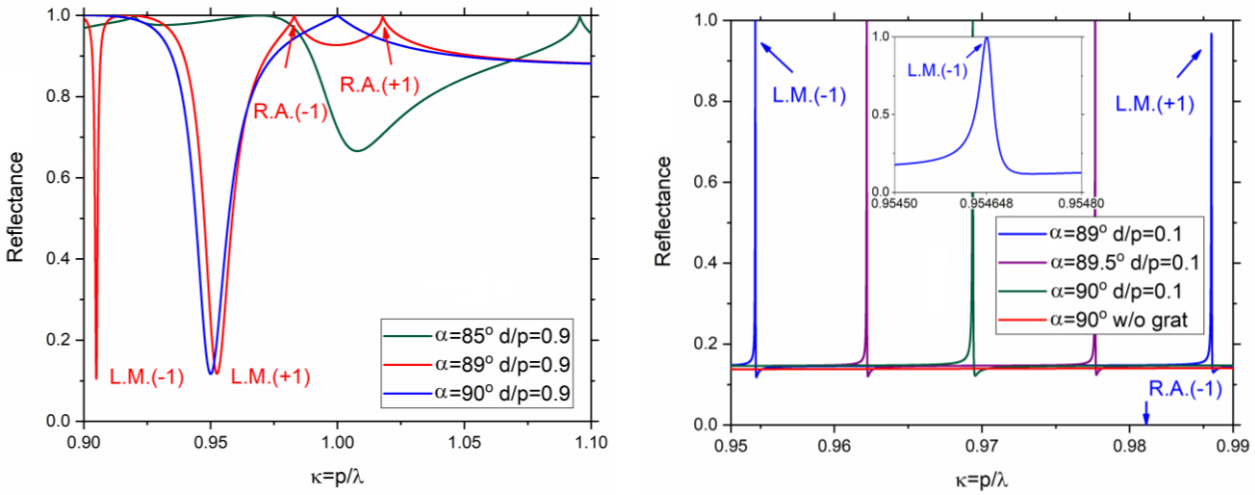

Figure 2.10. The reflectance of the on-substrate grating versus the normalized frequency for $h/p = 1/7$ and $\varepsilon = 2.25$ in the case of the normal and inclined incidence, the values of the incidence angle α and the filling factor *d*/*p* are indicated in the insets.

In this case, each RA splits to two anomalies, +*m*-th and –*m*-th, according to two separate roots of equations $\gamma_n = 0$, $n = \pm 1, \pm 2, \ldots$ at $\cos\alpha \neq 0$. One of the RA, for positive *n*, obtains higher, in frequency, value, than at the normal incidence, and the other RA, for negative *n*, obtains lower value. Each of the split RA is accompanied with its own "satellite" in the form of the LMs resonance of the same index. They have

opposite symmetry with respect to the center of the strip and therefore only one of them, on the symmetric mode, is present at the normal incidence, while the other one, on the anti-symmetric sister mode, is absent. Field portraits of such modes can be seen in Chapter 4. In the other words, the anti-symmetric LM remains “dark” at the normal incidence, while symmetric one is “bright.” At inclined incidence, both LM are bright.

These effects are especially well observable if the strip width-to-period ratio is close to 1 (see panel (a)) or to zero (see panel (b)). The resonances reveal themselves as sharp and deep drops in reflection and even sharper peaks of reflection, respectively. This corresponds to what is frequently called anomalous transmission” and “anomalous reflection” phenomena, respectively.

2.3.2 E-polarization: resonances on substrate and lattice modes

First, just like in the case of H-polarization, we need to make sure that the solution to the problem converges. To analyze the rate of convergence of the code based on (2.40), we make some numerical experiments. Namely, we select two values of the normalized frequency $\kappa = p/\lambda$, 14.1 and 100.1, take both normal and inclined incidence, $\alpha = 90^{o}$ and 45^{o}, and assume that the strips and slots are equal in size.

As usual, the relative error is computed in the sense of l_2-norm, as the difference between two solutions found with a given truncation order N and with some large $N_{\max}$.

As the transmittance and reflectance are expressed via finite sums (2.10) and (2.13), the error in their computation is of the same order as (1.9). The results of computations are shown in Fig. 2.10 for $N_{\max} = 400$ and several values of the substrate thickness and dielectric constant. As visible, with an increase in the truncation order N the error at first oscillates, and then after some threshold value larger than κ, the error starts decreasing, i.e. the accuracy of the calculation increases. As one can see from Fig. 2.11, the exponential decay starts as soon as N becomes larger than $\kappa\sqrt{\varepsilon} + M$, де M where M depends on the substrate thickness and optical contrast.

As visible, the rate of convergence is similar both in the case of absence of dielectric layer and at its presence. Still, thicker and optically denser substrates entail larger values of N to achieve the same accuracy. In contrast, the fill factor, d / p, and the angle of incidence, α, have no effect on the rate of convergence.

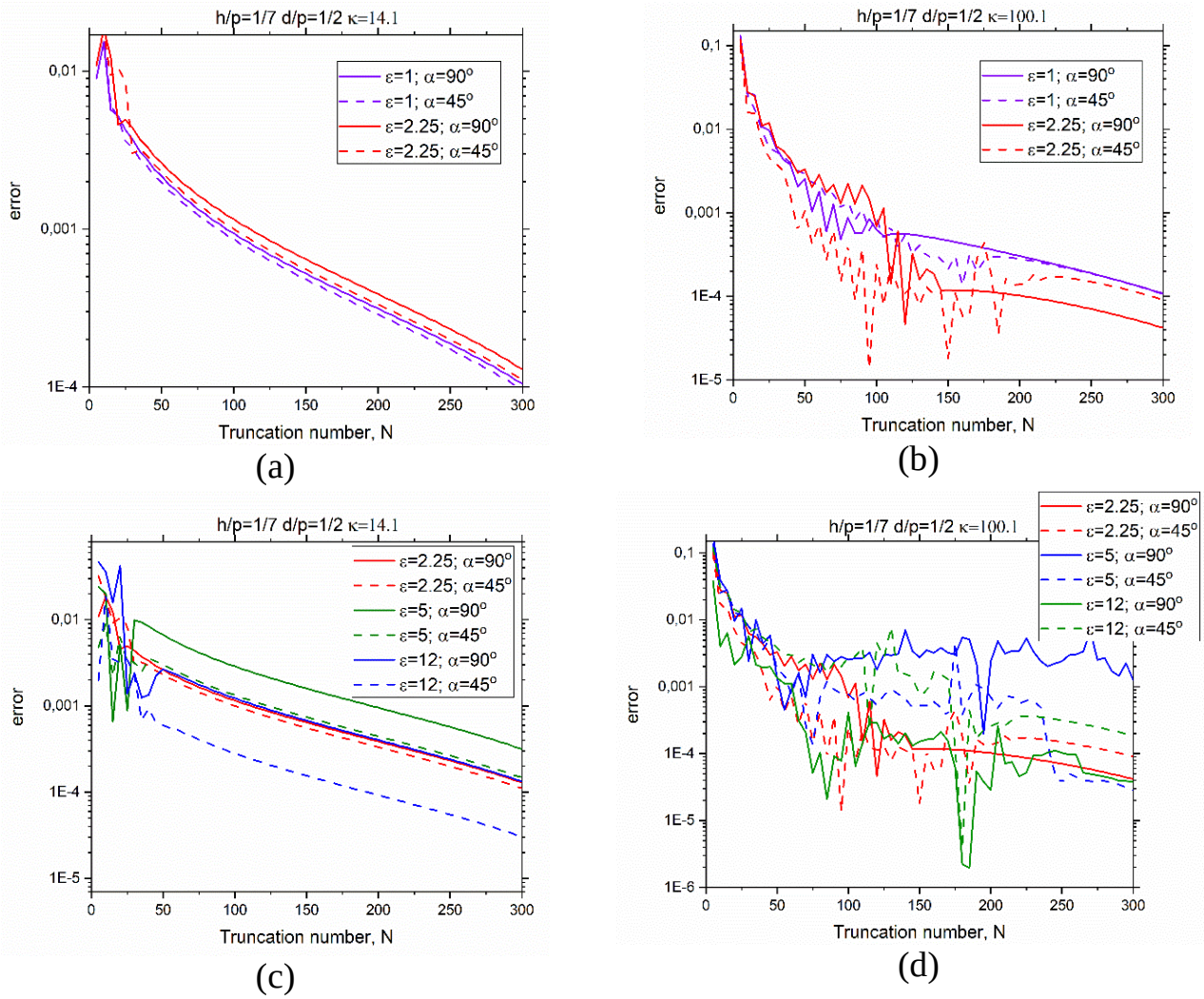

Figure 2.11. The error versus the order of truncation for the grating with strips d/p = 0.5, angles of incidence α = 90° and 45°, and h/p and ε as indicated in the inset, κ= 14.1 (a), (c) and κ = 100.1 (b), (d).

As for the power conservation law, we have found that it is satisfied with machine precision.

Further, for the validation of our code we present, in Fig. 2.12, a comparison of our results with those of [51], computed by another full-wave convergent technique, MAR-Galerkin with the Chebyshev first-kind polynomials as basis functions.

The plots correspond to the absolute value of the transmission coefficient as a function of the frequency for three cases: on-substrate strip grating, freestanding strip grating, and unloaded dielectric slab. Visual overlap of the curves is exactly what is expected if both methods are full-wave, convergent, and the orders of discretization are high enough. As the results of [51] were validated by the agreement with commercial software, this agreement holds for our results as well.

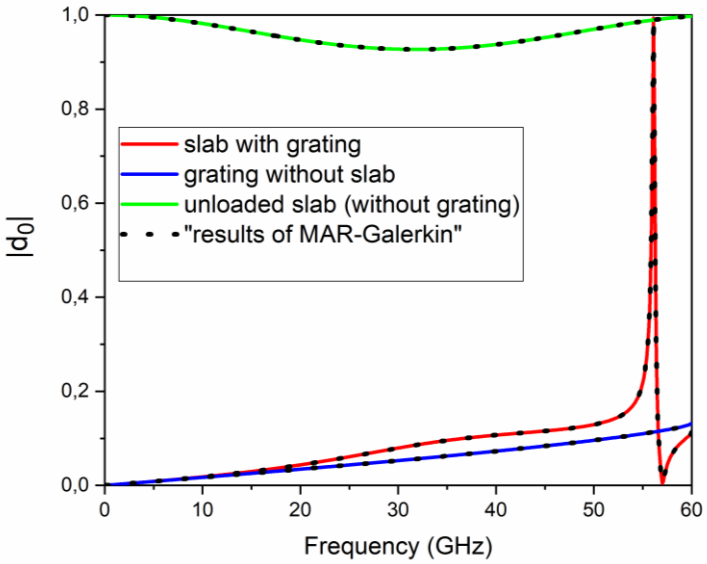

Figure 2.12. Comparison of the results of [51] and MAR-RHP using (2.42), for $p = 5$ mm, $d = 4$ mm, $h = 1.5$ mm, $\varepsilon = 2.2$. Absolute value of the amplitude transmission coefficient of strip grating on top of dielectric substrate versus the frequency in the single-harmonic range, $0 < \kappa < 1$. The plots for freestanding strip array and for bare dielectric slab are also shown.

Note a sharp total-transmission peak at 57 GHz for the wide-strip (d = 0.8p) grating on the thin (h = 0.3p) dielectric slab. This is the lattice-mode LM_{11} resonance, which has actually a Fano shape of double extremum. Off this resonance, the transmission is small and almost the same as for a PEC-strip grating without substrate.

Thus, the LM resonance can completely ruin the famous “Hertz effect” of strong reflection of the E-polarized plane wave from a PEC strip grating.

In Fig. 2.13 (a) presented are the plots of the reflectance (2.12) versus the normalized frequency κ for the normal incidence of the E-polarized plane wave on a grating with narrow strips, in the free space and on a thin substrate with the relative permittivity values 2.8 and 3.8.

At $\kappa = 1,2,3$, all the curves make sharp bends: these points are the RA, where $p = \lambda, 2\lambda, 3\lambda$; they are the branch points of the scattered field $U(x, y, \kappa)$ as a function of the frequency. Besides, one can see double (Fano-shape) extrema: these are the resonances on the LM^{+}_{m0} of the orders m = 1,2,3. Panels (b) and (c) show zooms of the spectra in the vicinities of RA. They demonstrate that, if the optical contrast or thickness of substrate gets smaller, then the LM peaks of total reflection move closer to the RA frequencies and their Q-factors get larger. The shift, to the red side, from the RA is mediated by the guided wave of the dielectric slab. At the normal incidence, where a phase shift between the adjacent periods is absent, the resonance frequencies are found to be [61],

$$\kappa^{L}_{mM} \approx \kappa^{RA}_{m} \left(\varepsilon^{eff}_{M} \right)^{-1/2}, \tag{2.43}$$

where $\kappa^{RA}_{m} = m$ and $1 < \varepsilon^{eff}_{M} < \varepsilon$ is the “effective dielectric permittivity” of the slab, defined as square of the normalized by k_0 propagation constant of the M-th guided wave of the slab, TE_M. This value is a function of the frequency and slab’s parameters, h and ε. Therefore, if the substrate parameters are as in Fig. 2.13, the resonance on the LM_{10} mode takes place below RA_1, however, there are two Fano-shape resonances, on LM_{20} and LM_{30}, between RA_1 and RA_2.

Here, it should be reminded that the principal wave TE_0 has no cutoff frequency, and higher-order waves TE_M start propagating at the frequencies, satisfying the condition, $k_0 h(\varepsilon - 1)^{1/2} = M\pi$ [104]. Note that for all guided waves including the

principal wave, $\varepsilon_M^{eff} = 1 + (\varepsilon - 1)O(k_0 h)^2$ if $k_0 h \to M\pi(\varepsilon - 1)^{-1/2} + 0$. Therefore, if either $\varepsilon \to 1$ or $h \to 0$, then all the complex poles of $U(x, y, \kappa)$, which correspond to LMs, tend to the RA values, which are the branching points, and then migrate to the bottom (non-physical) sheet of the square-root Riemann surface. Such singularities do not show up as peaks or drops, in the spectral dependences.

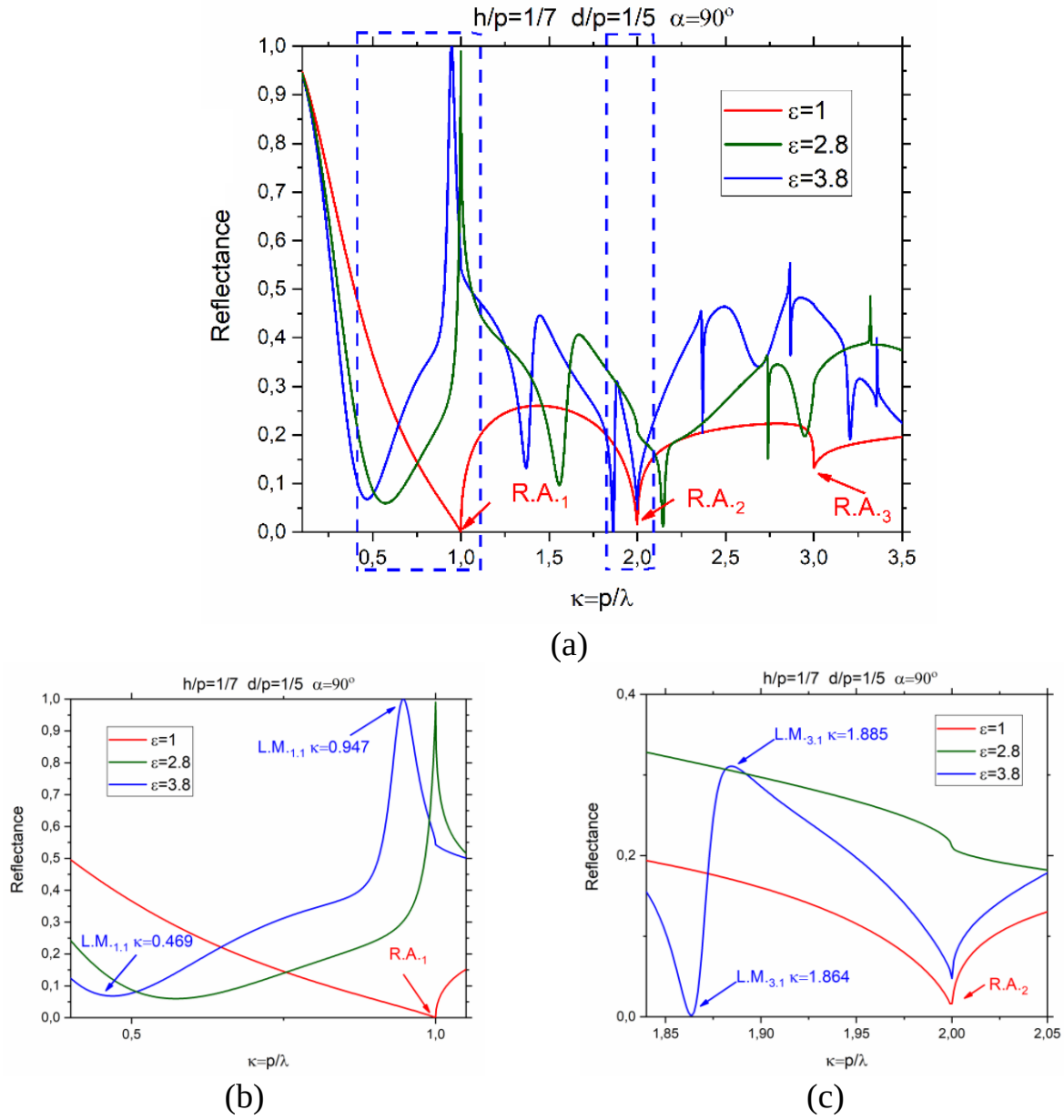

Figure 2.13. The reflectance of the free-standing and on-substrate gratings with $h/p = 1/7$, $d/p = 0.2$ versus the normalized frequency for three values of the permittivity $\varepsilon = 1$, $\varepsilon = 2.8$ and 3.8 (a), zooms near RAs, $\kappa = 1$ (b) and $\kappa = 2$ (c).

In Fig. 2.14 to 2.16, we present the portraits of the near electric field, $|E_z|$, in three resonances LM_{n1} (n = 1,2,3) marked in Fig. 2.13 (b), (c) by arrows. Inside the substrate, one can see the LM signatures: bright hot spots, the number of which, on period, corresponds to the first lattice-mode index [62].

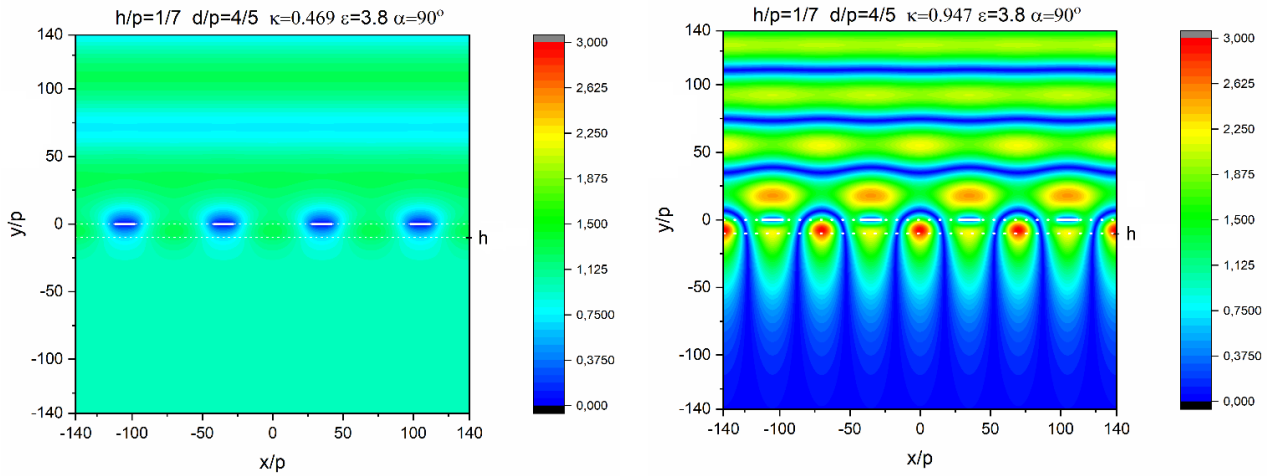

Figure 2.14. The electric field patterns on four periods in the reflectance minimum, $\kappa = 0.469$ (a) and maximum, $\kappa = 0.947$ (b) of the LM_{10} resonance at the normal incidence on the same grating as in Fig. 2.13.

The lattice (a.k.a. grating) modes and associated resonance effects are currently under intensive investigation. This is explained by the observation that they are found behind a number of remarkable and to some extent counter-intuitive phenomena, for instance, “anomalously” high transmission through and, reciprocally, high reflection from the arrays of extremely narrow holes and small particles, respectively. This relates also to the resonances in absorption in lossy gratings, and to “giant” Kerr, Kerker, and Faraday effects [65-68].

The LMs are natural modes of every grating as a periodic open resonator. Pioneering research where such resonances were discovered theoretically in the scattering from a periodically modulated impedance plane, was published in 1965 [31]. However, these authors failed to recognize that the resonances were caused by the

presence of certain eigenmodes as solutions to the source-free equations, neither they studied the scattering from the other gratings, gradually, this discovery was forgotten.

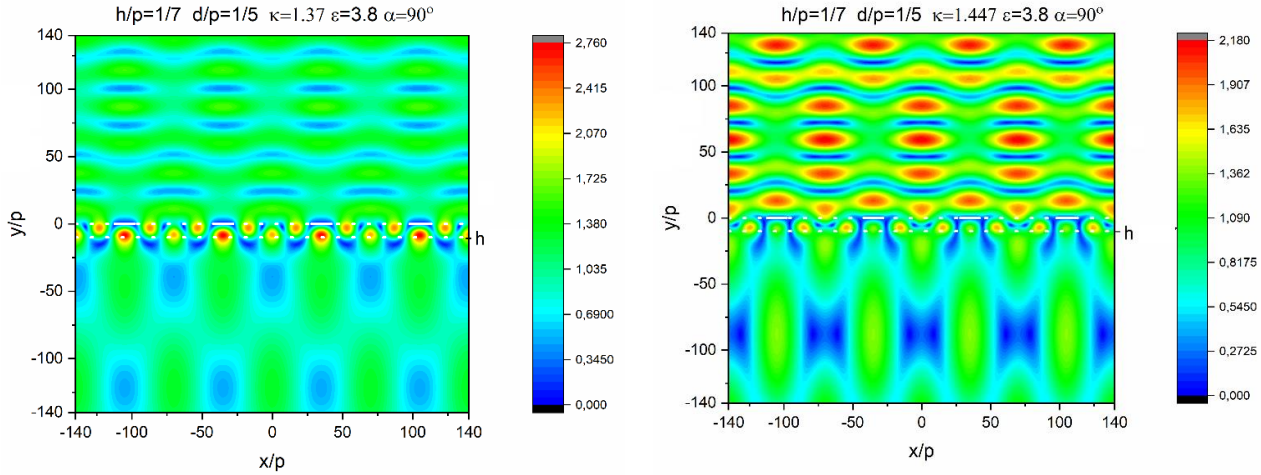

Figure 2.15. The electric field patterns on four periods in the reflectance minimum, $\kappa = 1.37$ (a) and maximum, $\kappa = 1.447$ (b) of the $LM^{+}_{2,1}$ resonance at the normal incidence on the same grating as in Fig. 2.13.

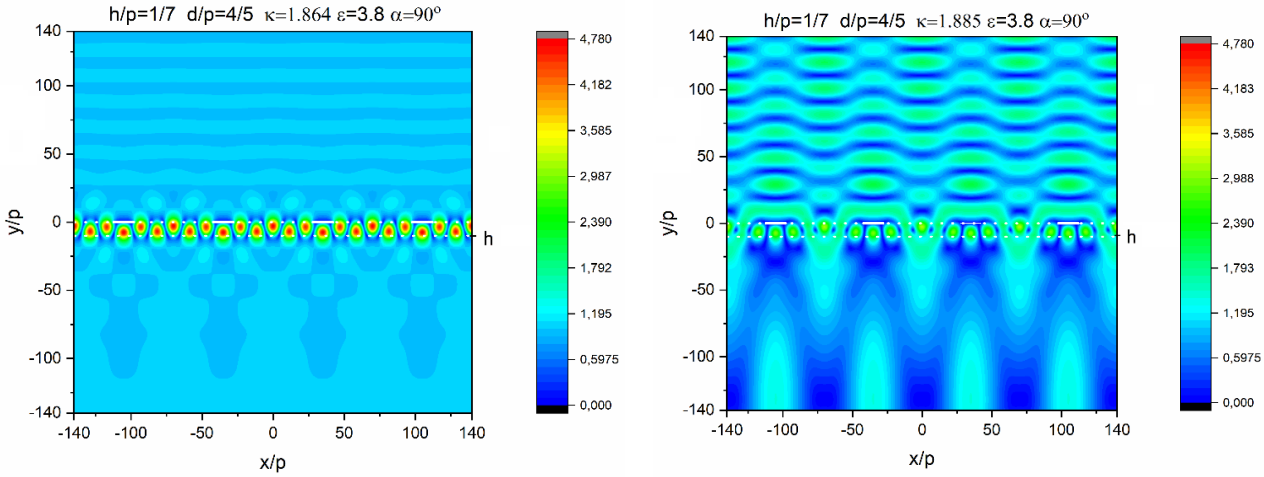

Figure 2.16 The electric field patterns on four periods in the reflectance minimum, $\kappa = 1.864$ (a) and maximum, $\kappa = 1.885$ (b) of the $LM^{+}_{3,1}$ resonance at the normal incidence on the same grating as in Fig. 2.13.

In 1986, K. Carron and his co-workers published a study into the scattering of light by large two-periodic arrays of silver nanoparticles on a substrate, combining theory and measurements and showing narrow resonances near the RA wavelengths [105].

However, then this effect did not attract any reasonable attention of research community. Ten years later, extremely high-Q complex poles near to the RAs were computed in the analysis of the 2-periodic gratings made of 3-D dielectric “bricks” [106]. Nevertheless, these findings had not been properly understood and explained.

As explained in review [62], this situation started changing in the early 2000s. Today, there is a well-established understanding that the lattice (a.k.a. grating) modes are specific eigenmodes of nearly all types of gratings as periodic open resonators. For the gratings of material strips and wires in the visible-light range of wavelengths, their properties were summarized in [62]; fine measurements of the characteristics of these resonances in the visible-light range were published in [63].

In view of recent findings and better understanding of the nature of LMs, it becomes clear that they are directly responsible for the famous “large phased-array blindness effect” discovered experimentally over 50 years ago [107,108] and still puzzling the antenna engineers [109]; sometimes this effect hides behind “anomalously high” Q-factors of antenna arrays [110].

Traditionally, this phenomenon is explained via empiric considerations of the “synchronism” between the substrate guided mode and a Floquet harmonic of the scattered field. As one can see, this is formally expressed as equation (2.43). New knowledge allows to see that the true reason of “blindness” is that the frequency, during the scan, hits a tremendously high-Q natural mode of the array that, indeed, lays near to the point of that “synchronism”.

Worth noting is that LMs and associated with them resonances do not exist on a zero-thickness PEC-strip grating, suspended in the free space (see Fig. 2.13). In [50,51], this is explained by the absence of capacitance (inductance) in the equivalent circuit in the case of the E (H) polarization. From the full-wave viewpoint the same can be attributed to the fact that the LM pole is located on the bottom sheet of the associated two-sheet Riemann surface that has the branching point at RA. The need of substrate to shift that pole to the top sheet (see Chapter 3) is a reason to justify the fact that the resonances on LMs are also called “guided-mode resonances” [111].

As already mentioned, if the substrate thickness or its contrast with environment tends to zero, then the LM poles tend to the corresponding RA frequencies [62]. As the latter if purely real-valued, the LM Q-factors grow up indefinitely. On finite periodic arrays, these Q-factors reach finite high vales, defined by the number of elements. This makes such resonances dangerous and unwanted phenomena in phased array antennas however very attractive in the design of optical biological and chemical sensors.

To make our study more complete, we present in Fig. 2.17 the spectra of the reflectance of on-substrate PEC-strip gratings with three different filling factors, *d*/*p*, under the normal incidence.

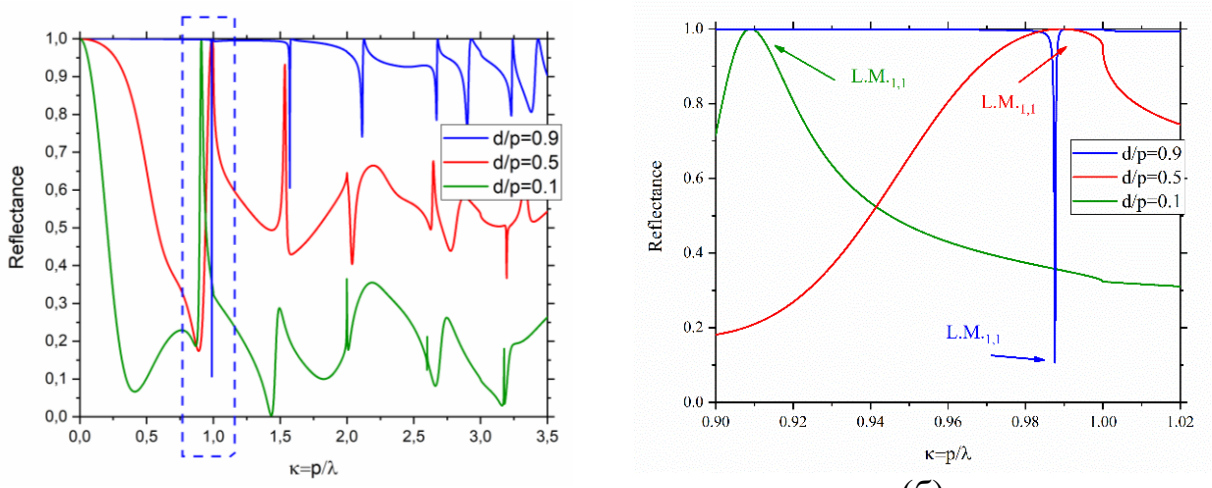

(a) (б)

Figure 2.17. The reflectance of the on-substrate grating versus the normalized frequency for $h/p=0.2$, $\varepsilon=2.8$ (Teflon, Polyethylene), and three values of the filling factor, i.e. the strip-to-period ratio (a), and the zoom in the marked interval near $\kappa=1$ (b).

As expected, a grating of wide PEC strips shows almost total reflectance at all wavelengths exceeding the grating period, except a narrow drop very close to the first RA. This is the resonance on the first-order LM. A zoom of spectra in the vicinity of the first RA, shown on panel (b), helps seeing this effect of “anomalous transmission” in detail. The opposite case of a grating of narrow PEC strips shows good reflection only for the waves, much longer than the grating period. Even if the wave is twice longer than the period, reflectance drops to 0.1 and less. However, near the first RA frequency,

the reflectance shows a resonance spike of almost total reflection again, now due to the first-order LM resonance. This is sometimes called “anomalous reflection” phenomenon.

Finally, the plots in Fig. 2.18 correspond to the inclined incidence of the E-polarized plane wave on the on-substrate gratings with three different values of the filling factor, d/p = 0.1, 0.5 and 0.9. The incidence angle values, 85° and 89°, are near to the normal-incidence value of $\alpha = 90^{o}$.

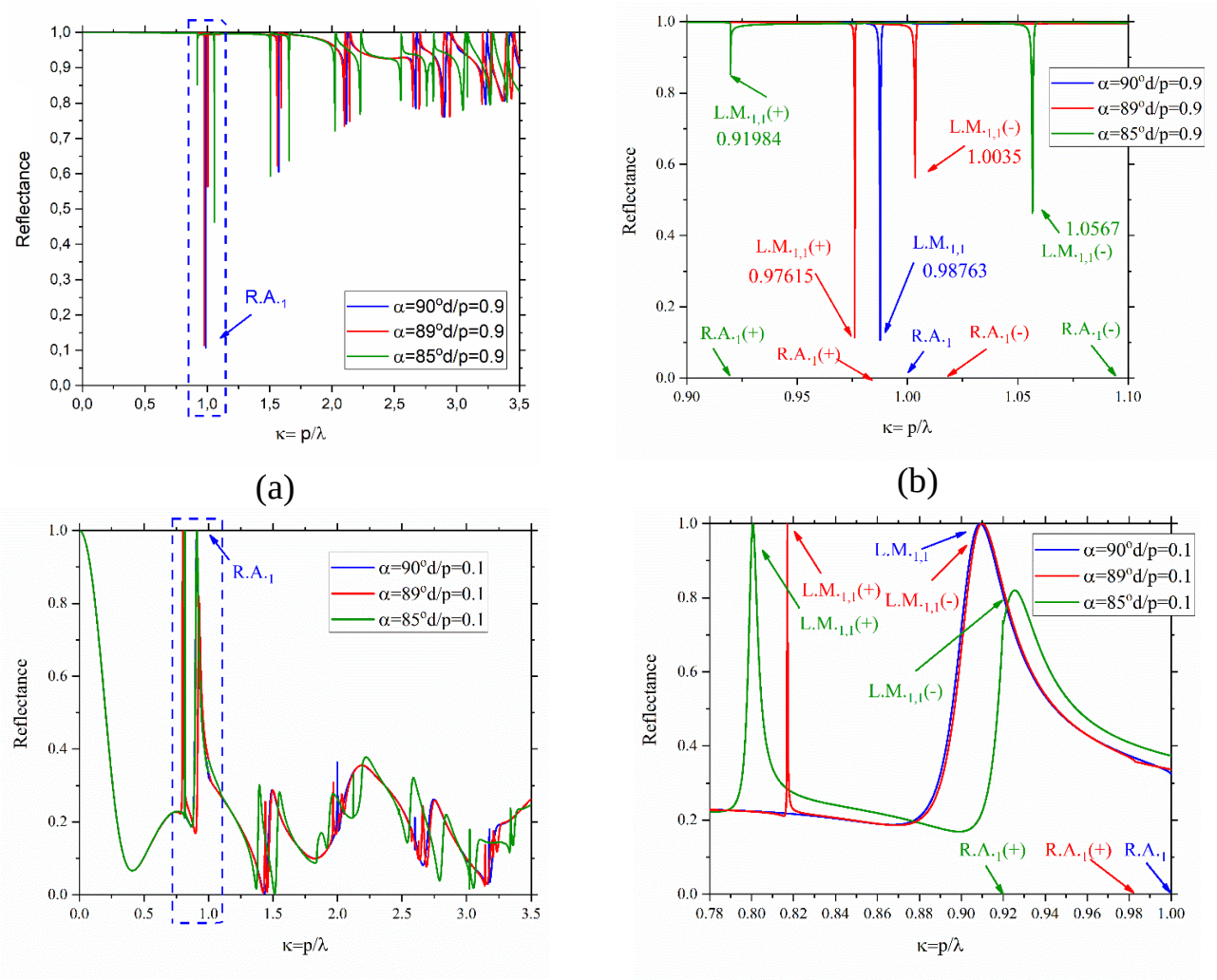

Figure 2.18. The reflectance of the on-substrate grating with wide strips (a), (b) and narrow strips (c), (d) versus the normalized frequency for $h/p = 0.2$ and $\varepsilon = 2.8$ in the case of the normal and inclined incidence, the values of the incidence angle α and the filling factor d/p are indicated in the insets. Note that panels (b) and (d) are zooms of the parts of (a) and (c), respectively.

These plots demonstrate that, at the inclined incidence, the resonances on LMs split into pairs together with RAs. As known, one of RAs shifts to the “blue” and the other – to the “red.” Each $LM^{\pm}_{m0}$ resonance accompanies the corresponding RA of the $\pm m$-th order from the red side of the spectrum.

Conclusions to Chapter 2

We have implemented a numerical algorithm for solving the problem of the scattering a plane H and E-polarized electromagnetic waves from an infinite grating of PEC strips on the surface of a dielectric substrate. This algorithm is meshless and based on full-wave formulation of the corresponding boundary value problem. It exploits the analytical inversion of the static part of the problem associated with the grating in free space by means of the well-known RHP solution and the derivation of the Fredholm matrix equation of the second kind. Note that we have presented the final matrix equations in the form, most convenient for programing and computations.

The behavior of the computation at error versus the order of truncation of this matrix equation confirms the convergence of the algorithm and its high efficiency.

Computations of the frequency dependences of the reflectance of the grating on the substrate confirmed the existence of high Q resonances on the LMs, which do not exist on the grating of PEC strips in free space. These results help explain the effect of "phased array blindness", which was discovered more than 50 years ago, and the phenomenon of "abnormally high Q" matrix, which has been recently reported. The importance of LM resonances for applications is twofold. First, this effect may be undesirable due to the deterioration of electromagnetic systems based on arrays of identical elements, such as large phased array antennas. In this case, our analysis helps avoid such deterioration. However, second, the behavior of the scattering resonances on ultra-high Q LMs suggests that they can be useful as a physical basis in various sensing

applications; for example, they can be used to design sensors of refractive index changes in the substrate.

The portraits of the resonance near fields clearly show the standing waves of high amplitudes which are characteristic of LMs, previously found for other infinite and finite gratings.

The results related to Chapter 2 were published as journal papers [A4, A5] and conference papers [A13 - A16].

CHAPTER 3
SCATTERING AND ABSORPTION OF PLANE WAVES BY GRAPHENE STRIP GRATING ON DIELECTRIC SUBSTRATE

This chapter presents the analysis of the scattering and absorption of the H and E-polarized plane waves by infinite grating of flat graphene strips on the surface of a dielectric substrate. The difference from the PEC-strip grating of Chapter 2 is in the imperfect conductivity of strips, characterized with the aid of the complex-valued surface impedance (or resistivity), Z. Fortunately, this surface impedance has analytical description, given by the Kubo formalism – see Chapter 1. Then, the one-side PEC boundary conditions on the strips change to the two-side resistive boundary conditions. Still, the role played by the impedance is different in the H- and E-polarization cases.

In the H-case, finite impedance is non-singular perturbation to the PEC condition. In contrast, it is a singular perturbation in the E-case. Moreover, in the E-case non-zero impedance plays the role of regularizing parameter. As a consequence, our full-wave meshless codes are now very different. For the H-polarization, the code is still based on the analytical semi-inversion using the RHP solution and allows $Z = 0$. For the E polarization, it is based on the use of Inverse Discrete Fourier Transform, and $Z \neq 0$.

In either case, we reduce the scattering problem to a Fredholm second-kind matrix equation for the Floquet harmonic amplitudes that guarantees the code convergence. The convergence provides easy control of computational error, which can be reduced to machine precision. The matrix elements are combinations of elementary functions and therefore each code is not only accurate but very economic. This enables us computing the reflectance, transmittance and absorbance as a function of the frequency, in the wide band from static case to dozens of THz. Numerical results show that such a metasurface with micrometer-sized strips is a composite periodic open resonator. It is highly frequency-selective, thanks to the interplay of three types of natural modes: low-Q slab modes, moderate-Q plasmon strip modes, and ultrahigh-Q lattice modes, which do not exist in the absence of the substrate. Varying the chemical potential of graphene, one

can manipulate the electromagnetic characteristics of metasurface at a fixed frequency from almost total transmission to almost total reflection.

The results of Chapter 3 were published in [A1-A3, A8-A11].

3.1 Scattering problem formulation

The scattering configuration is shown in Fig. 3.1. The scattering problem statement is the same as for a PEC-strip grating on substrate, considered in Chapter 2, the only difference is in different boundary conditions at the zero-thickness strips.

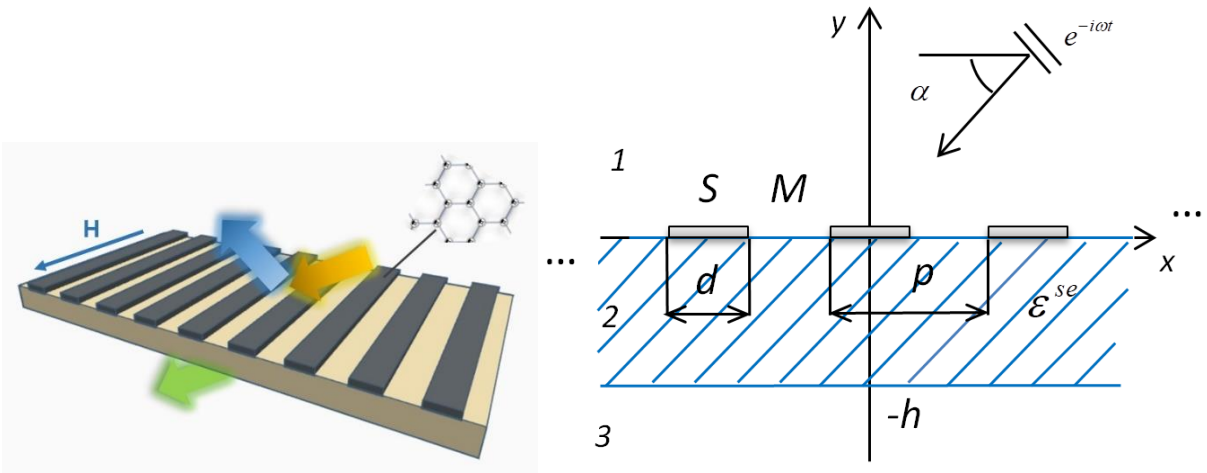

(a) (b)

Figure 3.1 Infinite flat graphene strip grating laying on a dielectric substrate and illuminated by a plane H or E-polarized wave (a) and cross-sectional geometry and notations used (b).

As in the previous section, in the case of the H-polarization the field components are $(E_x, E_y, 0)$ and $(0, 0, H_z)$ and the "basic" component is H_z; in the case of the E-polarization, the field components are $(H_x, H_y, 0)$ and $(0, 0, E_z)$, and the "basic" one is E_z; in either case, the basic component is denoted as $U(\mathrm{x}, \mathrm{y})$. The incident plane wave is (2.1) and the total field is as in section 2.1. Then, for the unknown scattered field $U(\mathrm{x}, \mathrm{y})$, the following boundary-value problem is formulated: it must satisfy

(I) the 2-D Helmholtz equation everywhere outside the strips and the slab interfaces (2.2), with wavenumber *k* in domains 1,3 and $k\sqrt{\varepsilon}$ in domain 3;.

(II) resistive boundary conditions at the graphene strips lying on the upper interface, i.e. at $\vec{r} \in M : \{y = 0; |\, x + np \,| < d/2; n = 0, \pm 1, \pm 2, ...\}$, namely,

- in the case of the H-polarization

$$\frac{1}{ik_0}\frac{\partial}{\partial y}\left[\frac{1}{\varepsilon}U^{(2)}(x,y) + U^{in}(x,y) + U^{(1)}(x,y)\right]\Bigg|_{y=0} = 2Z\left[U^{(2)}(x,0) - U^{(in)}(x,0) - U^{(1)}(x,0)\right] \tag{3.1-a}$$

$$\frac{\partial}{\partial y}\left[\frac{1}{\varepsilon}U^{(2)}(x,y) + U^{in}(x,y) + U^{(1)}(x,y)\right]\Bigg|_{y=0} = 0, \tag{3.1-b}$$

- in the case of the E-polarization,

$$U^{(1)}(x,0) + U^{in}(x,0) = U^{(2)}(x,0) \tag{3.2-a}$$

$$\left[U^{(2)}(x,0) + U^{(in)}(x,0) + U^{(1)}(x,0)\right] = -2Z\frac{1}{ik_0}\frac{\partial}{\partial y}\left[U^{(2)}(x,y) - U^{(in)}(x,y) - U^{(1)}(x,y)\right]\Bigg|_{y=0} \tag{3.2-b}$$

transparent boundary conditions at the slots between the strips, i.e. at $\vec{r} \in S : \{y = 0; -\infty < x < +\infty\} \setminus M$ for the either polarization, and similar conditions at the whole lower interface, $y = -h$, $-\infty < x < +\infty$, (2.5a) and (2.5b);

(III) the radiation condition: the scattered field in domains 1,3 must contain only the outgoing and decaying waves; (IV) the condition of local finiteness of power.

Conditions (I)–(IV) provide the solution uniqueness: if the function U exists, then it is unique. Note that if $Z = 0$, then (3.1) turn into the PEC conditions however (3.2) - not.

3.2. H-case: regularization by the Riemann-Hilbert problem method

The property of quasi-periodicity as in case PCE strips (2.3) allows expanding the unknown field in terms of the Floquet series in each of domains #1 in the upper half-space (2.8), #2 in the dielectric substrate (2.9), and #3 in the lower half-space (2.10).

The reflectance and transmittance are the power fractions taken from the slab with grating to the upper and lower half-space, respectively. They are expressed via the Floquet harmonic amplitudes as (2.12).

Substituting (2.8)-(2.9) into the conditions (2.5-a), we obtain

$$\begin{cases} \sum\limits_{n=-\infty}^{\infty}\left(b_n e^{-i\gamma_n^{sl}\xi}+c_n e^{i\gamma_n^{sl}\xi}\right)e^{i\beta_n\phi}=\sum\limits_{n=-\infty}^{\infty}d_n e^{i\gamma_n\xi}e^{i\beta_n\phi} \\ \frac{1}{\varepsilon}\sum\limits_{n=-\infty}^{\infty}\left(i\gamma_n^{sl}b_n e^{-i\gamma_n^{sl}\xi}-i\gamma_n^{sl}c_n e^{i\gamma_n^{sl}\xi}\right)e^{i\beta_n\phi}=\sum\limits_{n=-\infty}^{\infty}-i\gamma_n d_n e^{i\gamma_n\xi}e^{i\beta_n\phi} \end{cases} \tag{3.3}$$

Since these series coincide on the entire period, we replace them with term-wise equations and exclude the unknowns b_n and c_n, expressing them via d_n,

$$b_n=\tfrac{1}{2}d_n e^{i\gamma_n\xi}\left(1-\frac{\varepsilon}{\gamma_n^{sl}}\gamma_n\right)e^{i\gamma_n^{sl}\xi},\ c_n=\tfrac{1}{2}d_n e^{i\gamma_n\xi}\left(1+\frac{\varepsilon}{\gamma_n^{sl}}\gamma_n\right)e^{-i\gamma_n^{sl}\xi} \tag{3.4}$$

According to the graphene conditions (3.1-a) and (3.1-b) on the strips, for $|\phi|<\theta$,

$$\frac{1}{\kappa}\left(-\kappa\sin\alpha e^{i\beta_0\phi}+\sum_{n=-\infty}^{\infty}a_n\gamma_n e^{i\beta_n\phi}+\frac{1}{\varepsilon}\sum_{n=-\infty}^{\infty}\left(\gamma_n^{sl}b_n-\gamma_n^{sl}c_n\right)e^{i\beta_n\phi}\right)= \\ 2Z\left(\sum_{n=-\infty}^{\infty}\left(b_n+c_n\right)e^{i\beta_n\phi}-e^{i\beta_0\phi}-\sum_{n=-\infty}^{\infty}a_n e^{i\beta_n\phi}\right) \tag{3.5}$$

$$-\kappa\sin\alpha e^{i\beta_0\phi}+\sum_{n=-\infty}^{\infty}a_n\gamma_n e^{i\beta_n\phi}=\frac{1}{\varepsilon}\sum_{n=-\infty}^{\infty}\left(\gamma_n^{sl}b_n-\gamma_n^{sl}c_n\right)e^{i\beta_n\phi} \tag{3.6}$$

On the slots, $\vec{r}\in S$, the conditions (2.4a) yield, for $\theta<|\phi|<\pi$,

$$e^{i\beta_0\phi}+\sum_{n=-\infty}^{\infty}a_n e^{i\beta_n\phi}=\sum_{n=-\infty}^{\infty}\left(b_n+c_n\right)e^{i\beta_n\phi} \tag{3.7}$$

$$-\kappa\sin\alpha e^{i\beta_0\phi}+\sum_{n=-\infty}^{\infty}a_n\gamma_n e^{i\beta_n\phi}=\frac{1}{\varepsilon}\sum_{n=-\infty}^{\infty}\left(\gamma_n^{sl}b_n-\gamma_n^{sl}c_n\right)e^{i\beta_n\phi} \tag{3.8}$$

Thanks to (2.4-a) and (3.1-b), equation (3.6) is satisfied on the entire period. Therefore, on substituting b_n and c_n from (3.4) and introducing new coefficients (n = 0,±1,…),

$$x_n = \left(-\delta_{n,0}\kappa\sin\alpha + \gamma_n a_n\right)\left(\Gamma_n\right)^{-1} + 2\delta_{n,0}, \tag{3.9}$$

$$\Gamma_n^H = \left[\frac{1}{\gamma_n} - \frac{\varepsilon}{\gamma_n^{sl}}\frac{\left(\gamma_n^{sl} - \gamma_n\varepsilon\right)e^{2i\gamma_n^{sl}\xi} + \left(\gamma_n^{sl} + \gamma_n\varepsilon\right)}{\left(\gamma_n^{sl} - \gamma_n\varepsilon\right)e^{2i\gamma_n^{sl}\xi} - \left(\gamma_n^{sl} + \gamma_n\varepsilon\right)}\right]^{-1}, \tag{3.10}$$

we arrive at the expression allowing to exclude d_n,

$$d_n = \left(x_n - 2\delta_{n,0}\right)\Gamma_n\varepsilon e^{i\gamma_n\xi}\left[i\gamma_n^{sl}\sin(\gamma_n^{sl}\xi) + \gamma_n\varepsilon\cos(\gamma_n^{sl}\xi)\right]^{-1} \tag{3.11}$$

Note that, if $|n|\to\infty$, then the weight function in (3.10) behaves as

$$\Gamma_n^H = \frac{i|n|}{1+\varepsilon}\left[1 + O\left(\frac{\kappa\cos\alpha}{|n|}\right) + O\left(\frac{\kappa^2}{n^2}\right) + O\left(e^{-|n|2\pi h/p}\right)\right] \tag{3.12}$$

To make analytical regularization, we introduce the function

$$\Delta_n^H(\kappa,\varepsilon,h/p,\alpha,Z) = |n| + i(1+\varepsilon)\Gamma_n^H + i(1+\varepsilon)\kappa Z \tag{3.13}$$

and, using the expressions (3.5)-(3.10), the following DSE for the unknown coefficients, x_n:

$$\begin{cases} \displaystyle\sum_{n=-\infty}^{\infty} x_n|n|e^{in\phi} = \sum_{n=-\infty}^{\infty} x_n\Delta_n^H e^{in\phi} - i(1+\varepsilon)2\Gamma_0, \quad \theta < |\phi| \le \pi, \\ \displaystyle\sum_{n=-\infty}^{\infty} x_n e^{in\phi} = 0, \quad |\phi| < \theta, \end{cases} \tag{3.14}$$

It can be verified that if all $\Delta_n = 0$, then (3.14) forms the RHP on an arc of the unit circle in the complex plane. This problem has analytical solution expressed via the Plemelij-Sokhotskii formulas, as explained, for instance, in [25,45]; note that when building this solution, the edge condition (IV) is used explicitly. If this procedure is applied to the full DSE (3.14), it yields an infinite matrix equation,

$$x_m = \sum_{n=-\infty}^{\infty} A_{mn}^H x_n + B_m^H, \quad m = 0,\pm1,\pm2,... \tag{3.15}$$

$$A_{mn}^H = \Delta_n^H T_{mn}(\theta), \quad B_m^H = -i(1+\varepsilon)2\Gamma_0 T_{m0}(\theta), \tag{3.16}$$

where all notations are the same as for the PEC-strip grating case, see section 2.2. Note that if $Z = 0$, then matrix equation (3.15) turns to the PEC equation (2.25).

As in the PEC-strip case, the large-index asymptotics of the Legendre polynomials enable one to see that the following infinite sums are bounded:

$$\sum_{m,n=-\infty}^{+\infty} \left| A_{mn} \right|^2 < \infty, \qquad \sum_{m=-\infty}^{+\infty} \left| B_m \right|^2 < \infty, \tag{3.17}$$

This is exactly what is needed to state that equation (3.15) is a Fredholm second kind matrix equation in the space of number sequences l_2. Hence, the convergence of its numerical solution for progressively larger truncation numbers N is mathematically guaranteed.

It should be noted that in [39] the inverted part of DSE was slightly different: namely, it involved the weight $|n|+const$ instead of $|n|$ in (3.14). This led to slightly faster convergence however led to appearance of the Legendre functions of complex-valued frequency-dependent index. Computation of these special functios is not a trivial task. In contrast, expressions (3.16) are combinations of elementary functions. Besides, they need no numerical integrations and hence can be easily computed with machine precision. This is an important advantage before the other MAR-like techniques, such as MAR-Galerkin in the spatial or Fourier-transform domains [38,47-52].

Inspection of (3.12), (3.13) and (3.16) shows that both Δ_n and A_{mn} contain the terms proportional to the normalized frequency, $\kappa = p / \lambda$, and the terms, proportional to $e^{-|n|2\pi h/p}$. This means that the regularization, i.e. semi-inversion of DSE, is performed via the analytical inversion of the static limit of the part, corresponding to the strip grating on the interface between two media, air and dielectric. As a result, both the existence of the finite thickness of substrate and the finite conductivity of strips must shift the "threshold" value of the matrix truncation number, after which the error starts descending, to the larger values than in the case of suspended PEC strips: $N_{th} \approx \kappa\left[1 + h\varepsilon^{1/2} / p + (1+\varepsilon)|Z|\right]$.

3.3 E-polarization: regularization using the inverse Fourier transform

Note that the Floquet series (2.8) - (2.10) already satisfy the boundary problem conditions (I) and (III). The boundary conditions, valid on the whole upper and lower interfaces, allow excluding a part of unknown coefficients. Then, the dual conditions (3.2-a) and (3.2-b) generate a DSE, with the domains of validity *M* and *S*. On introducing new unknowns, $A_n = \delta_{0n}(1 - 2\kappa \sin\alpha / \Gamma_0) + a_n$, and denoting

$$\Gamma_n^E = \gamma_n - \gamma_n^{sl} \frac{\left(\gamma_n^{sl} - \gamma_n\right) e^{i\gamma_n^{sl}\xi} - \left(\gamma_n^{sl} + \gamma_n\right) e^{-i\gamma_n^{sl}\xi}}{\left(\gamma_n^{sl} - \gamma_n\right) e^{i\gamma_n^{sl}\xi} + \left(\gamma_n^{sl} + \gamma_n\right) e^{-i\gamma_n^{sl}\xi}}, \tag{3.18}$$

we follow [20] and cast the DSE to the following form:

$$\sum_{n=-\infty}^{\infty} A_n \Gamma_n^E e^{i\beta_n\phi} = \begin{cases} 0, & \theta < |\phi| < \pi \\ -\dfrac{\kappa}{Z} \displaystyle\sum_{n=-\infty}^{\infty} A_n e^{i\beta_n\phi} - \dfrac{2\kappa^2 \sin\alpha}{Z\,\Gamma_0} e^{i\beta_0\phi}, & |\phi| < \theta \end{cases} \tag{3.19}$$

Note that this DSE is drastically different from the PEC-strip case of (2.39). therefore, the RHP-based regularization is not applicable here. However, as shown in Section 1.3, the left hand part of (3.19) can be inverted analytically using the IDFT, thus yielding a matrix equation for the unknowns A_n. Still, the rate of decay of the obtained by IDFT matrix elements with larger $|m|$ and $|n|$ is different, namely $O(m^{-2})$ and $O(|n|^{-1})$. To balance it, we follow [20] and introduce new variables as

$$x_n = A_n w_n, \quad w_n = \sqrt{|n| + 1}, \tag{3.20}$$

and finally arrive at the infinite matrix equation as follows:

$$x_m + \sum_{n=-\infty}^{\infty} A_{mn}^E x_n = B_m^E, \quad m = 0, \pm 1, \pm 2, \ldots \tag{3.21}$$

$$A_{mn}^E = \kappa w_m S_{mn} \left(Z\, w_n \Gamma_m^E\right)^{-1}, \quad B_m^E = -\sin\alpha\, 2\kappa^2 w_m S_{m0} \left(Z\, \Gamma_0^E \Gamma_m^E\right)^{-1}, \tag{3.22}$$

where

$$S_{nm} = \frac{\sin(n-m)\theta}{\pi(n-m)}, \quad S_{mm} = \frac{\theta}{\pi}, \quad m, n = 0, \pm 1, \pm 2, \ldots \tag{3.23}$$

As $\Gamma_n^E \cong i|n|\left[1+O(e^{-|n|2\pi h/p})+O(\kappa^2/|n|)\right]$ if $n>>1$, inspection of the large-index behavior of the matrix elements enables us to state that equation (3.21) is a Fredholm second kind matrix equation in the space of number sequences l_2. Hence, the convergence of its numerical solution to the exact solution with larger truncation numbers *N* is mathematically guaranteed by the Fredholm theorems. Then, the accuracy is easily controlled with the aid of the matrix truncation order.

3.4 Analytical study of the Rayleigh Anomalies and natural modes

Rayleigh Anomalies. RA are associated with the branch points of the field U as a function of the frequency and correspond to $\gamma_{\pm m}=\left[\kappa^2-(\pm m-\kappa\cos\alpha)^2\right]^{1/2}=0$ (m = 1,2,…); existence of these branch points is the consequence of our assumption that the grating is infinite and use of the Floquet series (3.13) and (3.14). Note that the frequencies, at which $\gamma_m^{sl}=0$, are not the branch points. Thus, RA frequencies do not depend on the fine structure of the grating period and are given by the following equations ($f=\omega/2\pi$):

$$f_{\pm m}^{RA}=\frac{cmp^{-1}}{1\mp\cos\alpha},\quad m=1,2,... \tag{3.23}$$

If the all periods are in the same phase, as at the normal incidence, the ±*m*-th RA frequencies coalesc and correspond to period divisible by the free-space wavelength,

$$f_{\pm m}^{RA}=cm/p,\quad m=1,2,... \tag{3.24}$$

Substrate modes. In the absence of strips, the dielectric-slab substrate is a simplest 1-D open resonator, sometimes called “Fabry-Perot etalon.” Its natural modes S_m have complex-valued frequencies, which are asymptotically given by the expressions, found, for instance, in [89],

$$f_m^S\approx c(m+1)/2h\sqrt{\varepsilon},\quad Q_m^S\approx\pi(m+1)\left(\ln\frac{\sqrt{\varepsilon}+1}{\sqrt{\varepsilon}-1}\right)^{-1},\quad m=0,1,... \tag{3.25}$$

The Q-factors of the slab modes are low, $Q_m^S \approx 10$. If the substrate is equipped with strips, the slab mode frequencies shift in the complex plane, however, they do not disappear.

Plasmon modes of the strip. As mentioned in Section 3.2, in the H-polarisation regime the grating of graphene strips demonstrate the resonances associated with the plasmon modes of each strip, P_m, $m = 1,2, \ldots$

Plasmon natural modes of a graphene strip can be conveniently viewed as the modes of the surface-wave Fabry-Perot resonator. Then the characteristic equation for such modes is

$$\sin\left(g_{plas} d + \psi\right) \approx 0, \tag{3.26}$$

where g_{plas} is the wavenumber (propagation constant) of the plasmon guided wave of infinite sheet of graphene located on the interface between dielectric and air and ψ is the phase of the reflection coefficient of that wave from the strip edge (here, we assume that the absolute value of the reflection coefficient equals 1). According to [112], if $|Z^2| >> 1$, then the wavenumber of the plasmon guided wave is

$$g_{plas}^2 \approx k^2(1+\varepsilon)\left[\tfrac{1}{2} - Z^2(1+\varepsilon)\right] + O(|Z|^{-2}), \tag{3.27}$$

and the best fit with the first-order plasmon mode is obtained if $\psi = \pi / 4$.

Suppose that graphene's impedance can be approximated with Drude term, (1.14) with (1.15) for Ω. Using this and (3.27) in (3.26) and neglecting the terms other than the leading one, we conclude that the natural frequencies of the plasmon modes P_m of graphene strip are given by

$$f_m^P \approx \frac{1}{2\pi}\left[\frac{c\Omega(\pi m - \psi)}{d(1+\varepsilon)}\right]^{1/2}, \quad m = 1,2,\ldots, \tag{3.28}$$

As visible from (3.28), these frequencies are inverse proportional to the square root of the strip width, *d*, and proportional to the square root of the mode index, *m*. They also scale as square root of the graphene chemical potential. Therefore, one can manipulate them by changing the DC bias. The Q-factors of the plasmon modes are between 10 and

100 and depend mainly on the relaxation time, τ. Neglecting the radiation losses and assuming that the frequency and chemical potential allow Drude approximation for the surface impedance (1.14), we derive

$$Q_m^P \approx \tau \left[\frac{(\pi m - \psi) c \Omega}{d(1+\varepsilon)} \right]^{1/2}, \quad m = 1,2,..., \tag{3.29}$$

Lattice modes of periodic open resonators. Besides of the dielectric-slab modes and graphene-strip modes, our metasurface possesses specific "collective" modes, which appear due to periodicity: these are the LM (also called "grating modes" [62,63]), $L^{\pm}{}_{mM}$. Here, index *m* correspond to the "parent" RA (3.30) because their complex frequencies tend to the latter if the slab thickness shrinks to zero. Still, at any finite thickness they are shifted, in the main term, by the frequency-dependent factor $g_M^H / k_0 > 1$,

$$f_{mM}^{\pm L} \approx \frac{cm(pg_M^H / k_0)^{-1}}{1 \mp \cos\alpha}, \quad m = 1,2,..., \quad M = 0,1,2,... \tag{3.29}$$

Here, g_M^H is the wavenumber of the *n*-th guided wave TM_M of the bare dielectric slab [63]. Note that, as the RA frequencies are purely real-valued, the LM Q-factors are controlled by the slab thickness mainly, so that if the slab vanishes, all $Q_{mM}^{\pm L}$ tend to infinity. However, it is known that the Poynting Theorem prohibits purely real-valued frequencies of natural modes of open resonators [88]. Indeed, in the limit, the complex poles of LMs fall into the RA branch points and further migrate to the bottom sheet of the correspoding Riemann surface.

Today, the LM resonances are found responsible for many remarkable phenomena, explained earlier by different mechaisms. Among them, besides of those mentioned in Chapter 2, there are "large phased-array scan blindness effect" [107-109], "anomalous antenna Q-factors" [110] and "guided-mode resonance" [111].

The casting of the E-case full-wave scattering problem to the Fredholm second-kind matrix equation (3.21) enables us to perform analytical study of LMs and

associated to them resonances in mathematically grounded manner, i.e. without resorting to the empiric quasi-static and circuit-theory considerations. This follows from the Gershgorin theorem of the matrix algebra [113], which states that the characteristic numbers of such a matrix equation are contained inside finite-radius circles on the complex plane, with their centers at the zeros of the diagonal elements. Here, it is necessary to introduce the coefficients $x_n^{\pm} = x_n \pm x_{-n}$ and split the matrix of (3.21) into two independent matrices, for the *x*-even and *x*-odd electric fields, that leads to replacement of $S_{m,n}$ with the coefficients $S_{m,n}^{\pm} = S_{m,n} \pm S_{-m,n}$, respectively. Then, assuming that $\alpha = 90^o$ and considering, for definiteness, the *x*-even natural modes, the approximate characteristic equations are

$$\Delta_m^{E\pm}(\kappa) = 1 + \frac{\kappa S_{m,m}^{\pm}}{Z(\kappa)\Gamma_m^E(\kappa)} + \frac{\kappa^2}{Z^2(\kappa)\Gamma_m^E(\kappa)} \sum_{n=0,\neq m}^{\infty} \frac{\left[\Gamma_n^E(\kappa)\right]^{-1} S_{m,n}^{\pm} S_{n,m}^{\pm}}{1 + \kappa Z^{-1}(\kappa)\left[\Gamma_n^E(\kappa)\right]^{-1} S_{n,n}^{\pm}} + O(Z^{-3}) = 0, \quad m = 1,2,... \tag{3.30}$$

At first, consider the case of *the graphene strip grating suspended in the free space*, $\varepsilon = 1$. Then, as follows from (3.18), $\Gamma_m^E = 2\gamma_m = 2\left(\kappa^2 - m^2\right)^{1/2}$, so that (3.30) reduces to

$$\gamma_m(\kappa) + \frac{\kappa S_{mm}^{\pm}}{2Z(\kappa)} + O\left(Z^{-2}\right) = 0, \quad m = 1,2,..., \tag{3.31}$$

where $S_{mm}^{+}(s) = s + \sin(2\pi m s)/2\pi m$ and $S_{mm}^{-}(s) = O(s^2)$. This is transcendental equation for the frequency $\kappa = p/\lambda = 2\pi f/c$. If we assume, for simplicity, that graphene is lossless, $1/\tau = 0$, and that the intraband conductivity dominates over the interband one, then we can use (1.16) for graphene's impedance. Selecting the sign "+" before the square root, i.e. at the top sheet of $\gamma_m(\kappa)$, we obtain equation

$$i\sqrt{m^2 - \kappa^2} + i\frac{p\Omega}{4\pi c} S_{mm}^{\pm}(s) + O\left(Z^{-2}\right) = 0, \quad m = 1,2,..., \tag{3.32}$$

This equation has no roots with $\mathrm{Re}\,\kappa < m$, although such a root is present on the bottom sheet, where the sign "–" is selected; it does not show up in the reflectance.

Returning to *the graphene strip grating located on the surface of dielectric substrate,* one has to use full expression (3.18) for Γ_m^E, so that

$$\Gamma_m^E(\kappa)+i\frac{p\Omega S_{mm}^{\pm}(s)}{\pi c}\left(1+\frac{ip}{2\pi c\tau}\right)+O\left(Z^{-2}\right)=0,\quad m=1,2,... \tag{3.33}$$

The expression for $\Gamma_m^E(\kappa)$ is quite complicated, however, it can be simplified under the assumption that the substrate is electrically thin, i.e. $h/\lambda\to 0$, namely,

$$\Gamma_m=2\gamma_m-i\xi(\varepsilon-1)\kappa^2+O(\xi^2) \tag{3.34}$$

Then, the following approximate characteristic equation appears instead of (3.31):

$$\gamma_m(\kappa)-\frac{i}{2}\xi(\varepsilon-1)\kappa^2+i\frac{p\Omega S_{mm}^{\pm}(s)}{2\pi c}\left(1+\frac{ip}{2\pi c\tau}\right)+O\left(\xi^2,Z^{-2}\right)=0,\quad m=1,2,..., \tag{3.35}$$

This equation can be treated analytically in the same way as (3.31). The result is

$$\kappa_{m0}^{L+}=m-\frac{1}{8m}\left[m^2\xi(\varepsilon-1)-\frac{p\Omega S_{mm}^{\pm}(s)}{2\pi c}\left(1-\frac{ip}{2\pi mc\tau}\right)\right]^2+O\left(\xi^2,Z^{-2}\right)=0, \tag{3.36}$$

Therefore, unlike the case of suspended grating, if the parameters of the dielectric substrate, ε and *h*, are fixed, however the strips are vanishing, $s\to 0$, then the LM complex natural frequencies tend to the real numbers, which are redshifted from the RA frequencies,

$$\kappa_{m0}^{L\pm}\to m-\tfrac{1}{8}m^3(\varepsilon-1)^2\xi^2 \tag{3.37}$$

As one can verify, equation (3.37) corresponds to the condition that the grating period equals to *m* wavelengths of the principal guided wave of the dielectric slab TE_0, which has no cutoff frequency. Indeed, this wave propagation constant, g_{TE0}, satisfies the transcendental equation, $\tan\left(\frac{1}{2}\sqrt{k^2\varepsilon-g_{TE0}^2}h\right)=\sqrt{g_{TE0}^2-k^2}\,/\sqrt{k^2\varepsilon-g_{TE0}^2}$ [90]. This equation can be solved analytically if we assume that $h\to 0$ and keep the leading term, yielding $\lambda_{TE0}=\lambda\left[1-\frac{1}{8}k^2h^2(\varepsilon-1)^2\right]+O\left(k^3h^3\right)$ that is in full agreement with (3.37).

For completeness, it should be noted that if the frequency or the substrate contrast or its thickness gets larger, then, besides the principal wave TE_0, the substrate starts guiding similar waves of the higher orders, TE_M, $M > 0$. Therefore, new LM resonances can be expected, mediated by these higher guided waves as well. This guess is indeed supported by computations (see Section 3.5). Thus, LMs should be classified using not one but two indices, $L^{\pm}_{mM}$, where m = 1,2, … and M =0,1,2, … while ± corresponds to the parity in x.

The obtained above expressions show that the LM frequencies of the on-substrate graphene strip grating are always close to the RA frequencies, being red-shifted from them by the values mediated by the guided waves of the substrate. However, because of the presence of the quantity Ω in (3.36), the LM resonances are still tunable, although in much narrower band than the frequencies of the PM resonances, which exist only in the case of the H-polarized wave scattering.

The Q-factors of LMs can be also expressed from (3.36). Provided that the mode is on the top sheet of the corresponding RA, they are

$$Q^{L\pm}_{m0} = \frac{8\pi^2 m^3 c^2 \tau}{p^2 \Omega S^{\pm}_{mm}} \left\{ 1 - \frac{1}{4m^2} \left[m^2 \xi(\varepsilon - 1) - \frac{p\Omega S^{\pm}_{mm}(s)}{2\pi c} \right]^2 \right\} \left[m^2 \xi(\varepsilon - 1) - \frac{p\Omega S^{\pm}_{mm}(s)}{2\pi c} \right]^{-1} \quad (3.38)$$

Note that the quantity in the last brackets can turn zero – this happens when the mode pole coalesces with the RA branching point. Formally, the Q-factor here turns infinite.

3.5 Results of numerical study of wave scattering and absorption

3.5.1 H-case: resonances on substrate, plasmon and lattice modes

Convergence and validaton. To visualize the rate of convergence of the numerical solution, we compute the relative error in the l_2-norm, of the solution found with varying truncation order N as compared to N = 400, and defined as (1.9).

The results in Fig. 2a correspond to the normal and inclined incidence, $\alpha = 90^o$ and 45^o, on the grating with $p = 70\ \mu\text{m}$, $d = 14\ \mu\text{m}$, $h = 10\ \mu\text{m}$ placed on the substrate with relative dielectric permittivity, $\varepsilon = 2.25;\ 5;\ 12$; the frequency is 5 THz that means $\kappa = 1.16$. The graphene parameters are $T = 300\text{K}$, $\mu_c = 0.39\ \text{eV}$ and $\tau = 1\ \text{ps}$ that results in the relative surface impedance $Z = 0.06 - i1.81$.

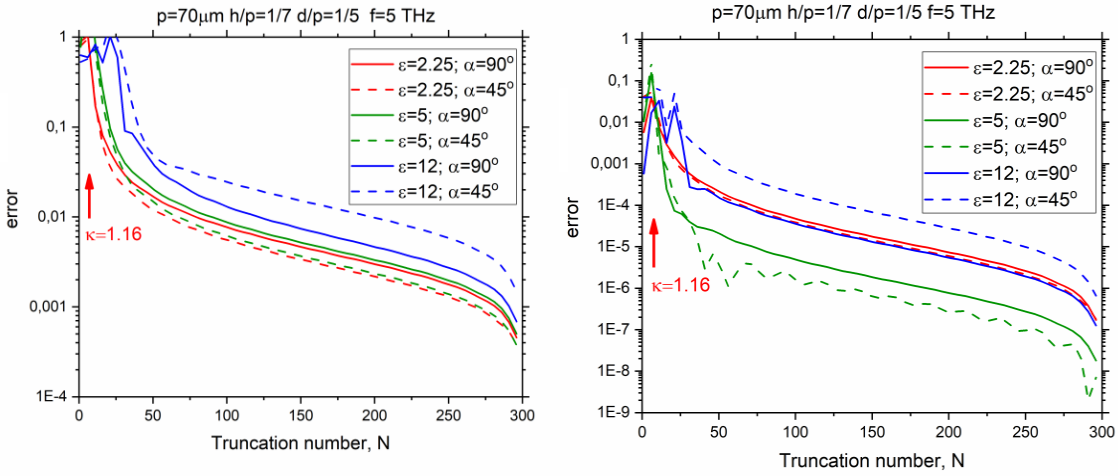

Figure 3.3. (a) The error in the computation of the Floquet harmonic amplitudes using (1.2)-(1.5) versus the matrix truncation order for the grating with parameters indicated in the inset. (b) The error in the computation of the reflectance. The frequency is $f = 5\ \text{THz}$ and the graphene impedance is $Z = 0.06 - i1.81$.

This value can be considered as the near-field error. As one can see from Fig. 3.3a, it starts nearly exponential decay as soon as N becomes larger than certain N_{th}. In the analysis of the plane-wave scattering from gratings, normally the phenomena of reflection, transmission and absorption, in terms of the power fractions, are of the primary interest. Therefore, we define and compute the far-field error as a function of N (1.10). As seen in Fig. 3.3-b, with an increase in N over N_{th}, the error (1.10) starts decreasing similarly to near-field error, however, the value of that error is 1-2 orders smaller than for (1.9). As visible, the rate of convergence is the highest in the case of

absence of dielectric layer and normal incidence, while thinner and optically denser slabs entail larger values of N to achieve the same accuracy. In contrast, the filling factor, d / p, does not change N_{th} or the rate of convergence.

Finally, as a proof of validation, we present in Fig. 3.4 a comparison of our results with those in Fig. 3-a of [42], computed by a conventional MoM code and a MAR-Galerkin with one weighted Chebyshev polynomial approximating the strip current.

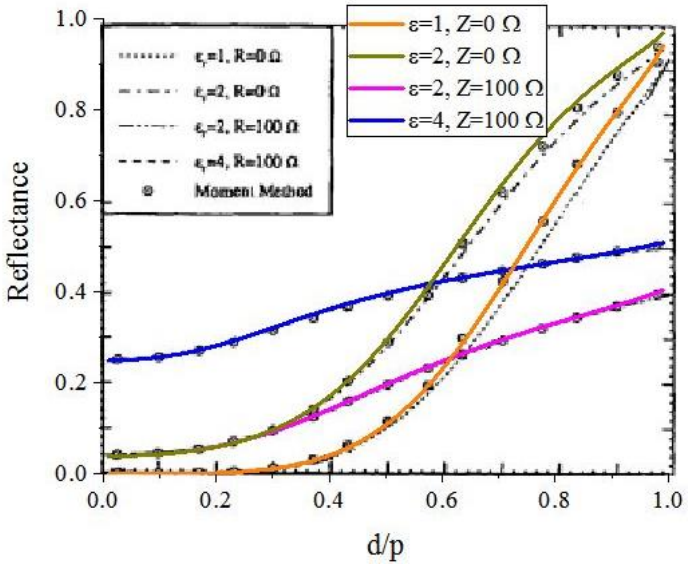

Figure 3.4. Comparison of the results of Fig. 3-a of [42] and MAR-RHP using (1.2)-(1.5). Reflectance of resistive-strip grating with $Z = 100$ Ohm on dielectric substrate versus the ratio d/p at $\kappa = 0.5$, $\alpha = 60^o$, $h / p = 0.2$, and $\varepsilon =$ 2 and 4. The plots for PEC strip array in the free space and on the same substrate are also shown.

Here, the absolute value of the zeroth-order Floquet harmonic is shown versus the filling factor, d/p, at the normalized frequency $\kappa = 0.5$ for resistive-strip grating with $Z = 100$ Ohm on dielectric substrate with $\varepsilon = 2$ and 4 and $h = p / 5$, illuminated by the H-polarized plane wave incident at $\alpha = 60^o$. The PEC-strip case (Z = 0) is also shown, for comparison. The corresponding curves visually overlap; small discrepancy from MAR-Galerkin is explained by too low order of the latter and vanishes if $d / p \le 0.3$.

Numerical results: interplay of resonances. In Fig. 3.5-a, presented are the plots of the reflectance (2.12) versus the frequency in the range from zero to 10 THz at the

normal incidence of the H-polarized plane wave on a grating of graphene strips with rather small filling factor, $d/p=0.2$, in the free space and on a rather thin substrate with $h/p=1/7$ and $\varepsilon=2.25$ and 4.2.

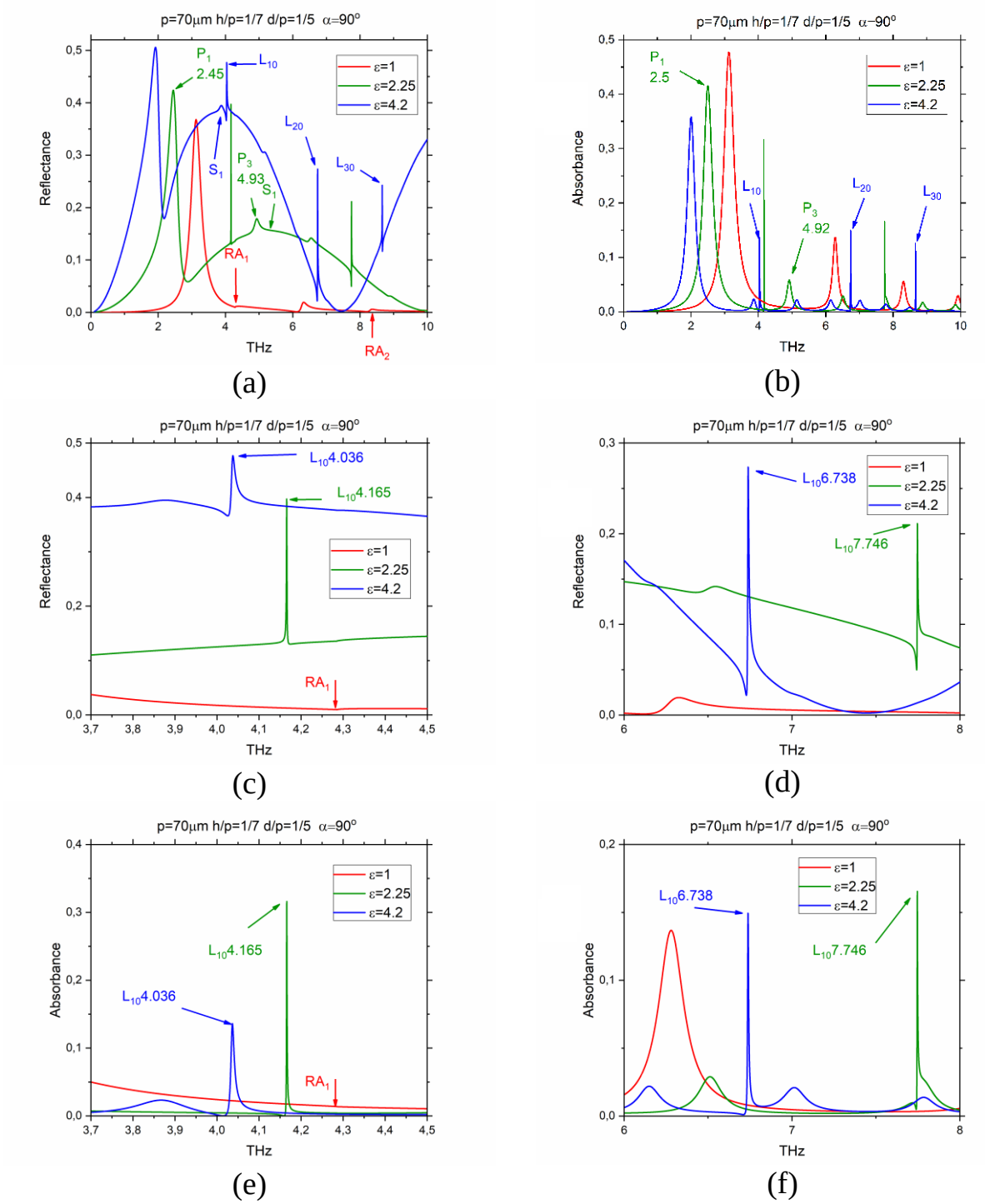

Figure 3.5. The reflectance (a), (c), (d) and absorbance (b), (e), (f) of the free-standing and on-substrate gratings with period $p=70\ \mu$m, $d/p=0.2$ and $h/p=1/7$ versus the frequency for three values of the permittivity, $\varepsilon=1,\ 2.25,\ 4.2$ (a), and zooms of (a) and (b) near the L_{10} (c), (e) and the L_{20} (d), (f) mode resonances.

In computations, we follow [20,24,60] and take the following graphene parameters: temperature $T = 300\text{K}$, chemical potential $\mu_c = 0.39\ \text{eV}$ and electron relaxation $\tau = 1\ \text{ps}$. The latter value is somewhat over-optimistic as the best CVD-graphene samples available today have twice smaller value of the relaxation time; we have selected it to emphasize the plasmon resonances. In the end of this Section, we address the tunability of these resonances with the aid of the potential μ_c.

The plots in Fig. 3.5-b show similar dependences of the absorbance, for the same parameters. We do not show the plots for the transmittance because $P_{tr} = 1 - P_{ref} - P_{abs}$. Note that the RA frequencies, which correspond to $\kappa = 1$ and 2, are found to be 4.286 THz and 8.571 THz, respectively. Besides, one can see several peaks and Fano-shape double extremums of the reflectance and absorbance. They correspond to the natural modes of our metasurface. Zoomed-in spectra on panels (b) and (c) show with better resolution narrow ranges containing sharp peaks on the high-Q LMs L_{10} and L_{20}.

Besides of them, the spectra in Fig. 3.5-a,b reveal medium-Q resonances on the PMs P_1, P_3, P_5. At the normal incidence, the OMs with even indices remain "dark modes:" they are not excited because their eigenfields are orthogonal, in symmetry, to the plane wave. Note that if $\varepsilon = 4.2$ the LM L_{10} hybridises with the PM P_3 around 4.03 THz.The resonance on the principal PM P_1 dominates at the frequencies, lower than the first RA. Its presence, in fact, ruins the so-called Hertz effect of the good transparency, in the H-polarisation regime, of the gratings made of well-conducting wires or strips placed with period, smaller than the wavelength; note that the same takes place for the noble-metal gratings in the visible range [45]. However, enhanced reflection is accompanied with sizeable absorption.

Below 0.5 THz (this value depends on ε and μ_c), on-substrate graphene-strip grating displays rather good polarization discrimination in Hertz sense. Exact position of the principal plasmon resonance P_1 depends on the strip width in accordance with (3.28) that opens opportunities to design tunable sub-THz polarizers.

Panels (b) and (c) demonstrate that, if the optical contrast of the substrate and the host medium gets smaller (the same happens if the substrate gets thinner), then the LM peaks of high reflection and absorption move closer to the RA frequencies and their Q-factors get larger. The distance from RA is mediated by the principal guided wave TM_0 of the dielectric slab in accordance with (3.29).

Finally, we attract attention to the wide bell-like resonances in Fig. 3.5-a that are absent in Fig. 3.5-b, at 4.1 THz for $\varepsilon = 4.2$ and 5.0 THz for $\varepsilon = 2.25$. These are the SM resonances. They do not show up in the absorbance because here the slab is assumed lossless. The presented above identification of the natural modes, which are responsible for the resonances in the THz wave scattering and absorption by the considered metasurface is supported by the near-field portraits, presented in Figs. 3.6 to 3.8.

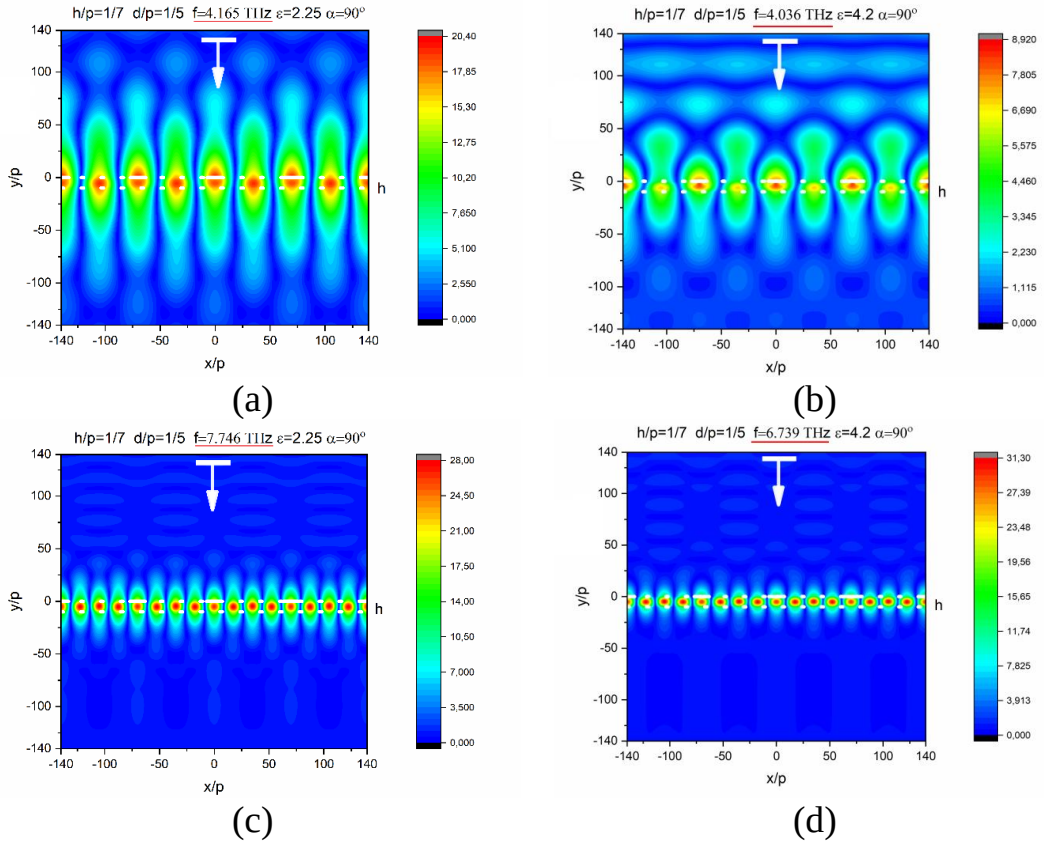

Figure 3.6. The magnetic field patterns on four periods in the resonances on the LMs L_{10} and L_{20} at the normal incidence for the same grating as in Fig. 3.5 with $\varepsilon = 2.25$: (a) $f = 4.165$ THz (c) $f = 7.746$ THz and with $\varepsilon = 4.2$: (b) $f = 4.036$ THz and (d) $f = 6.739$ THz.

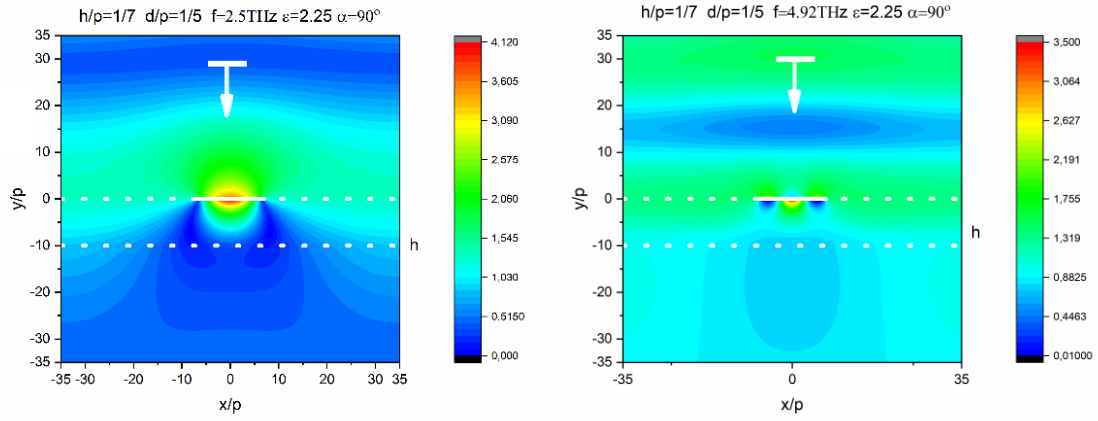

(a) (b)

Figure 3.7. The magnetic field patterns on one period in the resonances on the PMs P_1 and P_3 for the same grating as in Fig. 3.5 with $\varepsilon = 2.25$: (a) $f = 2.5\,\text{THz}$ and (b) $f = 4.92$ THz.

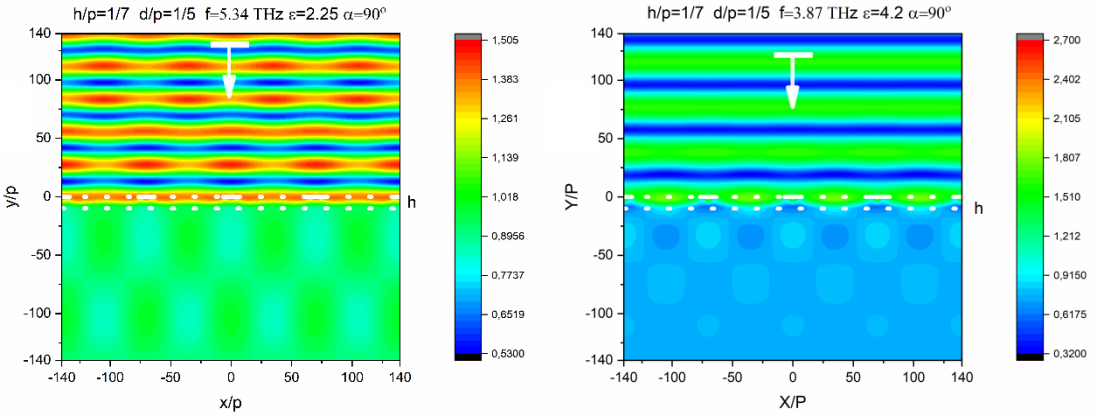

(a) (b)

Figure 3.8. The magnetic field patterns on four periods in the resonances on the SM of substrate, S_1 for the same grating as in Fig. 3.5 with (a) $\varepsilon = 2.25$ at $f = 5.34$ THz and (b) $\varepsilon = 4.2$ at $f = 3.87$ THz.

The next results demonstrate what happens to the spectra of reflectance and absorbance if the angle of the plane-wave incidence starts deviating from the normal. Plots in Fig. 3.9 correspond to the grating with period $p = 70\ \mu$m made of narrow graphene strips with $d = 7\ \mu$m and those in Fig. 3.10 – to the grating of the same period made of wide strips with $d = 63\ \mu$m. Other parameters are the same as in Fig. 3.5.

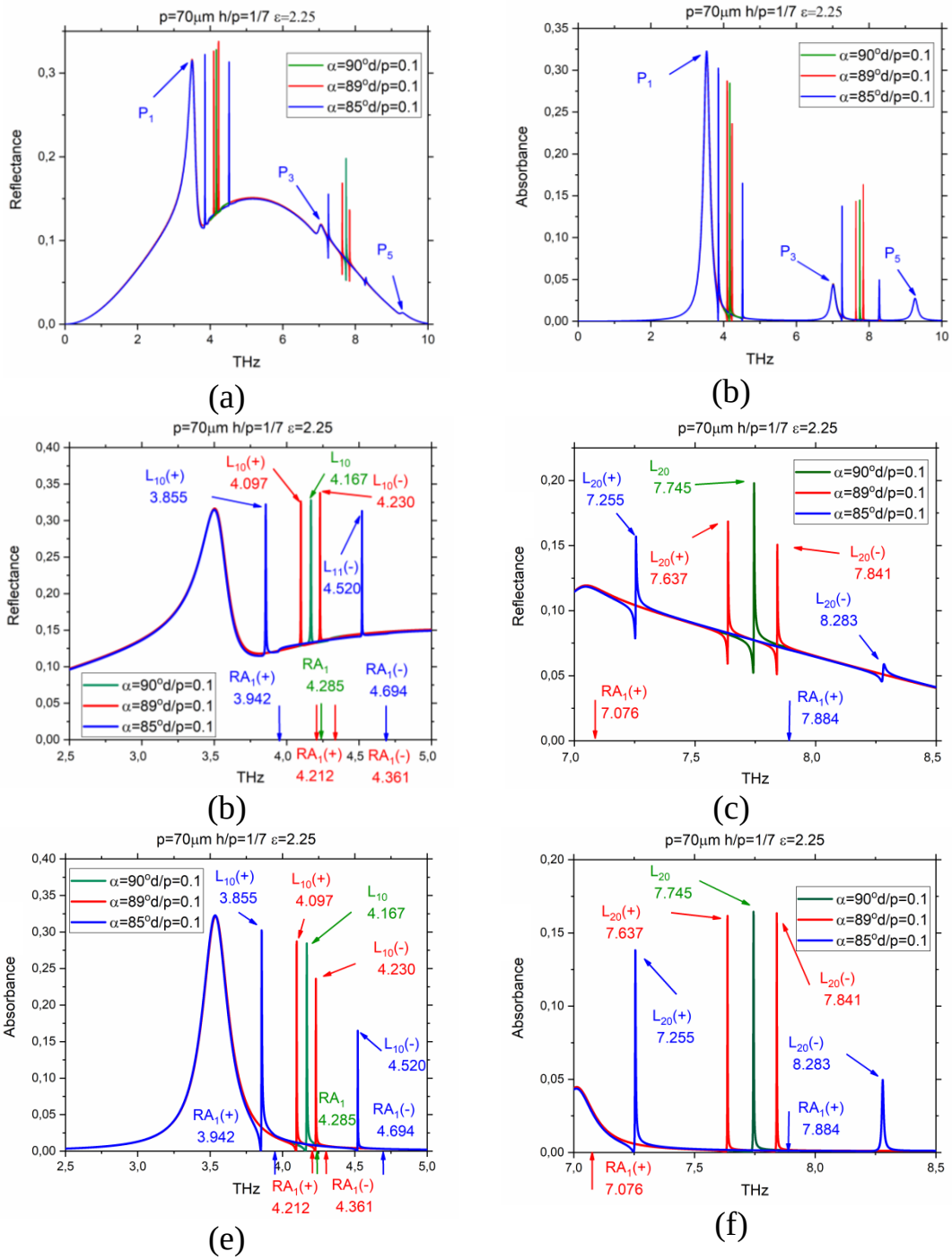

Figure 3.9. Inclined incidence on the on-substrate grating with narrow strips. The reflectance (a), (c), (d) and absorbance (b), (e), (f) for $p = 70\ \mu$m, $h / p = 1/7$, $\varepsilon = 2.25$, and $d / p = 0.1$ versus the frequency at three values of the angle of incidence, $\alpha = 90^\circ$, 89° and 85°. Zooms near LM resonances $L^{\pm}_{10}$ (b) and $L^{\pm}_{20}$ (c), are also shown.

If the strips are narrow (Fig. 3.9), then for this combination of parameters at the normal incidence there is a broad SM resonance S_1 at around 5 THz,

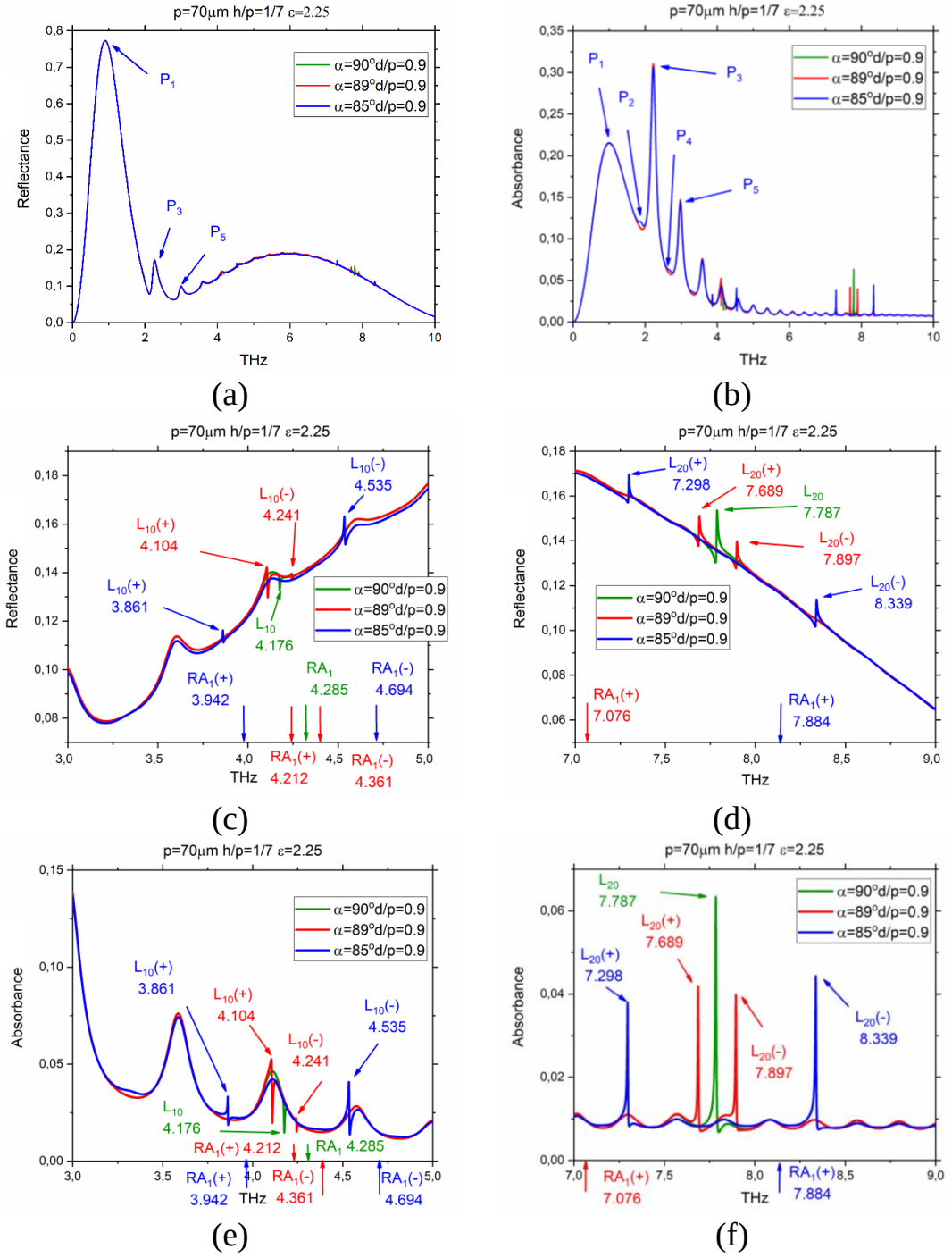

Figure 3.10. Inclined incidence on the on-substrate grating with narrow slots. The reflectance (a), (c), (d) and absorbance (b), (e), (f) versus the frequency at three angles of incidence for the same slab and grating parameters as in Fig. 3.9 except for $d / p = 0.9$. Zooms near the LM resonances $L_{\pm 10}$ (c), (e) and $L_{\pm 20}$ (d), (f), are also shown.

On the red slope of this peak there is a principal PM resonance P_1 at 3.855 THz and on the blue slope – the next P_3 mode resonance, which is much weaker.

Double RA of the orders ±1 is at 4. 286 THz. Slightly red-shifted from this RA is the sharp LM resonance L_{10} and its higher-order sister L_{20} is seen at 7.746 THz. As soon as the angle of incidence departs from the normal, double RA splits to two separate ones for the -1-st and +1-st Floquet harmonics.

Each of them is accompanied with the corresponding LM resonance, on the red side. Note that the negative-index RA is accompanied with resonances on the L_{-mn} modes, which remained "dark" at the normal incidence because their field symmetry was orthogonal to the plane wave. Note that both PM and SM resonances remain intact, so that off the LM frequencies all curves overlap.

If the strips are wide (the grating is a sheet of graphene with narrow slots) as in Fig. 3.10, then at the normal incidence the slab-mode resonance is blue-shifted to 6 THz while the principal plasmon P_1 is red-shifted to 1 THz.

In this case, a departure of the angle of incidence from the normal entails the appearance of split resonances on the LM $L_{\pm 10}$ and $L_{\pm 20}$, less intensive than on the narrow-strip grating. Besides, even-index PM, P_2, P_4, etc. become visible, at least on the plots of absorbance.

As the DC tuneability of conductivity is graphene's most important for applications feature, we have computed the THz spectra of the reflectance, transmittance andabsorbance for various values of the chemical potential, μ_c. These dependences are show in Fig. 3.11-a,b,c.As one can see, larger chemical potentials shift the plasmon-mode resonances to the blue and their peak values get somewhat smaller. This shift eventually yields, at $\mu_c = 1.5\,\mathrm{eV}$, the situation where the real values of the complex natural frequencies of the medium-Q mode P_1 and the high-Q mode L^{+}_{10} coincide. In ths situation, the broad peak of high (75%) reflection because of the PM becomes cut through by a narrower band of low (12%) reflection. In this band, the absorbance also drops to 0.1%, so that the transmittnce exceeds 87%. Such an effect is called *electromagnetically induced transparency*. Due to this effect, by varying the graphee chemical potential, one can change the transmittance/reflectance ratio of the H-

polarised terahertz plane wave, i.e. the transparency of the metasurface, in large dynamical range.

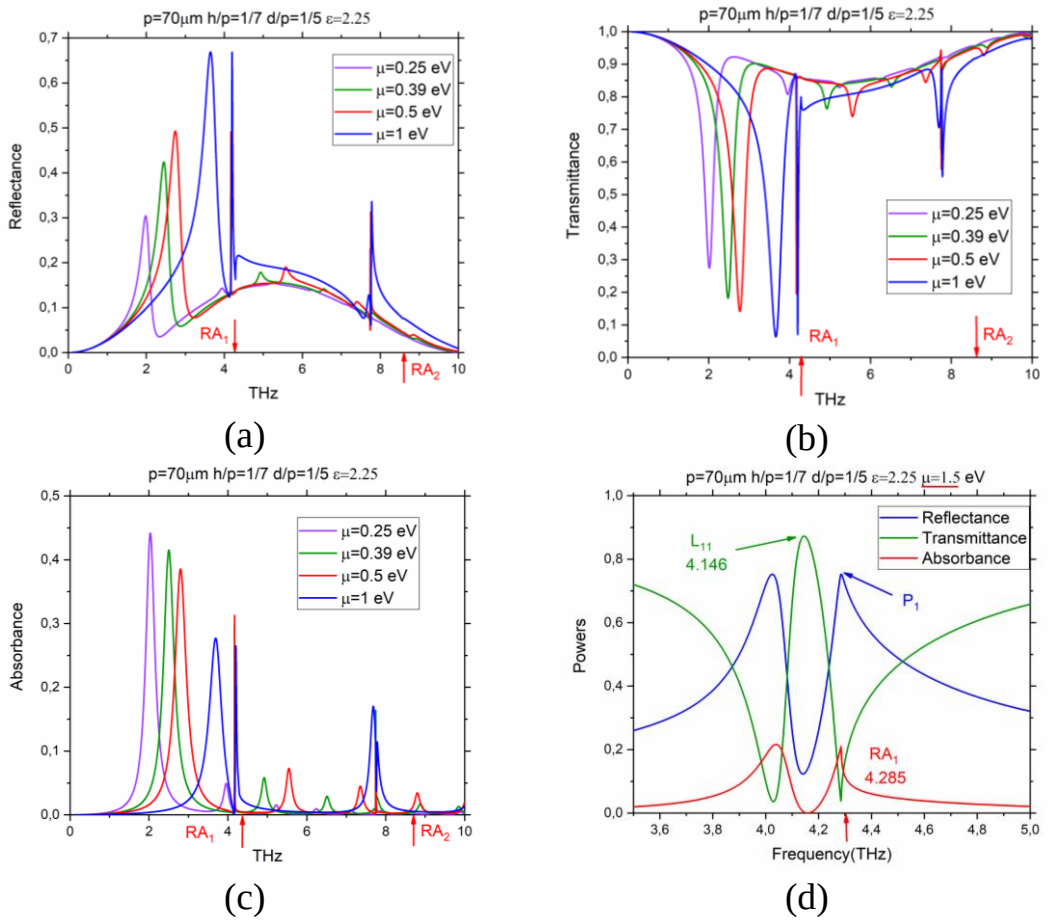

Figure 3.11. (a)-(c) Reflectance, transmittance and absorbance versus the frequency of the H-polarized plane wave, normally incident of the on-substrate narrow-strip grating with $p = 70\ \mu$m, $h/p = 1/7$, $d/p = 0.2$ and $\varepsilon = 2.25$ for four values $\mu_c = 0.25$ eV, 0.39 eV, 0.5 eV and 1 eV. (d) Zoom of the narrow band around P_1, L_{10} and RA_1 frequencies at $\mu_c = 1.5$ eV.

3.5.2 E-case: resonances on substrate and lattice modes

For numerical experiments, we choose the graphene parameters as follows: $\mu_c = 0.39$ eV, $T = 300$ K, and electron relaxation time $\tau = 1$ ps. The latter value is rather optimistic, however, it helps to emphasize the LM resonances. Note that today the

largest values of graphene's chemical potential, achieved with the best available samples, are around 1 eV.

In Fig. 3.12, we show the frequency dependences of the reflectance (a) and absorbance (b) of the studied metasurface in the range from zero to 10 THz, in the case of the normal incidence.

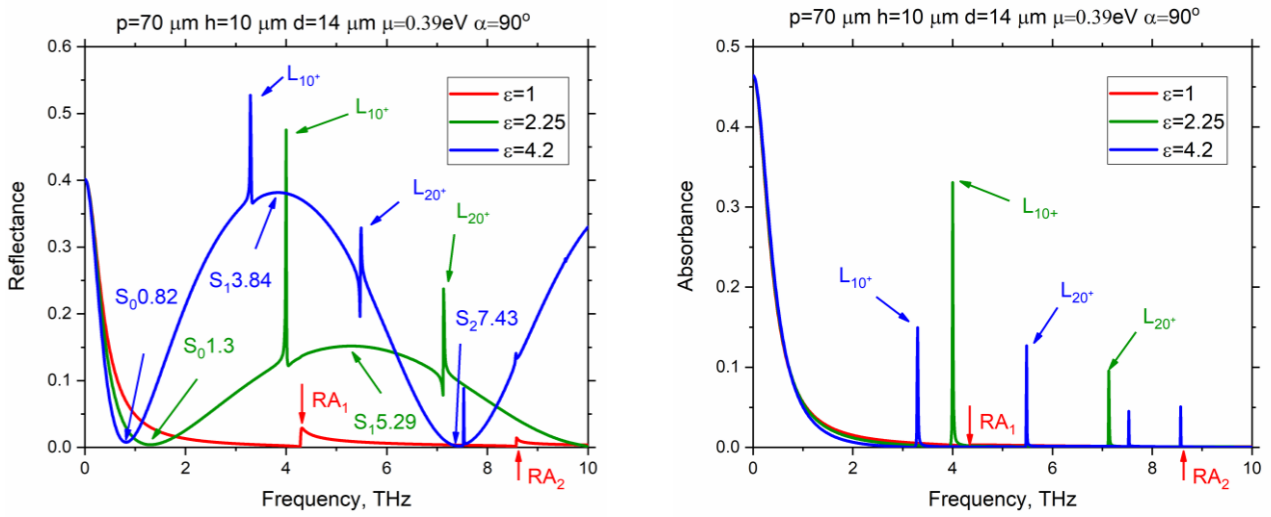

(a) (b)

Figure 3.12. The reflectance (a) and absorbance (b) of the suspended and on-substrate gratings with period $p = 70\ \mu\text{m}$, filling factor $d/p = 0.2$, and relative substrate thickness $h/p = 1/7$, versus the frequency for three values of substrate permittivity, $\varepsilon = 1, 2.25$ and 4.2.

In computations, we use the matrix equation (3.21) truncated to N = 50. The transmittance can be found from the power conservation law, $T = 1 - R - A$, and is not shown. Here, the grating has period of p = 70 μm, the strip width is d = 14 μm, and the substrate thickness is h = 10 μm. Thus, both the filling factor of the grating and the relative thickness of the substrate are rather small, $d/p = 0.2$ and $h/p = 0.143$, respectively. The substrate relative dielectric permittivity is 1 (i.e. the grating is suspended in free space), 2.25 and 4.2. On the plots, one can see several sharp Fano-shape double-extremum peaks, overlapping with a sinus-like background. These are the

ultrahigh-Q LM L_{10}^{+} and L_{20}^{+} resonances on the background of low-Q SM resonances S_0, S_1, and S_2. The positions of the LM peaks are defined by the period and mediated by the wavelength of the principal guided wave TE_0 of the dielectric-slab substrate - see [24,60]. They are always shifted to the red side of the RAs, the first two pairs of which (for the normal incidence, ±1-st and ±2-nd) correspond to $\kappa = 1 \text{ and } 2$ and lie at 4.286 THz and 8.572 THz, respectively. The shift from RA gets larger for larger optical contrast and thickness of the substrate and larger mode index, *m*, which corresponds to the RA index. Note that, for the graphene strip grating suspended in the free space, no resonance peaks of reflectance are observed, however, there are sharp drops of both transmittance and absorbance at the RA frequencies.

Wide bell-like peaks of reflectance in Fig. 3.12a are located at 3.84 THz for $\varepsilon = 4.2$ and at 5.29 THz for $\varepsilon = 2.25$. As mentioned, they correspond to the lowest *y*-odd mode, S_1, of the slab as a Fabry-Perot resonator, slightly perturbed by the presence of strips. They are absent on the plots of absorbance in Fig. 3.12b as the slab is assumed lossless. The broad minima of reflectance are also associated with the SM, however, those which have the *y*-even E-fields when the strips are absent. The lowest of them is S_0, which has zero frequency in the absence of strips; the appearance of strips makes its frequency finite.

In Fig. 3.13, we show in-resonance total electric field portraits computed at the frequencies of the absorbance peaks corresponding to the *x*-even LMs L_{10}^{+} and L_{20}^{+}. Here, the graphene strips are marked as white straight lines and the dielectric-air boundaries are shown as white dotted lines.

The panels (a) and (b) are for the substrate with permittivity 2.25 and the panels (c) and (d) – with permittivity 4.2. They demonstrate the standing-wave patterns both above the grating and in the normal direction. In the +*y* direction, the standing wave appears due to strong reflection of the incident plane wave. The standing wave along the grating is the signature of the corresponding natural LM: two (for L_{10}^{+}) and four (for L_{20}^{+}) bright spots on the period.

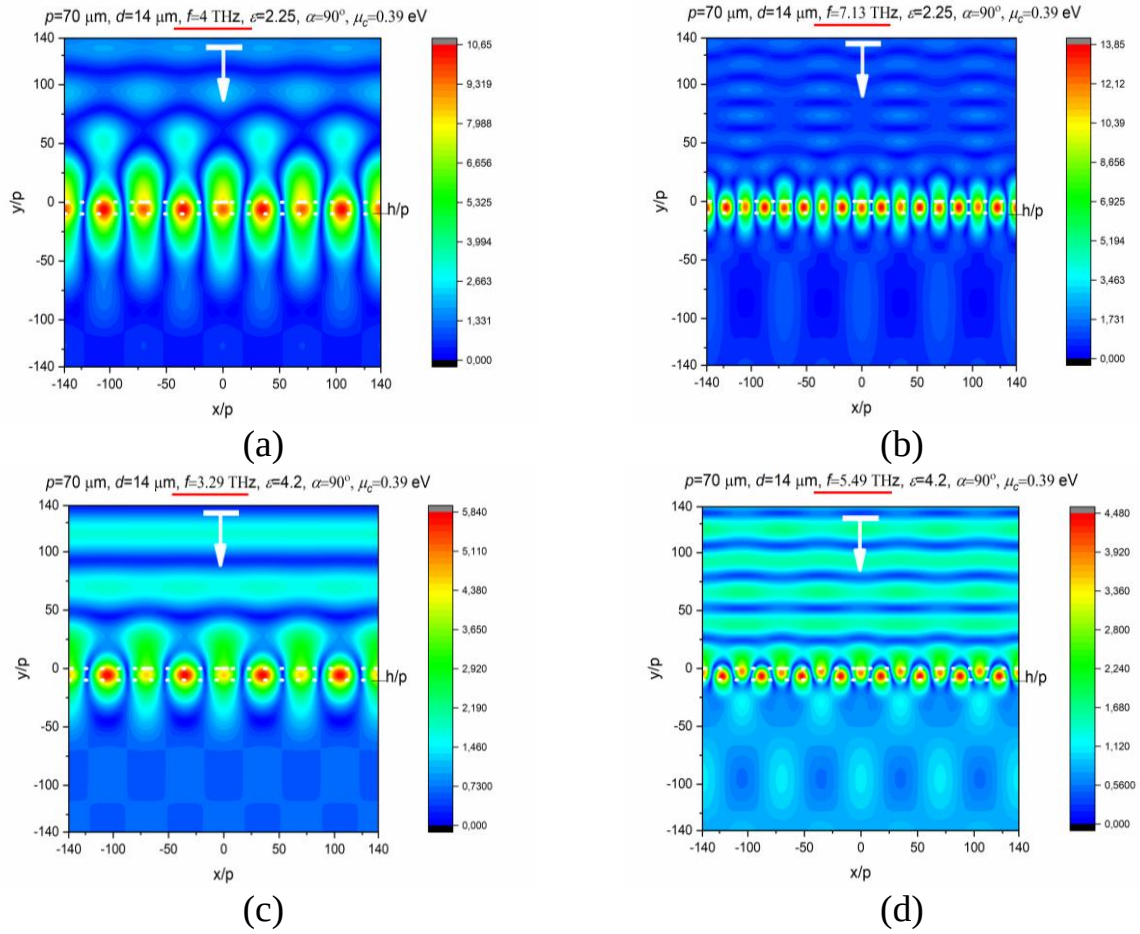

Figure 3.13. The electric field patterns on four periods in the resonances on the LMs L_{10}^{+} ((a) and (c)) and L_{20}^{+} ((b) and (d)) at the normal incidence for the same grating as in Fig. 3.12. The metasurface parameters are indicated at the top of each panel.

This is because in the LM resonances, at the normal incidence, the near field is heavily dominated by the contribution of two Floquet harmonics, namely, ±1-st and ±2-nd, respectively, see eq. (4) in [50]. Note that these harmonics remain non-propagating away from the grating, and their in-resonance amplitudes scale with LM Q-factors. This means that they can be arbitrarily large if the periodicity vanishes because then the frequencies tend to purely real RA values.

For completeness, in Fig. 3.14 we show the near electric field patterns at the resonance frequencies, corresponding to the SM, S_1. They demonstrate the standing wave patterns in the normal direction only, slightly perturbed by the presence of strips. This is as expected as the bare SMs are essentially the modes of 1-D Fabry-Perot etalon.

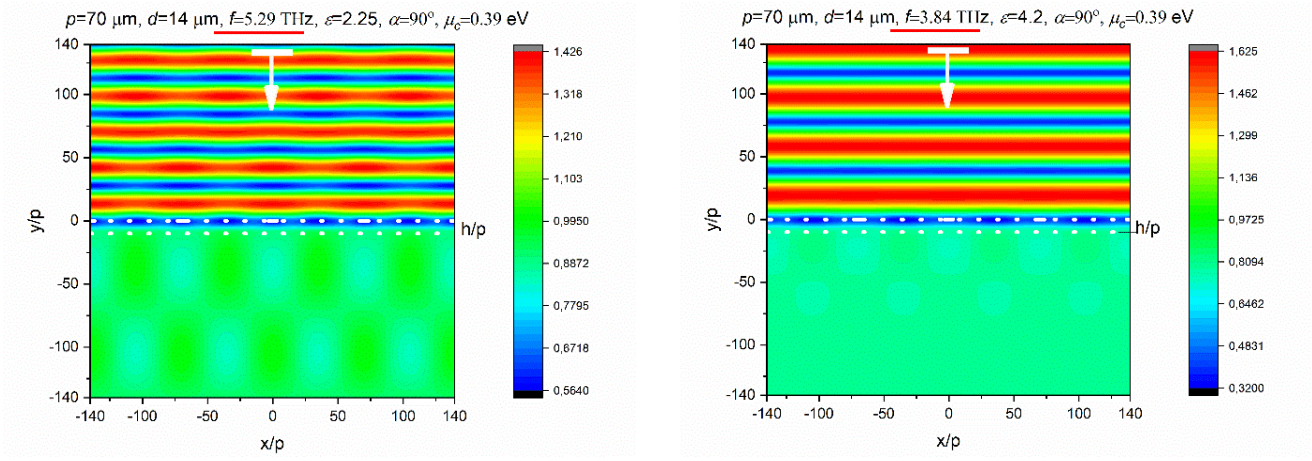

Figure 3.14. The electric field patterns on four periods in the resonances on the SM of substrate, S_1, perturbed by the strips, at the normal incidence on the same grating as in Fig. 3.12 with (a) $\varepsilon = 2.25$ at $f = 5.29$ THz and (b) $\varepsilon = 4.2$ at $f = 3.84$ THz.

The most famous and attractive for application feature of graphene is the tunability of its electron conductivity and hence its impedance, with the aid of DC bias, which controls the chemical potential – see (1.13). Therefore, it is interesting and important to study how the variation of the chemical potential translates to the change of the reflectance, transmittance and absorbance of the patterned graphene configuration. As known, in the case of the H-polarization (magnetic field parallel to the strip edges) the grating of graphene strips possesses the strip PMs [20,24,52,58-60]. PM frequencies strongly depend on the chemical potential because these modes are the natural modes of the Fabry-Perot resonator, where graphene surface wave bounces between the strip edges – see (3.28). The propagation constant of the graphene plasmon wave is determined by graphene's impedance, hence, it scales as the square root of the chemical potential. Thanks to this effect, on-substrate graphene strip gratings are in the core of the design of tunable bio and chemo-sensors [3,8] based on the measurement of the PM resonance peak frequency. The other H-polarization modes of such a grating, SMs and LMs, are much less sensitive to the chemical potential variation.

However, in the E-polarization regime, there is no plasmon natural wave on a sheet of graphene and, therefore, no PMs on the strips. This leaves only the SMs and LMs as

possible candidates for the sensor applications. In Fig. 3.15, we present the spectra of *R* and *A* at 4 values of the chemical potential between 0.25 eV and 1 eV.

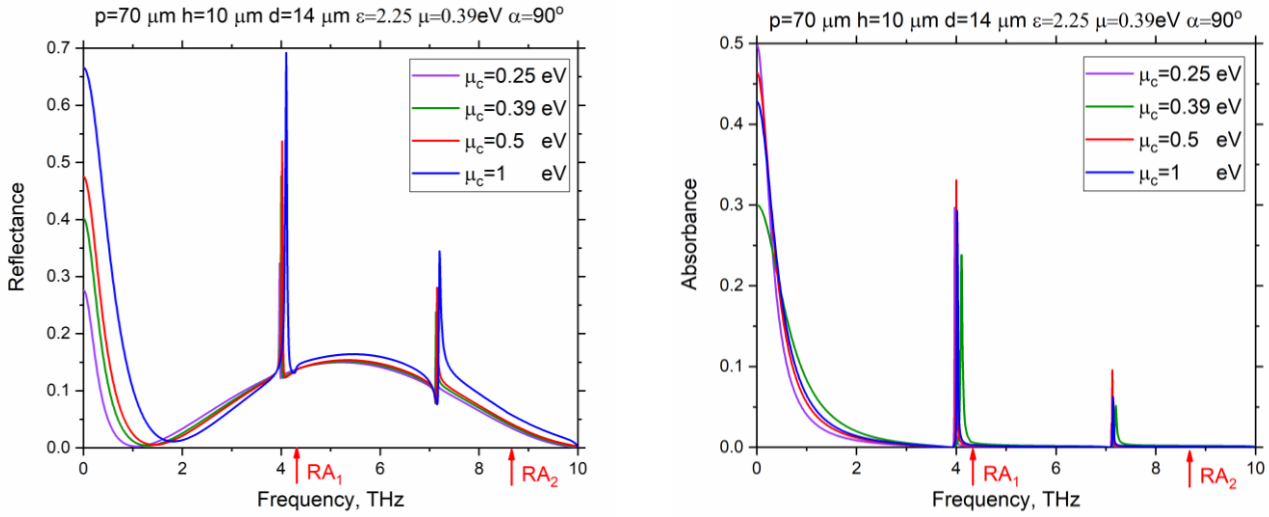

(a) (b)

Figure 3.15. Reflectance (a) and absorbance (b) versus the frequency at the normal incidence on the same grating as in Figs. 3.12 at four values of chemical potential, $\mu_c = 0.25$ eV, 0.39 eV, 0.5 eV and 1 eV.

These plots show that the variation of the chemical potential still has certain effect on the LM resonances. In Fig. 3.16, we present the color maps of the reflectance and absorbance as functions of two parameters, frequency and chemical potential.

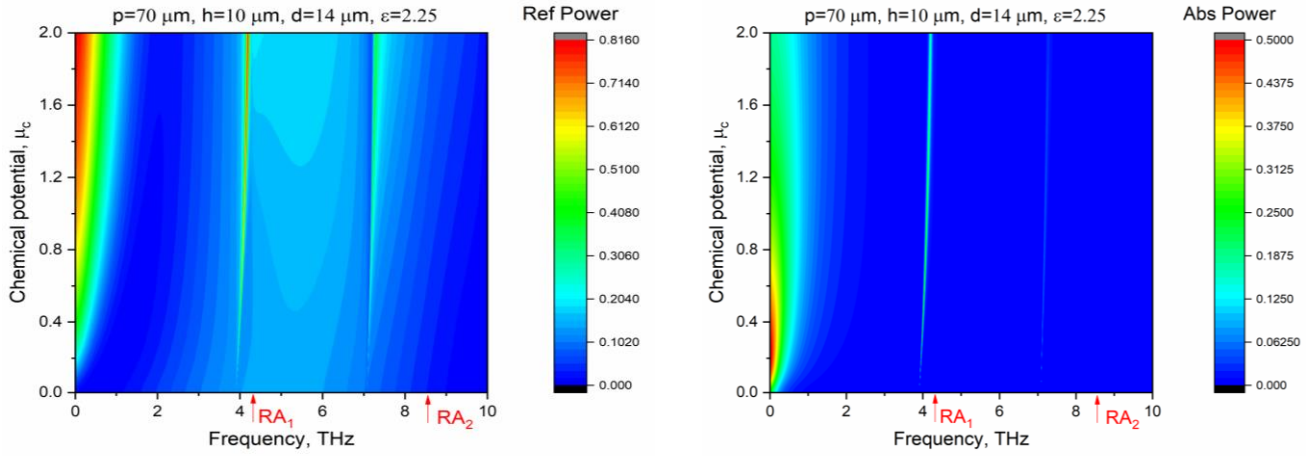

(a) (b)

Figure 3.16. Color maps of reflectance (a) and absorbance (b) versus the frequency and the chemical potential at the normal incidence at the same grating as in Figs. 2-5.

On these maps, the LM resonances show up as bright narrow “ridges” of high reflection located on the red side from the RA frequencies (marked with arrows) and approaching these frequencies as the chemical potential grows up. Note that this is in contrast to the *enhanced transmission* in the LM resonances that is found in the E-polarization scattering from imperfect-metal strip gratings on dielectric substrate [114]. The difference appears due to good transparency of graphene in the THz range in contrast to nearly impenetrable behavior of thin metal film used in [114] in the sub-THz range. As explained in Section 3.4, the LM frequencies and Q-factors can be studied analytically thanks to the regularized nature of equation (3.21).

In Fig. 3.17, we present zooms of the color maps of the reflectance from Fig. 3.16-a near the LM resonances L^{+}_{10} and L^{+}_{20}.

Here, we have added, by white dashed lines, the solutions of approximate equations (3.33), where it is assumed that $1/\tau = 0$, truncated to N = 50. One can see very close agreement between the peak values of R and the real parts of the corresponding LM frequencies.

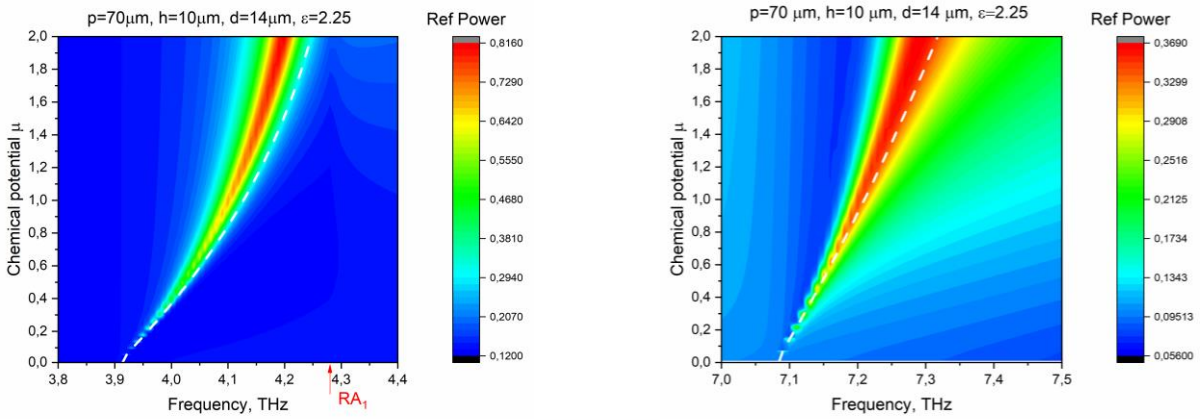

(a) (b)

Figure 3.17. Zooms of color map of reflectance from Fig. 3.16a near the LM resonances L_{10}^{+} and L_{20}^{+}. Dashed white lines show the frequencies found from approximate equation (3.33).

The tunability of the considered LMs is visible well on the maps in Fig. 3.17 where the largest potential is taken as 2 eV.

Another interesting question is the dependence of the LM resonances of the filling ratio, $s = d/p$. Color maps in Fig. 3.18 show the reflectance and absorbance as functions of the frequency and s, computed by the full-wave equation (3.27) truncated to $N = 50$. As visible, the LM resonances remain red-shifted from the RA frequencies for all s, however, this shift gets smaller if $s \to 1$, i.e. if the slots between strips are vanishing.

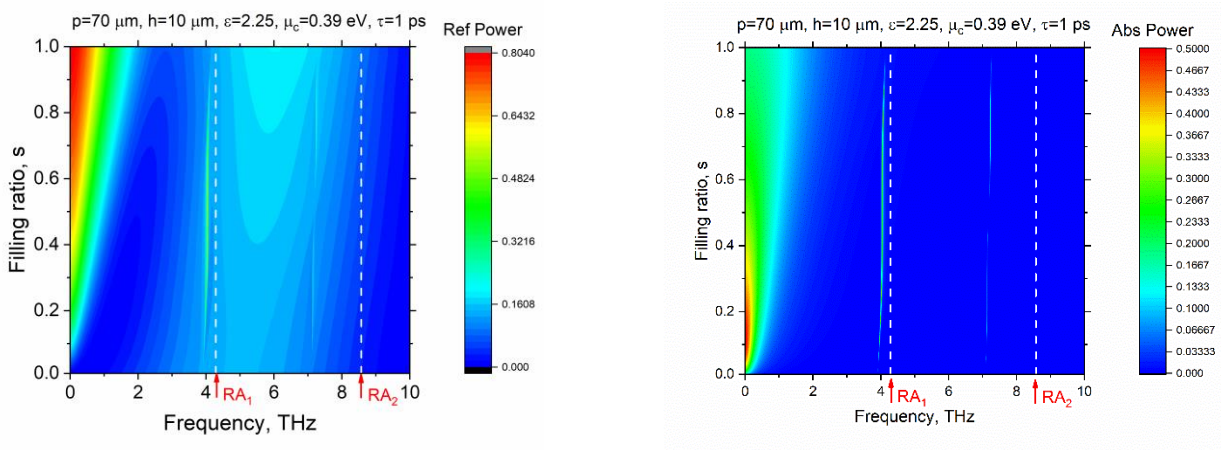

(a) (b)

Figure 3.18. Color maps of reflectance (a) and absorbance (b) versus the frequency and the grating filling factor at the normal incidence at the same grating as in Figs. 3.12-17.

The limiting value of the resonance frequency at $s = 1$ corresponds to the condition that the grating period equals m lengths of the natural wave, guided by the substrate with the upper surface covered with graphene.

In Fig. 3.19, we present the zooms of the color map of the reflectance from Fig. 3.18a in the vicinities of three LM resonances, L^{+}_{10}, L^{+}_{20} and L^{+}_{30} computed from the full-wave equation (3.21) truncated to $N = 50$. For comparison, dashed white lines show the resonance frequencies found from approximate equation (3.33), where it is assumed that $1/\tau = 0$.

One can see very good agreement between these approximations and the peak frequency of R. Note that the number of the peak broadenings corresponds to the mode

index. These broadenings are caused by the drops in the mode Q-factors, which correlate with the overlap of the lossy strip with the LM E-field, see Fig. 3.14.

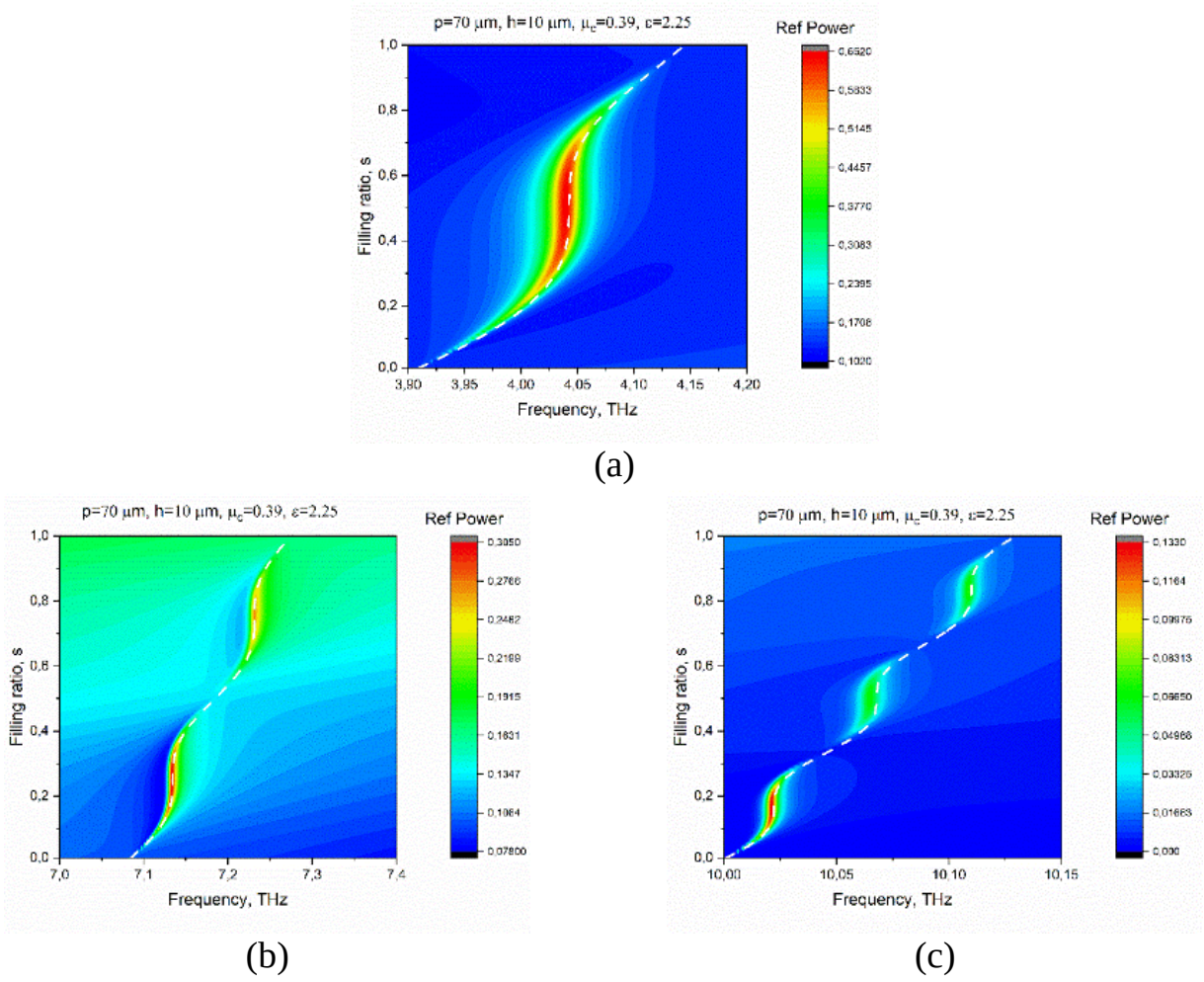

Figure 3.19. Zooms of color map of reflectance from Fig. 3.18-a near the LM resonances L_{10}^{+} (a), L_{20}^{+} (b) and L_{30}^{+} (c); the frequencies of RAs, which correspond to κ=1, 2 and 3 at the normal incidence are 4.286 THz, 8.572 and 12.857 THz. Dashed white lines show the resonance frequencies found from approximate equation (3.40).

Now, if we assume that the strips are narrow, so that the filling ratio is small, $s = \theta / \pi = d / p \to 0$, then for all m and n $S_{m,n}^{+}(s) = 2s + O(s^3)$, and then the complex natural frequencies of LMs tend to real numbers that entails unlimited growth of Q_{m0}^{L+}. The same happens if the substrate vanishes, i.e. if either $\varepsilon \to 1$ or $h \to 0$. At arbitrary s, dependences of Q-factors on s correlate with the overlap between the lossy graphene strip and the mode electric field magnitude.

For instance, if $p = 70\ \mu$m, $h = 1\ \mu$m, $d = 14\ \mu$m, $T = 300$ K, $\tau = 1$ ps and $\mu_c = 0.25$ eV, then $f_{10}^{L+} = 4.3124$ THz and $Q_{10}^{L+} = 431.15$, while if it is 1 eV, then $f_{10}^{L+} = 4.2857$ THz and $Q_{10}^{L+} = 107.79$.

3.6 Regime of electromagnetically induced transparency

In this section, we focus on the EIT regime, which was mentioned in Section 3.5. Here, we take T = 300 K and τ = 1 ps, consider the normal incidence, and select the strip width, grating period, and substrate thickness in the tens of μm. This places the frequencies of all natural modes to the THz range. However, similar effects take place in the near-infrared if the mentioned parameters are taken in the tens of nanometers.

As known, the DC tunability of conductivity is the most important for applications feature of graphene; it is quantified using the graphene chemical potential. Therefore, it is interesting to study the effect of μ_c on the grating characteristics – see Fig. 3.20-a.

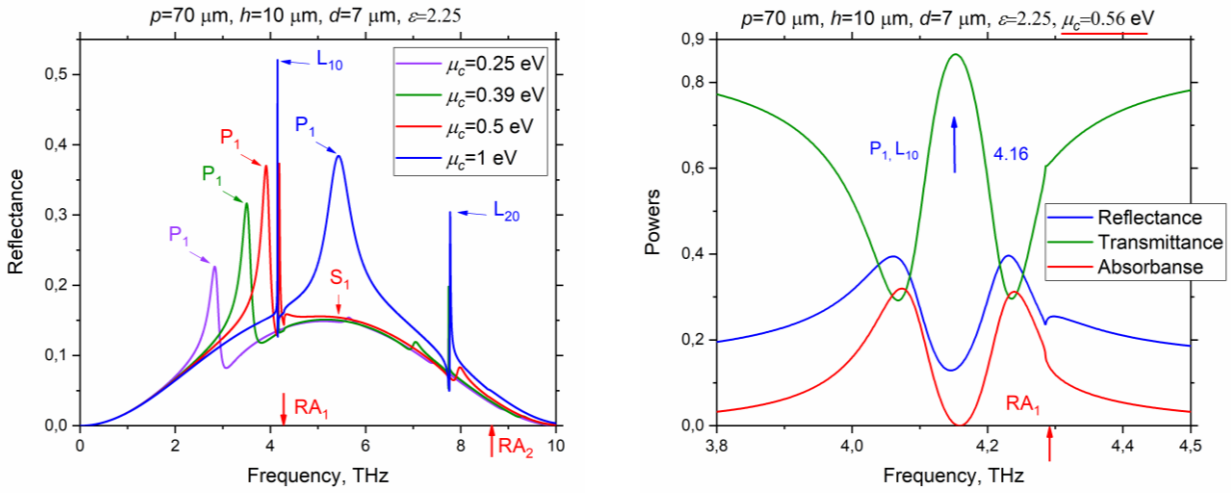

(a) (b)

Figure 3.20. Reflectance versus the frequency at the normal incidence on the grating with period p =70 μm, d = 7 μm and h =10 μm (a) at four values of the chemical potential, μ_c = 0.25 eV, 0.39 eV, 0.5 eV, and 1 eV and (b) zoom of the reflectance, transmittance and absorbance of graphene-strip grating in the narrow band around P_1, L_{10} and RA_1 frequencies at μ_c = 0.56 eV.

It shows the behavior of the reflectance of the studied metasurface with p = 70 μm, d = 7 μm and h = 10 μm as a function of the THz frequency, at normal incidence and four values of graphene's chemical potential, μ_c = 0.25 eV, 0.39 eV, 0.5 eV, and 1 eV.

Here, the marks $RA_{1,2}$ indicate the positions of the first and the second Rayleigh Anomalies, where the ±1-st and ±2-nd diffraction orders start propagating. Broad bell-like resonance at 5 THz is caused by the lowest SM, which is S_0. Its frequency is controlled by h and ε (3.25) and does not depend on μ_c. The sharp spikes just below RAs are the LM resonances L^+_{10} and L^+_{20}, respectively. They are controlled by the grating period p and the wavelength of the lowest guided mode of the dielectric slab. A moderate-Q peak, which shifts to the blue for the larger μ_c is for the PM resonance, P_1. Note that the latter peak has Fano shape if it sits on the slope of the broader S_0 peak.

The PM frequencies and associated Q-factors of a single graphene strip can be found analytically, viewing the strip as a one-dimensional surface-wave Fabry-Perot resonator, i.e. neglecting the radiation losses of PMs. Then the approximate expressions are obtained as (3.28) and (3.29), respectively. They show that both the graphene-strip PM frequencies and their Q-factors scale as $\sqrt{m\mu_c / d}$.

This behavior is clearly visible on the color maps of the reflectance, transmittance and absorbance of the same metasurface, shown in Fig. 3.21. These maps demonstrate a complicated interplay of the tunable medium-Q plasmon-mode resonances, P_1, P_2, with the fixed-frequency high-Q LM resonances, L^+_{10}, L^+_{20}, if their frequencies coincide. Additionally, the background is set by the fixed-frequency low-Q resonance S_1. The cuts of these maps at $\mu_c = 0.56\,\text{eV}$ are shown in Fig. 3.20-b. Here, the broad peak of high reflection on P_1 becomes split by a narrower band of very low reflection on L^+_{10}, accompanied by the negligible absorption – this is EIT-1 regime. Similar however weaker EIT effect takes place at a higher frequency where P_2 hybridizes with L^+_{20}, marked as EIT-2. Note that earlier the EIT effect was reported for the gratings of thin silver nanostrips and nanowires in the visible-light range [45]; it appeared due to the coupling between the low-Q PM and the ultrahigh-Q LM if their frequencies coincided.

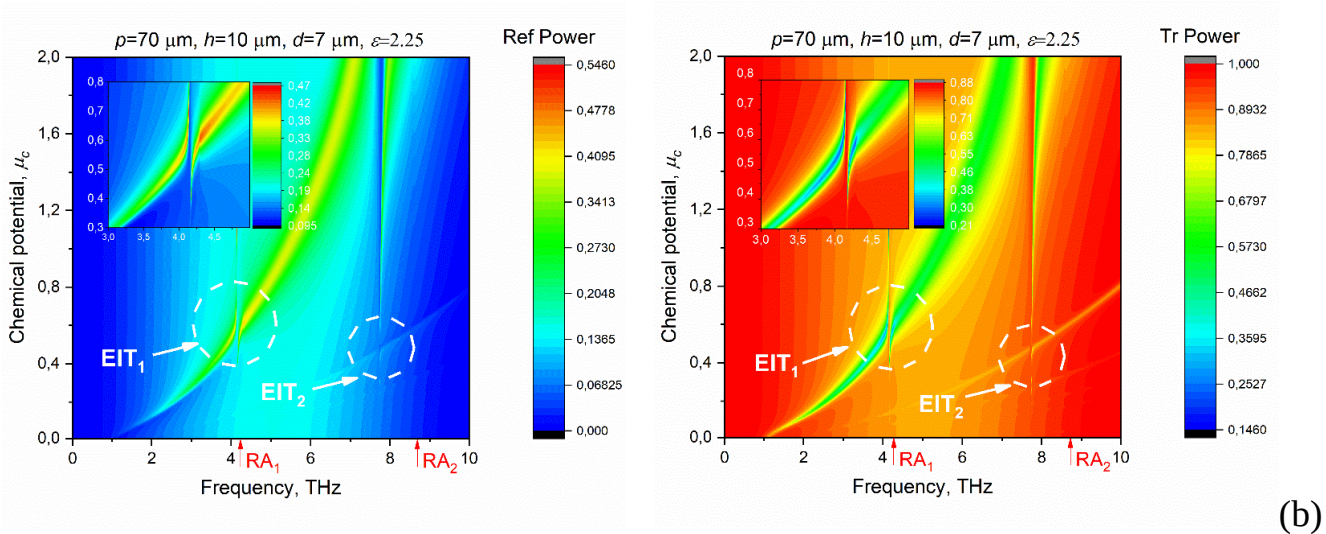

(a) Reflectance

(b) Transmittance

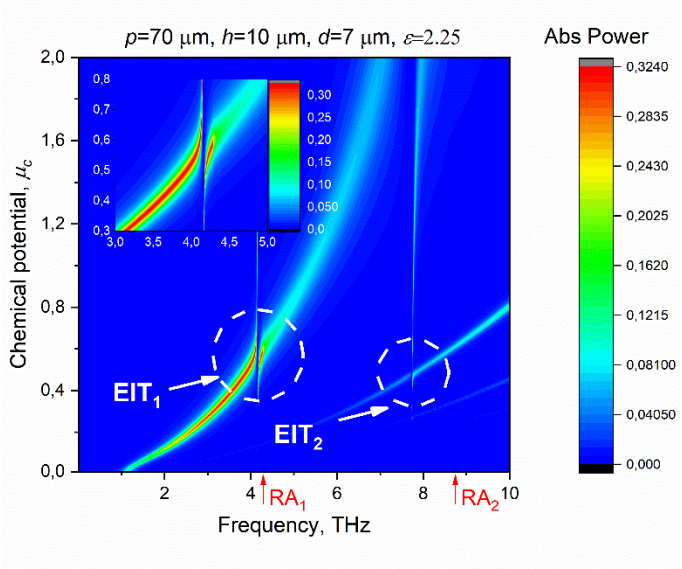

(c) Absorbance

Figure 3.21. The color maps of the reflectance (a), transmittance (b) and absorbance (c) versus the frequency and chemical potential, at the normal incidence of the H-polarized plane wave at the same grating as in Fig. 3.18.

It is known that EIT takes place in electric circuits and even in mechanics when two resonance contours are coupled, one with low Q-factor and another with high Q-factor, and their frequencies coincide [115]. More recently, all-optical EIT effects started attracting attention [116]; they can be found both in configurations with two coupled cavities and within a single cavity. In our case, each graphene strip is an open cavity, supporting the PMs, and the whole grating is also an open cavity, supporting the LMs; they are optically coupled. What is less expected, the absorbance of the graphene-

strip grating at EIT is extremely low. Moreover, the cuts through the maps of Fig. 3.21 at the frequency of EIT-1 and EIT-2, shown in Fig. 3.22 (a) and (b), respectively, reveal practically total loss of tunability of the metasurface with respect to the chemical potential. This combined effect has not been, apparently, reported earlier and is explained by the same reason, which becomes clear after visualizing the near-field pattern at EIT, i.e. at the LM frequency.

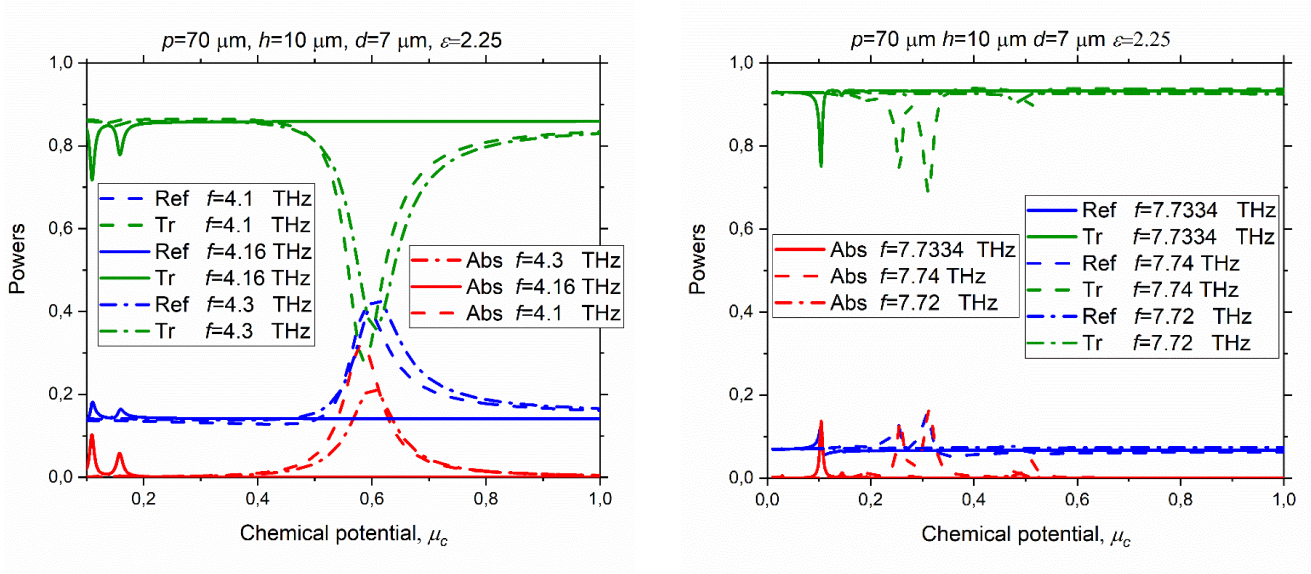

(a) (b)

Figure 3.22. The reflectance, transmittance and absorbance of the on-substrate graphene strip grating of the same parameters as in Figs. 3.20 versus the chemical potential of graphene at the frequencies of 4.1 THz, 4.16 THz (EIT-1 regime) and 4.3 THz (a) and 7.72 THz, 7.7334 THz (EIT-2 regime) and 7.74 THz (b).

In Fig. 3.23-a, such a pattern is shown for the absolute value of the magnetic field (normalized by the incident plane wave magnitude) at the L^{+}_{10} frequency.

This pattern reveals two bright spots on the unit period, one at the strip and the other at the slot. These two spots have opposite phases and such a standing wave is a signature of the first-order LM (see Chapters 2 and 3). As already mentioned, at the L^{+}_{10} resonance frequency this standing wave is formed by the ±1-st Floquet harmonics, which dominate over all other harmonics with amplitudes scaling as the Q-factor, however remain attenuating at the normal to the grating direction, $|y|\rightarrow\infty$.

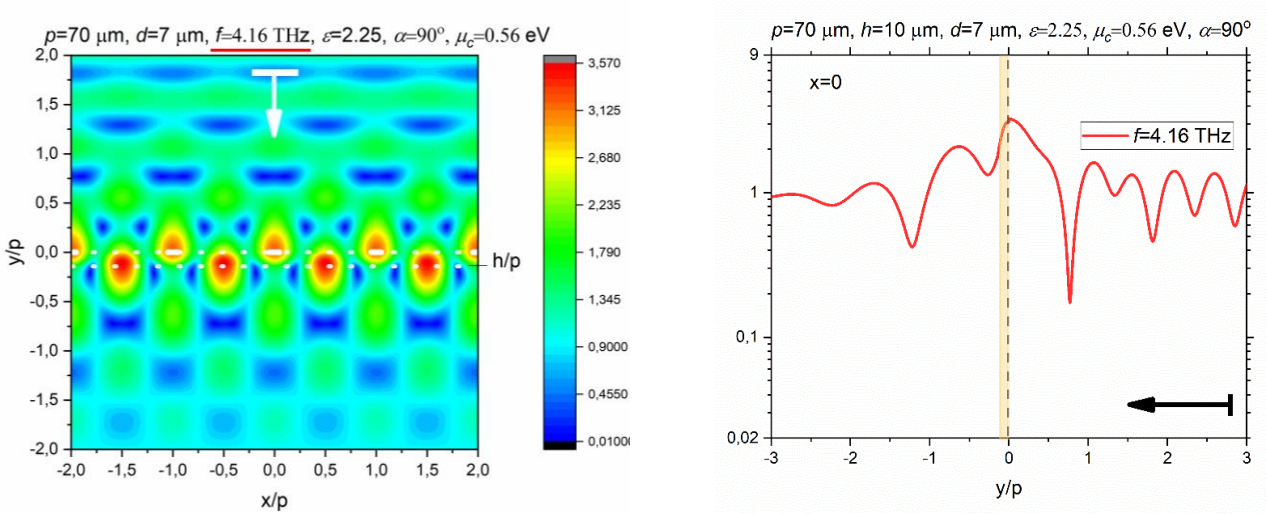

Figure 3.23. The magnetic field pattern on four periods of graphene-strip grating at the frequency of EIT-1 due to the hybridization of the LM resonance on L^{+}_{10} and the PM resonance on P_1 (a), and the magnetic field absolute value along the normal to the strip midpoint, $x = 0$, at this frequency (b), for the same parameters as in Figs. 3.20-3.22 and $\mu_c = 0.56$ eV.

The cut of the near magnetic field magnitude through the strip center (Fig. 3.23-b) also shows a maximum at the strip, together with the field continuity. Now, one should remember that, in the case of the H-polarization, the electric field vector is within a constant the gradient of the magnetic field *z*-component. Therefore, the bright spots of electric field appear at the nods of the magnetic field and vice versa. This means that, in the LM resonance, the lossy graphene strips (which are one-tenth of the period in our case) sit in the deep minima of the electric field. Besides, as the magnetic field in EIT is continuous across the strip, then the induced electric current is close to zero. These LM-field features minimize the graphene strip losses, which are a product of Re Z and the integral, over the strip width, of the squared absolute value of the current.

In addition, these features spoil the tunability of the grating scattering characteristics, in the sense that the DC bias, translated via the chemical potential, has no effect on the transmittance-to-reflectance ratio of our metasurface. In the other

words, in EIT regime, the graphene tunability as a material becomes irrelevant because of a stronger all-optical mechanism, which is enforced by the periodicity.

Such a behavior is observed so far as the strips are narrow, narrower than approximately a quarter of the period if the EIT is associated with the lowest LM, L^{+}_{10}. If the strips are wider and approach a half of the period, then certain absorption appears in the form of small bump at the LM frequency, and the bump height is larger for the larger chemical potential. This is because, if the strips are wide, then their edges "stretch out" of the near-zero E-field spots of the lattice mode L^{+}_{10} and therefore some current is induced that leads to absorption. In the EIT regimes associated with the higher-order lattice modes, L^{+}_{20}, L^{+}_{30}, etc., the strips have to be even narrower to spoil the tunability because these mode E-fields have 4, 6, etc. near-zero spots on the period.

This interpretation is supported by the near magnetic field pattern and its corresponding *y*-dependence, presented in Fig. 3.24-a and 3.24-b, respectively.

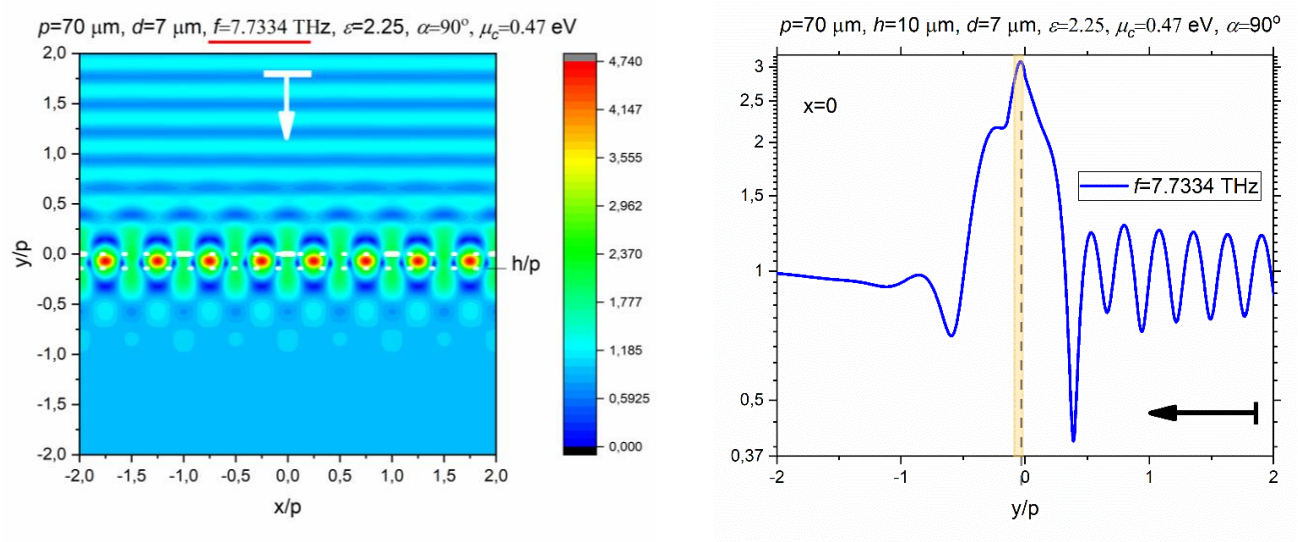

(a) (b)

Figure 3.24. The magnetic field pattern on four periods of graphene-strip grating at the frequency of EIT-2 due to the hybridization of the LM resonance on L^{+}_{20} and the PM resonance on P_3 (a), and the magnetic field absolute value along the normal to the strip midpoint, $x = 0$, at this frequency (b), for the same parameters as in Figs. 3.20-3.22 and $\mu_c = 0.47$ eV.

Although the tunability of the scattering from the studied grating is lost at EIT, the effect of the chemical potential is still present even then, however, in different manner. As follows from (1.13) and (1.14), for the larger chemical potentials, graphene's losses scale approximately as the inverse chemical potential. Due to this, the IET band gets slightly narrower if the potential is larger.

Conclusions to Chapter 3

Using MAR technique based on the analytical solution of the RHP as fast and trusted numerical instrument, we have studied the interplay, in the whole THz range, of the resonances in the plane-wave scattering and absorption, caused by the H-polarized natural modes of three types. Two of them are well-known low-Q SMs of the substrate and moderate-Q PMs of the graphene strips. Still, besides of them, the considered composite metasurface possesses ultrahigh-Q LMs of various orders. The existence of these modes is the consequence of two factors: periodicity and presence of the substrate. This can be seen in the fact that their frequencies are tied to the RA frequencies but shifted from them by the factors, which are determined by the normalized wavenumbers of the guided waves of the substrate.

In the E-polarization case, we have used the mathematically grounded MAR-IDFT technique to study numerically the scattering and absorption of THz-range electromagnetic plane wave by the metasurface shaped as array of graphene strips on flat dielectric substrate. With the aid of this trusted and efficient modelling instrument, we have analyzed the effect of the resonances, caused by the E-polarized natural modes of two types: low-Q SMs and ultrahigh-Q LMs of the whole configuration as a periodic open resonator.

Additionally, assuming that the substrate is lossless but graphene strips are lossy, we have derived the mathematically grounded full-wave asymptotic expressions for the complex frequencies and Q-factors of Ps and LMs. These expressions are in good agreement with numerical results.

This analysis shows that LMs do not exist if the graphene strip grating is suspended in the free space, in the sense that the corresponding complex poles are located at the bottom sheets of the corresponding RA Riemann surfaces. However, if the grating is supported by a dielectric substrate, these complex-frequency poles migrate to the top sheets and appear from the red side of the RAs, which are the field function branch points. The shift from RAs is controlled by the wavelength of the principal guided wave of the dielectric slab substrate. This means that the LM Q-factors grow up infinitely if strips get narrower or if the substrate gets thinner or if substrate's contrast with the host medium vanishes.

Remarkably, the LM frequencies are still tunable with the aid of the graphene chemical potential, although within much narrower range than that of the strip plasmon modes of the same grating in the case of the H-polarization.

Note that, even if the substrate is moderately thin, say, has the thickness of 1 μm, the LM Q-factors can reach 10^{10}, so that the numerical solutions must deliver 10 or more correct digits. Such high accuracy is not accessible with any existing today commercial code, however can be provided by our developed above MAR-based codes.

We have demonstrated that thanks to the tunability of PMs with the aid of graphene's chemical potential, it is possible to realize the DC-bias controlled electromagnetically induced transparency in the THz range, on the metasurface of microsize period. This can be useful in the design of novel tunable filters, modulators and absorbers that use periodically patterned graphene.

The results related to Chapter 3 were published as journal papers [A1 – A3] and conference papers [A8 - A11].

CHAPTER 4
LASING THRESHOLD CONDITIONS FOR GRAPHENE STRIP GRATING ON GAIN-MATERIAL SUBSTRATE

In the previous chapters, we studied the scattering and, in the case of the graphene strips, the absorption of the H- and E-polarized plane waves by infinite flat strip grating lying on flat passive ($\varepsilon'' \geq 0$) dielectric substrate. This study has revealed multiple resonance effects of different families and symmetry classes. Each of these resonances is caused by the underlining complex pole of the field as a function of the frequency. These poles form discrete set on the complex domain of the frequency variation. They coincide with the characteristic numbers of the corresponding matrix operator equations, (3.15) for the H-polarization and (3.21) for the E-polarization. Thanks to the Fredholm second-kind nature of these equations, each pole (i.e. its real part and its imaginary part) is a piece-continuous function of the other parameters, such as substrate thickness, relative permittivity, grating period, strip width, and all the parameters of the graphene. Here, substrate's dielectric permittivity can be complex-valued – which means that the poles are piece-continuous functions of both $\varepsilon' = \mathrm{Re}\,\varepsilon$ and $\varepsilon'' = \mathrm{Im}\,\varepsilon$. In the case of non-magnetic materials, the same is true for the the real the imaginary parts of the refractive index, $\nu = \nu' + i\nu''$, because $\varepsilon = \varepsilon' + i\varepsilon'' = (\nu')^2 - (\nu'')^2 + 2i\nu'\nu''$.

The materials with $\varepsilon'' < 0$, or, equivalently, with $\nu' > 0$ and $\nu'' < 0$, are the gain materials, which can be semiconductors, erbium-doped crystals, or dye-doped polymers demonstrating quantum effect of inverse population under the pump. For brevity, such materials are commonly called "quantum" ones, and the quantity $\gamma = -|\nu''|$ is called the gain index. Then, each complex-frequency pole depends piece-continuously on $\gamma = -|\nu''|$. As explained in section 1.4, in the passive open resonators, where $\nu'' \geq 0$ and the radiation into the host medium is always present, the Complex Poynting Theorem prohibits the existence of purely real mode frequencies. However, if ν'' varies across zero and becomes negative, then real natural frequencies are possible. Determining the value of $\gamma = -|\nu''|$, needed to make the mode frequency real, is the

same as finding the threshold of lasing. Thus, as mentioned in Chapter 1, to model the lasing modes at the threshold, it is necessary to look for the pairs of real numbers (k_s, γ_s) - this is to study the LEP.

In this Chapter, we investigate the H and E-polarized lasing modes of infinite flat grating of graphene strips lying on dielectric-slab substrate, on the threshold of their stationary emission. As in Chapter 3, the conductivity of graphene is modelled using the Kubo formulas, while the substrate material is assumed to have gain that offsets the radiation and ohmic losses and allows the modes to reach the lasing threshold. We look for the frequency and the gain index threshold values, specific to each mode, as eigenvalue pairs (eigenpairs, (k_s, γ_s)). To find them, we reduce the field problem, in each of two polarizations, to a DSE for the complex amplitudes of the Floquet spatial harmonics, which we analytically regularize based on the inversion of the static part of the grating-in-free-space problem. This yields a complex-valued Fredholm second-kind infinite determinantal equation for eigenpairs. Increasing the matrix truncation number guarantees the convergence of these quantities to their exact values. Using these equations in combination with iterative root-search techniques, we determine the eigenpairs with prescribed accuracy and thus, quantify the mode threshold conditions.

4.1 Modified eigenvalue problem formulation

We consider the 2-D LEP for a harmonic in time $e^{-i\omega t}$, H and E-polarized electromagnetic field in the configuration presented in Fig. 4.1. The grating of zero-thickness infinite along *z* graphene strips is assumed infinite in *x* and lies on the top interface $(y = 0)$ of the flat dielectric substrate. The strip width is *d*, the period is *p*, the substrate thickness is *h* and its relative dielectric permittivity is $\varepsilon = \varepsilon' + i\varepsilon'' = (\alpha - i\gamma)^2$. Here, the refractive index α is known and the gain index $\gamma > 0$ is unknown. Within the LEP, we look for the frequency and the gain index threshold, specific to each mode, as the real eigenpairs, (k_s, γ_s), of the following boundary value problem for the function $H(\vec{r})$ or $E(\vec{r})$, $\vec{r} = (x, y)$, respectively:

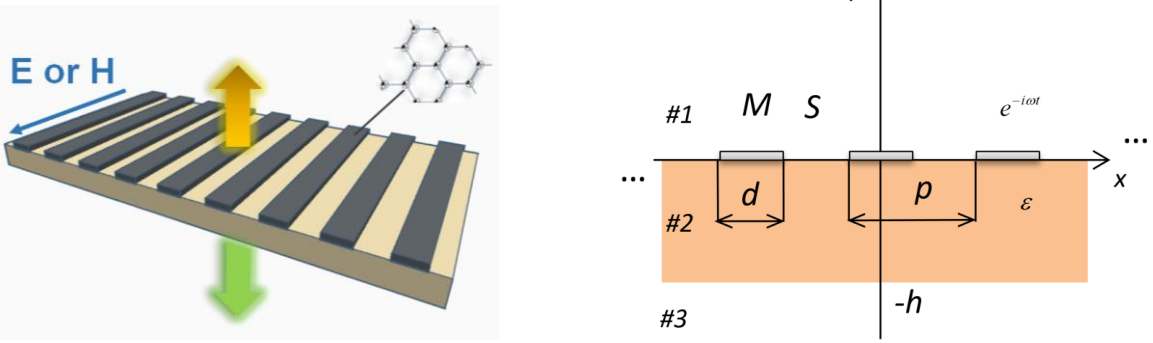

Figure 4.1. Cross-sectional view of laser built on infinite flat graphene strip grating lying on gain-material substrate, and notations used.

it has to satisfy (I) 2-D Helmholtz equation at $y \neq 0, -h$, with real free-space wavenumber off the substrate, $k_0 = \omega / c = 2\pi / \lambda$, and complex material wavenumber, $k = k_0(\alpha - i\gamma)$, where $\alpha, \gamma > 0$, inside the substrate, (II) resistive conditions at the strips, $\vec{r} \in M : \{y = 0; |\, x + np \,| < d / 2; n = 0, \pm 1, ..\}$:

- in the case of the H-polarization,

$$E_x^{(1)} + E_x^{(2)} = 2ZZ_0\left[H^{(1)} - H^{(2)}\right],\ E_x^{(1)} - E_x^{(2)}, \tag{4.1a}$$

- in the case of the E-polarization,

$$E_z^{(1)} + E_z^{(2)} = 2ZZ_0\left[H_x^{(1)} - H_x^{(2)}\right],\quad E_z^{(1)} = E_z^{(2)}, \tag{4.1b}$$

where Z is the complex-valued frequency-dependent graphene surface impedance, see (1.15), normalized by the free space impedance, $Z_0 = \sqrt{\mu_0 / \varepsilon_0}$. Besides, the tangential field components, H_z and E_x in the H-polarization and E_z and H_x in the E-polarization, have to be continuous across the slots, i.e. at $\vec{r} \in S : \{y = 0; -\infty < x < +\infty\} \setminus M$ and at the whole lower interface, $y = -h$, $-\infty < x < +\infty$. Finally, the function H or E has to satisfy (III) the radiation condition, and (IV) the condition of local finiteness of power. Note that this boundary-value problem is the same as the scattering problem of section 3.2, except the absence of the incident field and the presence of gain, γ. Besides, it is assumed, by default, that there is no phase shift between the periods/

4.2 Reducing eigenvalue problems to determinantal equations

4.2.1 H-polarization case

In this case, to find the mode-specific LEP eigenvalue pairs (frequency *f* and gain index γ), we follow Chapters 2 and 3, i.e. introduce Floquet series (2.8)-(2.10) for the magnetic field *H*, use the boundary conditions (4.1) and others, and reduce the electromagnetic field boundary-value problem to a DSE for the complex amplitudes of the field Floquet harmonics,

$$\begin{cases} \sum\limits_{n=-\infty}^{\infty} x_n |n| e^{in\phi} = \sum\limits_{n=-\infty}^{\infty} x_n \Delta_n e^{in\phi}, \; \theta < |\phi| \le \pi, \\ \sum\limits_{n=-\infty}^{\infty} x_n e^{in\phi} = 0, \quad |\phi| < \theta, \end{cases} \tag{4.2}$$

where $\theta = d / p$,

$$\Delta_n^H = |n| + i(1+\varepsilon)\left(\Gamma_n^H + \kappa Z\right), \tag{4.3}$$

$$\Gamma_n^H = \left[\frac{1}{g_n} - \frac{\varepsilon}{g_n^{sl}} \frac{\left(g_n^{sl} - g_n\varepsilon\right)e^{2ig_n^{sl}\xi} + \left(g_n^{sl} + g_n\varepsilon\right)}{\left(g_n^{sl} - g_n\varepsilon\right)e^{2ig_n^{sl}\xi} - \left(g_n^{sl} + g_n\varepsilon\right)} \right]^{-1}, \tag{4.4}$$

and all notations are the same as in (2.7), (2.11), (2.22) - see Chapter 2, except that now we use g_n instead of γ_n. The left-hand part of (4.2) does not depend on the frequency; it forms RHP on the unit circle, solution of which is known.

Thus, we perform analytical regularization of (4.2), based on the inversion of its left-hand part and arrive at the matrix equation (3.21). Details of this procedure, which makes use of the edge condition, can be found in [39]; see also Chapter 2.

As the considered configuration has the line of symmetry, which is the *y*-axis, we can split equation (3.21) into separate *x*-even and *x*-odd mode equations using the combinations, $x_m^{\pm} = x_m \pm x_{-m}$. This procedure yields two infinite equations,

$$x_m^{\pm} + \sum_{n=0(1)}^{+\infty} A_{m,n}^{\pm H} x_n^{\pm} = 0, \quad m = 0(1), \ldots \tag{4.5}$$

$$A_{m,n}^{\pm H} = \xi_n \Delta_n^H (k, \gamma; \varepsilon, p, h, \mu_c, \tau)\left[T_{mn}(\theta) \pm T_{-mn}(\theta)\right], \tag{4.6}$$

where $T_{mn}(\theta)$ are combinations of the Legendre polynomials of the argument $-\cos\theta$ – see Section 1.3 and $\xi_n = 1/2$ if n = 0 or 1 otherwise.

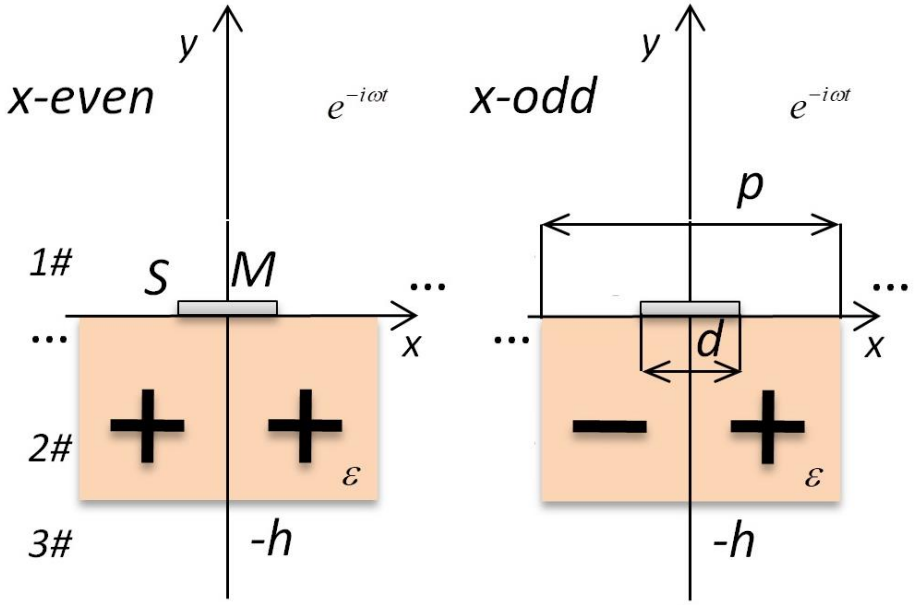

Figure 4.2. Representation of symmetry classes of the considered problem

Each of equations (4.5) is a Fredholm second kind operator equation. Therefore, its determinant exists as a function of all geometrical and material parameters of the problem. Then, due to the Fredholm theorems for operator-functions, characteristic numbers of (4.5) are discrete on the plane (k,γ) and each depends continuously on the problem parameters [117].

Moreover, Fredholm theorems guarantee that the characteristic numbers, found from the truncated determinantal equation for the *x*-even and *x*-odd modes, respectively,

$$D_H^{\pm}(k,\gamma) = Det\left\|\delta_{mn} + \xi_n \Delta_n^H (T_{mn} \pm T_{-m,n})\right\|_{m,n=0(1)}^{N} = 0 \qquad (4.7)$$

converge to the exact values with larger truncation numbers N [118].

Verification of the Fredholm property of the matrix equation is done analytically, using the large-index expressions and estimations for the functions, involved into the matrix elements (4.6).

4.2.2 E-polarization case

Here, to find the LEP eigenvalues, we use the series expansions for *E*, and reduce the EM problem to DSE for the Floquet-harmonic amplitudes, a_n, $n = 0, \pm1, \ldots$ similar to (3.20). On introducing new unknowns, $A_n = \delta_{0n}(1 - 2\kappa \sin\alpha / \Gamma_0) + a_n$, and notations,

$$\Gamma_n^E = g_n - g_n^{sl} \frac{\left(g_n^{sl} - g_n\right)e^{ig_n^{sl}\xi} - \left(g_n^{sl} + g_n\right)e^{-ig_n^{sl}\xi}}{\left(g_n^{sl} - g_n\right)e^{ig_n^{sl}\xi} + \left(g_n^{sl} + g_n\right)e^{-ig_n^{sl}\xi}}, \tag{4.8}$$

we cast the DSE to the following form:

$$\sum_{n=-\infty}^{\infty} A_n \Gamma_n^E e^{in\phi} = \begin{cases} 0, & \theta < |\phi| < \pi \\ -\dfrac{\kappa}{Z} \displaystyle\sum_{n=-\infty}^{\infty} A_n e^{in\phi}, & |\phi| < \theta \end{cases} \tag{4.9}$$

The left-hand part of (4.9) can be inverted analytically using the IDFT and the orthogonality of the exponents as it is done in Chapter 3, thus yielding a matrix equation for A_n. However, the rate of decay of the obtained matrix elements with larger |*m*| and |*n*| is different. To balance it, we use new variables, $x_n = A_n w_n$, $w_n = (|n|+1)^{1/2}$, split the infinite matrix equation into *x*-even and *x*-odd equations, and finally arrive at the following result:

$$x_m^{\pm} + \sum_{n=0(1)}^{\infty} A_{mn}^{\pm E} x_n^{\pm} = 0, \quad m = 0(1), \ldots, \tag{4.10}$$

where

$$A_{m,n}^{\pm E} = \kappa \xi_n w_m \left(Z w_n \Gamma_m^E\right)^{-1} \left[S_{mn}(\theta) \pm S_{-m,n}(\theta)\right], \tag{4.11}$$

and $S_m(\theta)$ are given by (3.28). Verification of the large-index behavior of the matrix elements $A_{m,n}^{\pm E}$ enables us to state that each of equations (4.10) is a Fredholm second kind matrix equation in the space of sequences l_2. Therefore, the Fredholm theorems guarantee that the characteristic numbers, found from the truncated determinantal equations for the *x*-even and *x*-odd modes, respectively,

$$D_E^{\pm}(k,\gamma) = Det\left\| \delta_{mn} + \kappa \xi_n w_m \left(Z w_n \Gamma_m^E\right)^{-1} \left(S_{mn} \pm S_{-m,n}\right) \right\|_{m,n=0(1)}^{N} = 0 \tag{4.13}$$

converge to the exact values with larger truncation numbers N. These values, or eigenpairs, (k_s, γ_s), form discrete set.

4.3 Results of numerical study of mode threshold conditions

4.3.1 H-polarized laser modes

The roots of determinantal equations like (4.7) are usually sought for using various iterative-search algorithms. Here, initial-guess values for (k, γ) can be taken from at least two different data.

First, the scattering problem solution (with γ = 0) can be used following section 3.3. In Fig. 4.3 (a), presented are the curves of the reflectance, transmittance and absorbance for the parameters explained in the caption and the frequency, $f = kc / 2\pi$, varying from zero to 6 THz.

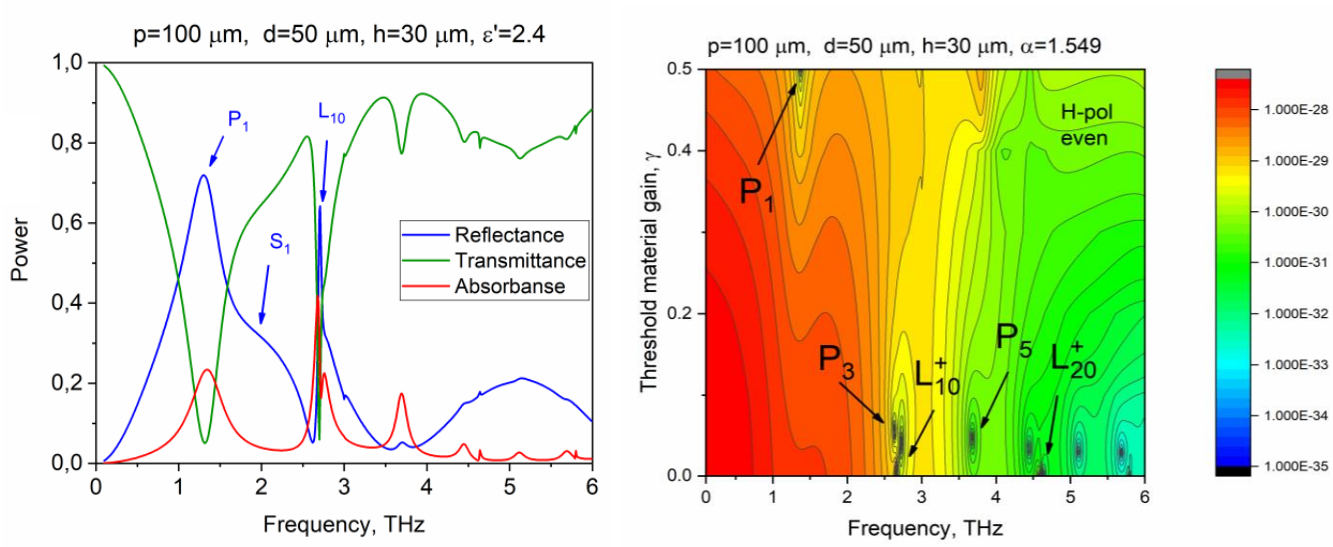

(a) (b)

Figure 4.3. Spectra of the reflectance, transmittance and absorbance of the infinite flat graphene-strip grating lying on passive dielectric substrate, for the normally incident H-polarized plane wave (a) and color map of the x-even LEP determinant absolute value for the similar plasmonic laser configuration with the gain substrate (b). The matrix truncation number is N = 50. Graphene parameters are T = 300 K, τ = 1 ps, and chemical potential μ_c = 0.5 eV.

Following section 3.5.1, we mark the resonances, which correspond to the SMs, PMs, and LMs, as S_n^+, P_n and $L_{n,m}^+$, respectively. Then, in the LEP analysis, the initial guesses can be taken as the peak reflectance frequencies and arbitrary small numbers for the thresholds.

Second, a map of either of the determinant absolute values (4.7) can be built on the plane (f,γ), to visualize the minima and take them as initial guess.

In Fig. 4.3 (b), presented is a color map of the even-mode determinant of (4.7) for the same parameters as in Fig. 4.3 (a). The minima on the map correspond to the LEP eigenvalues. It is well visible that the frequencies of reflectance peaks and the mode frequencies as in good agreement. Additional advantage of building a map of determinant is that, for each mode, one can determine approximate value of the mode threshold and further use it as initial guess in the iterative search algorithm. Therefore, in our systematic analysis we have used the latter approach to initial-guess selection.

As a search algorithm, we used the residual inverse iteration technique (RIIT), details of which can be found in [119,120], although a standard steepest-descent algorithm of Matlab library could be also used. The advantage of RIIT is that it finds the eigenvector together the eigenvalue.

In Fig. 4.4 we show color maps of determinants (4.7), for the *x*-even (a) and *x*-odd (b) modes computed with N = 50, on the plane (f,γ). Note that the values of the "background" on this map start growing at the larger frequencies.

Here, the grating period, the strip width and the substrate thickness are in the micrometer range, p = 70 μm, d = 14 μm, h = 10 μm and α = 1.5.

As explained, the minima on the maps correspond to the LEP eigenvalues, which we will call, for brevity, the modes. The chosen parameters place the lowest natural mode frequencies, for all mode types, to the THz range - on each map, in the frequency range from statics to 10 THz there are over ten modes with rather different thresholds, γ, from around 1 to 10^{-3}. More exact values, refined with the aid of RIIT algorithm., are presented in Table 4.1.

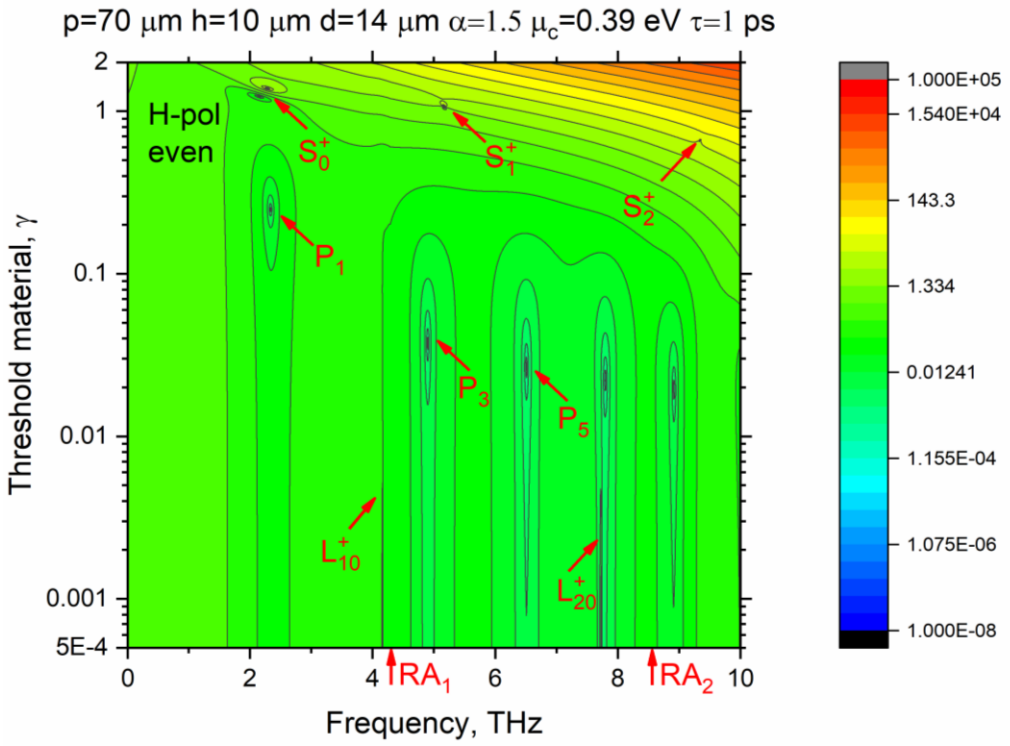

(a)

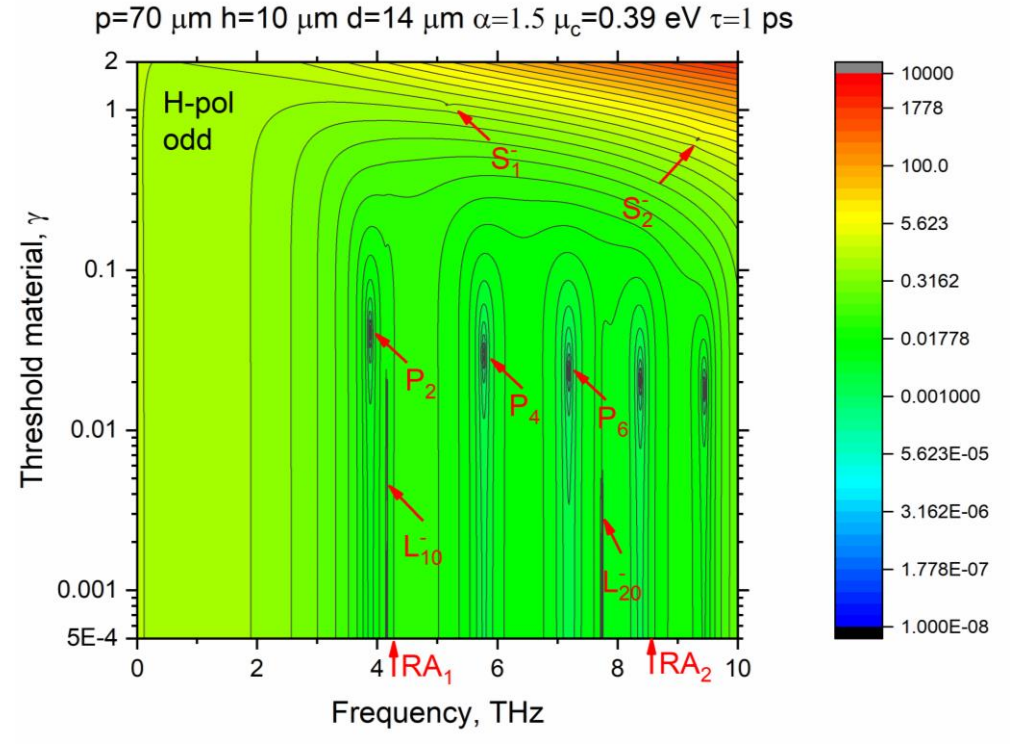

(b)

Figure 4.4. Color maps of the LEP determinants (absolute value) for the x-even (a) and *x*-odd (b) modes of the laser from Fig. 4.1. The matrix truncation number is N = 50. The grating and substrate parameters are indicated above the map. Graphene parameters are T = 300 K, τ = 1 ps, and μ_c = 0.39 eV.

Table 1. Eigenpairs for the LEP in the case of the H-polarization

$p = 70\ \mu\text{m}, h = 10\ \mu\text{m}, d = 14\ \mu\text{m}, \alpha = 1.5, \mu_c = 0.39\ \text{eV}, \tau = 1\ \text{ps}$			
Mode	Frequency, THz	Threshold gain, γ	Q-factor
P_1	2.501655	0.152062	9.86
P_2	3.881121	0.040944	36.6
L_{10}^{+}	4.165693	0.00424	353.7
L_{10}^{-}	4.162835	0.003903	384.3
S_0	2.153888	1.231526	1.137
S_1^{+}	5.176666	1.04789	1.441
S_1^{-}	5.158333	1.083	1.385

The Q-factors are computed using the formula $Q = \alpha / \gamma + O(\gamma)$, derived in [82], taking into account that the overlap coefficient here equals 1.

As we can see, there is one very high-threshold *x*-even mode at around 2.2 THz – this is the lowest SM, S_0, and two others on each map around 5.5 THz and 9.5 THz, which are $S_1^{\pm}$ and $S_2^{\pm}$, which are slightly perturbed by the presence of strips and have very large radiation losses.

Further, on each map there is a sequence of modes, which have by order or more lower thresholds and follow a hyperbola, $f \cdot \gamma = \text{const}$. These eigenvalues correspond to the PMs of graphene strips. Indeed, following the derivation of analytical formulas (3.29) and (3.29) in section 3, however, adapting it to the case of LEP eigenvalues, we obtain the PM frequencies and associated threshold gain values as

$$f_m^P \approx \frac{1}{2\pi}\sqrt{\frac{\pi(m-0.25)\Omega c}{(\alpha^2+1)\,d}}, \quad \gamma_m^P \approx \frac{1}{2\alpha\tau}\sqrt{\frac{(\alpha^2+1)^3 d}{\pi(m-0.25)\Omega c}}, \tag{4.14}$$

where $m = 1,2, \ldots$ is the mode index and Ω is given in (1.17).

As one can see, the plasmon frequencies grow and their thresholds drop as a $\sqrt{m\Omega c / d}$, so that indeed $f_m^P \cdot \gamma_m^P = (\alpha^2+1)(4\pi\alpha\tau)^{-1}$. Note that (4.14) are derived

neglecting the interband contribution to the graphene conductivity. Therefore, these expressions are not valid at the very high frequencies (lying in the visible range [87]) where the interband conductivity cannot be neglected. Besides, in (4.14) the radiation losses of the plasmon modes are neglected in favor of the losses in graphene.

The plasmons of the odd indices belong to the class of *x*-even modes, and those of the even indices – to the class of *x*-odd modes, appearing only on one of the maps.

The near-field patterns shown in Fig. 4.5 have been computed for $N = 50$ and the same graphene and configuration parameters as in Fig. 4.4. They support our identification of the plasmon modes.

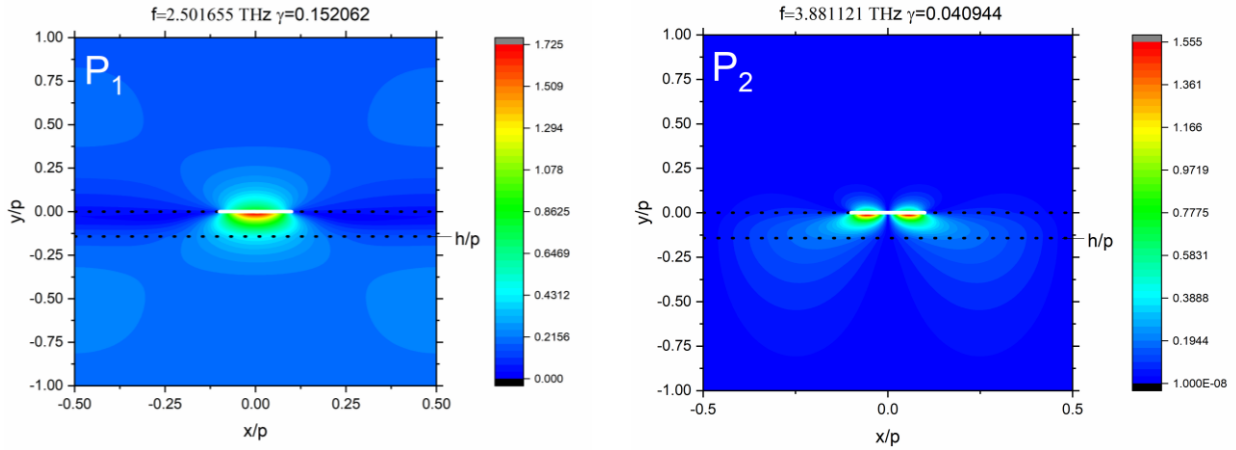

(a) (b)

Figure 4.5. Magnetic field patterns on three periods for the PMs of graphene strips, *x*-even P_1 and *x*-odd P_2, for the same grating as in Fig. 4.4.

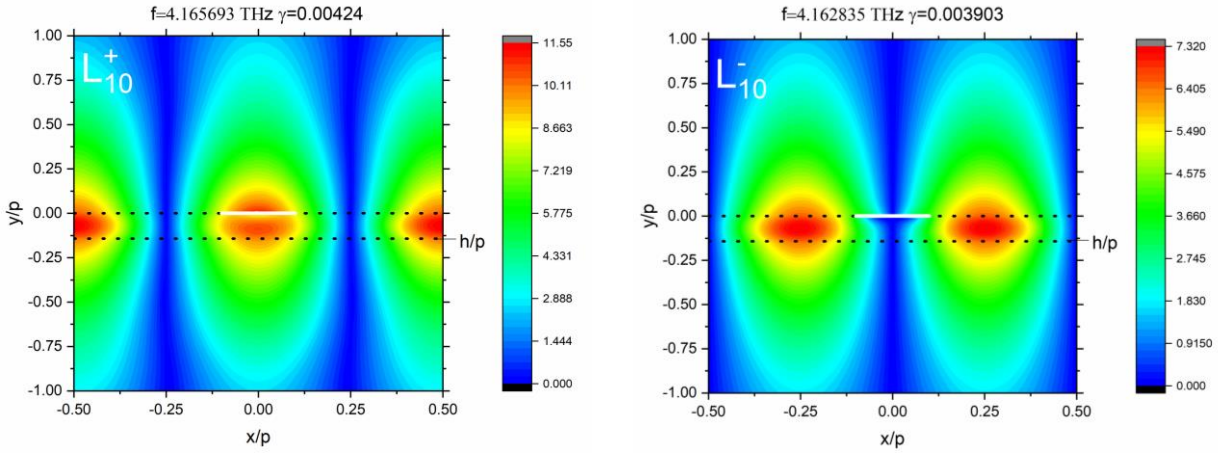

(a) (b)

Figure 4.6. Magnetic field patterns on three periods for the *x*-even LM L_{10}^{+} (a) and *x*-odd LM L_{10}^{-} (b) for the same grating as in Fig. 4.4.

Still besides, there are two very low-threshold minima on each map of Fig. 4.4, at 4.16 THz and 7.7 THz, which correspond to the LMs of the whole grating as a periodic open cavity, $L_{10}^{\pm}$ and $L_{20}^{\pm}$, respectively. These frequencies are red-shifted from the 1-st order RA, which sits at 4.28 THz. The near fields, shown in Fig. 4.6, correspond to L_{10}^{+} and L_{10}^{-}, respectively, and have been computed with $N = 50$.

Note that the lattice-mode fields are drastically different from the plasmon-mode fields. They form the standing waves along the whole grating with the number of hot spots per period being twice the index of the RA, which is "parent" for the LM. In Fig. 4.6, we have the modes $L_{10}^{\pm}$ (i.e. $m = 1$), so their fields have 2 very similar bright spots on the period. The difference is in the spot location – they are at the strip and the slot, for the *x*-even mode, and shifted by a quarter of period, for the *x*-odd mode.

In Fig. 4.7, we present the color maps of two determinants (absolute value) (4.13) for the laser with much smaller unit-cell dimensions, $p = 3$ μm, $d = 35$ nm, $h = 1$ μm, however, larger refractive index, $\alpha = 1.949$. Note that here the filling factor is very small, $d/p = 0.012$ (narrow strips). The band of the frequencies is from 60 THz to 250 THz, i.e. in the infrared range, and the wavelengths are from 5 μm to 1.2 μm.

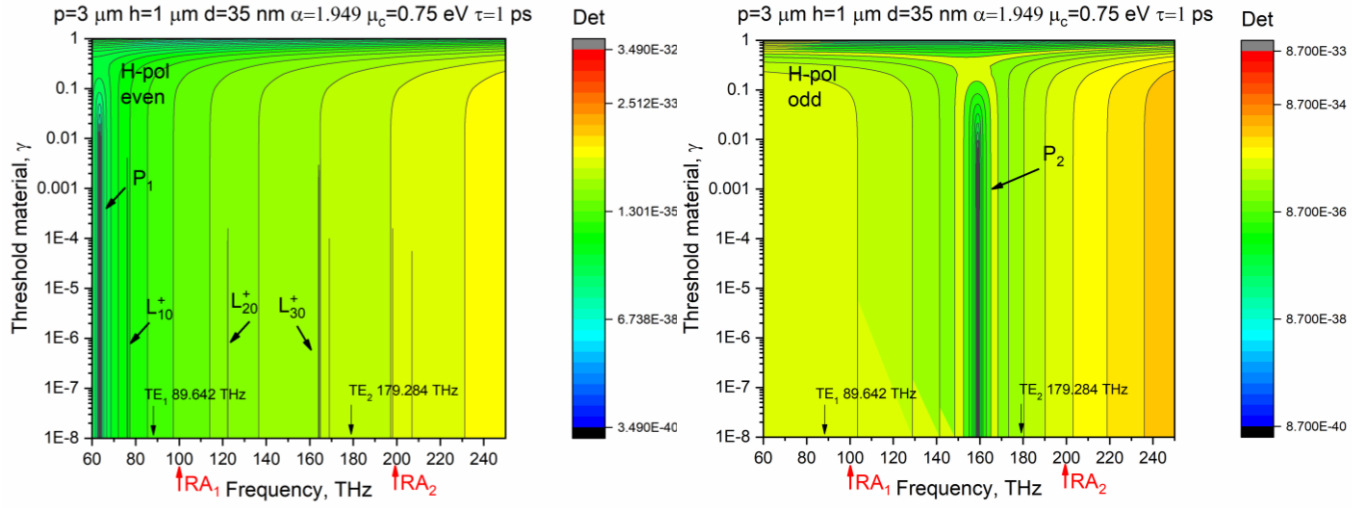

(a) (b)

Figure 4.7. Color maps of the LEP determinants (absolute value) for the *x*-even (a) and *x*-odd (b) modes of the laser from Fig. 4.1. The matrix truncation number is N = 50. Graphene parameters are T = 300 K, $\tau = 1$ ps, and $\mu_c = 0.39$ eV.

Comparing these maps with the previous case of Fig. 4.4, we see that now the determinant absolute values vary at ultra-small level, from 10^{-33} to 10^{-40} and it is quite difficult to see the minima, which correspond to the eigenvalues. This is, apparently, because of some 50 times higher frequencies of the PMs and LMs.

To overcome this difficulty, we started looking for the eigenvalues as the zeros of the other, real-valued quantity – matrix inverse condition number – see Fig. 4.8.

The condition number is defined as product of the matrix norm and its inverse norm, so the inverse condition number is

$$1/C = \left[Cond^{\pm}(k,\gamma) \right]^{-1} = \left\{ \left\| A^{\pm}_{m.n} \right\|^{N}_{m,n=0(1)} \times \left\| \left(A^{\pm}_{m.n} \right)^{-1} \right\|^{N}_{m,n=0(1)} \right\}^{-1} \qquad (4.14)$$

As a function of the frequency and threshold index, this quantity varies in much more moderate manner, see that color maps in Fig. 4.8. At the bottom edge, the red arrows mark the positions of the RAs, which are the branch points, and the black arrows mark the cut-off frequencies of the higher-order guided waves of the substrate.

On these maps, one can see the narrow valleys, which hide the mode eigenvalues of the same three families: high-threshold SMs, moderate-threshold PMs, and ultralow-threshold LMs. Their frequencies and threshold values of gain index. found by RIIT, are presented in Table 4.2. They demonstrate that the *x*-odd lattice modes have the thresholds several orders lower than their sister modes of the *x*-even class. Some of the modes have extremely low thresholds – for instance, for the L^{+}_{30} mode it has the order of 10^{-8}, and for the mode L^{-}_{30} it is at the level of machine precision, 10^{-17}.

In Fig. 4.9, we show the magnetic field of the principal SM in the near zone. The strip is shown as white box and the dielectric-air boundaries are shown as black dotted lines Note that the magnetic field at the substrate middle section is almost zero, similar to the slab without strip where it is exactly zero. Very narrow strips of 35 nm (d/p = 0.0117) perturb this pattern, however, very gently.

In Fig. 4.10, we show the field patterns of the first two PMs, P_1 and P_2.

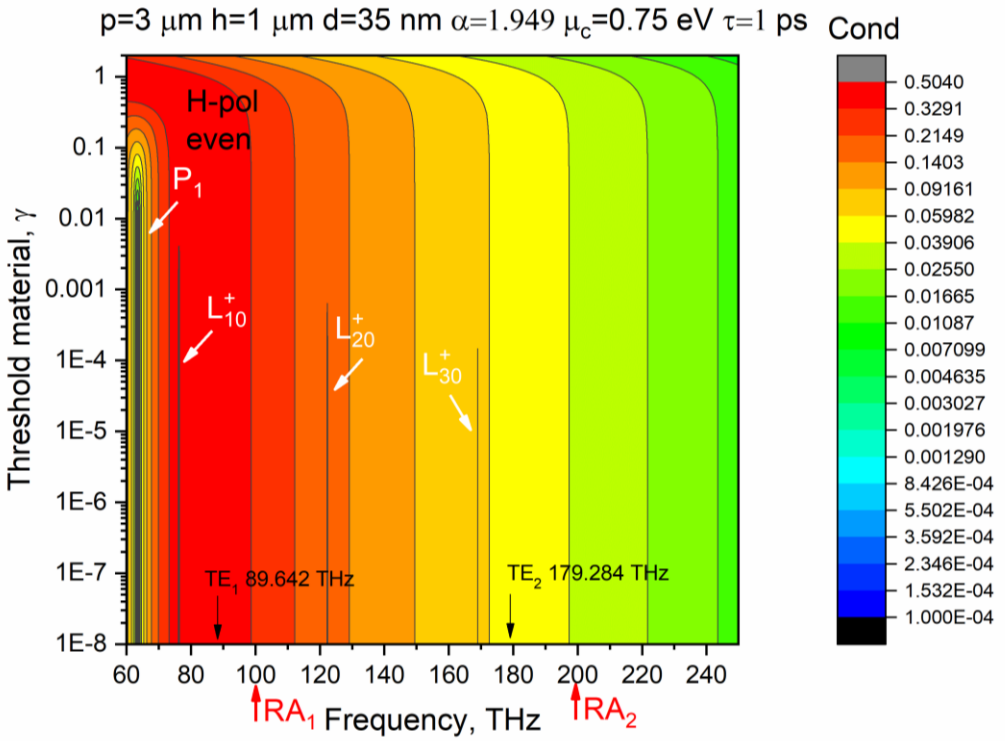

(a)

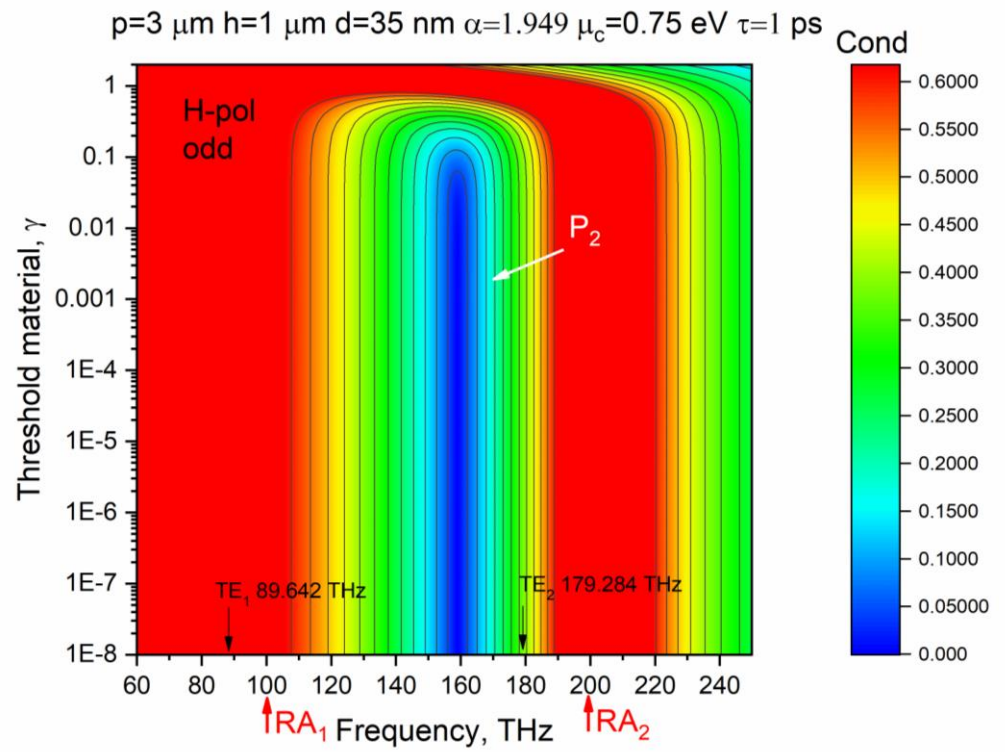

(b)

Figure 4.8 Color maps of the LEP inverse condition number for the *x*-even (a) and *x*-odd (b) modes of the same laser configuration as in Fig. 4.7. The matrix truncation number is N = 50.

Table 4.2. Eigenpairs for LEP in the case of the H-polarization

$p=3\,\mu\text{m}, h=1\,\mu\text{m}, d=35\text{ nm}, \alpha=1.949, \mu_c=0.75\text{ eV}, \tau=1\text{ ps}$			
Mode	Frequency, THz	Threshold gain, γ	Q-factor
P_1^+	63.428217	0.00425	458.67
P_2^-	159.055761	0.00192	1015.2
L_{10}^+	76.23657	$7.794*10^{-6}$	$2.50*10^{5}$
L_{10}^-	76.217061	$3.469*10^{-11}$	$5.62*10^{10}$
L_{20}^+	122.290800	$1.872*10^{-7}$	$1.04*10^{7}$
L_{20}^-	122.287012	$5.693*10^{-10}$	$3.42*10^{9}$
L_{30}^+	169.032243	$3.46183*10^{-8}$	$5.63*10^{7}$
L_{30}^-	169.031012	$5.262*10^{-17}$	$3.70*10^{16}$
S_0	13.05555	1.866	1.045

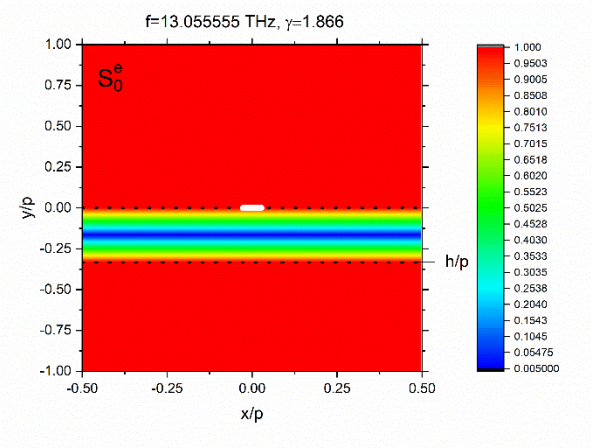

Figure 4.9 Magnetic field pattern on one period for the principal SM of substrate, S_0^+.

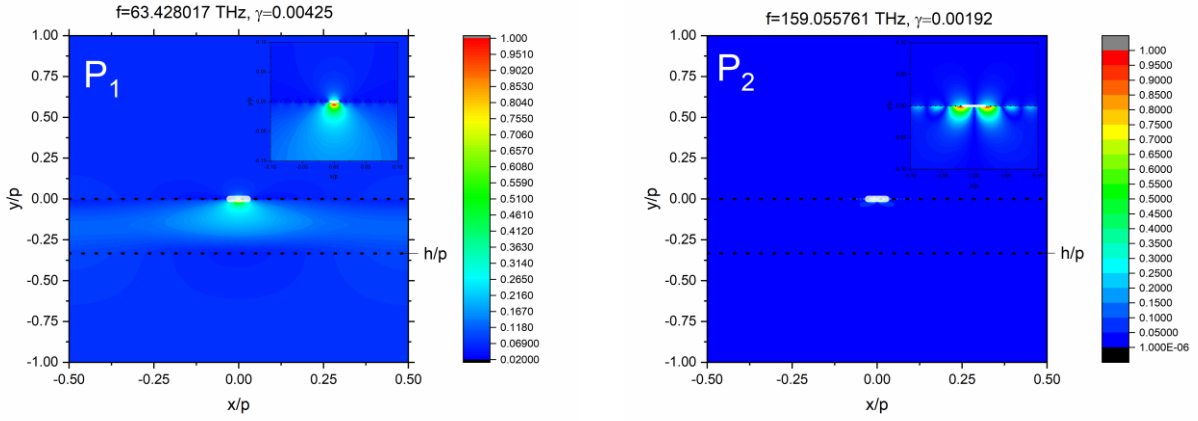

(a) (b)

Figure 4.10 Magnetic field patterns on one period for the *x*-even mode P_1 and *x*-odd P_2.

They display the fields, which are tightly bind to the strips, with the number of bright spots corresponding to the mode index, and *x*-even or *x*-odd symmetry.

In Fig. 4.10, we show the field patterns of the first three LMs, $L_{10}^{\pm}, L_{20}^{\pm}$ and $L_{30}^{\pm}$, created by the 1-st RA and the principal guided wave of the substrate, TM_0.

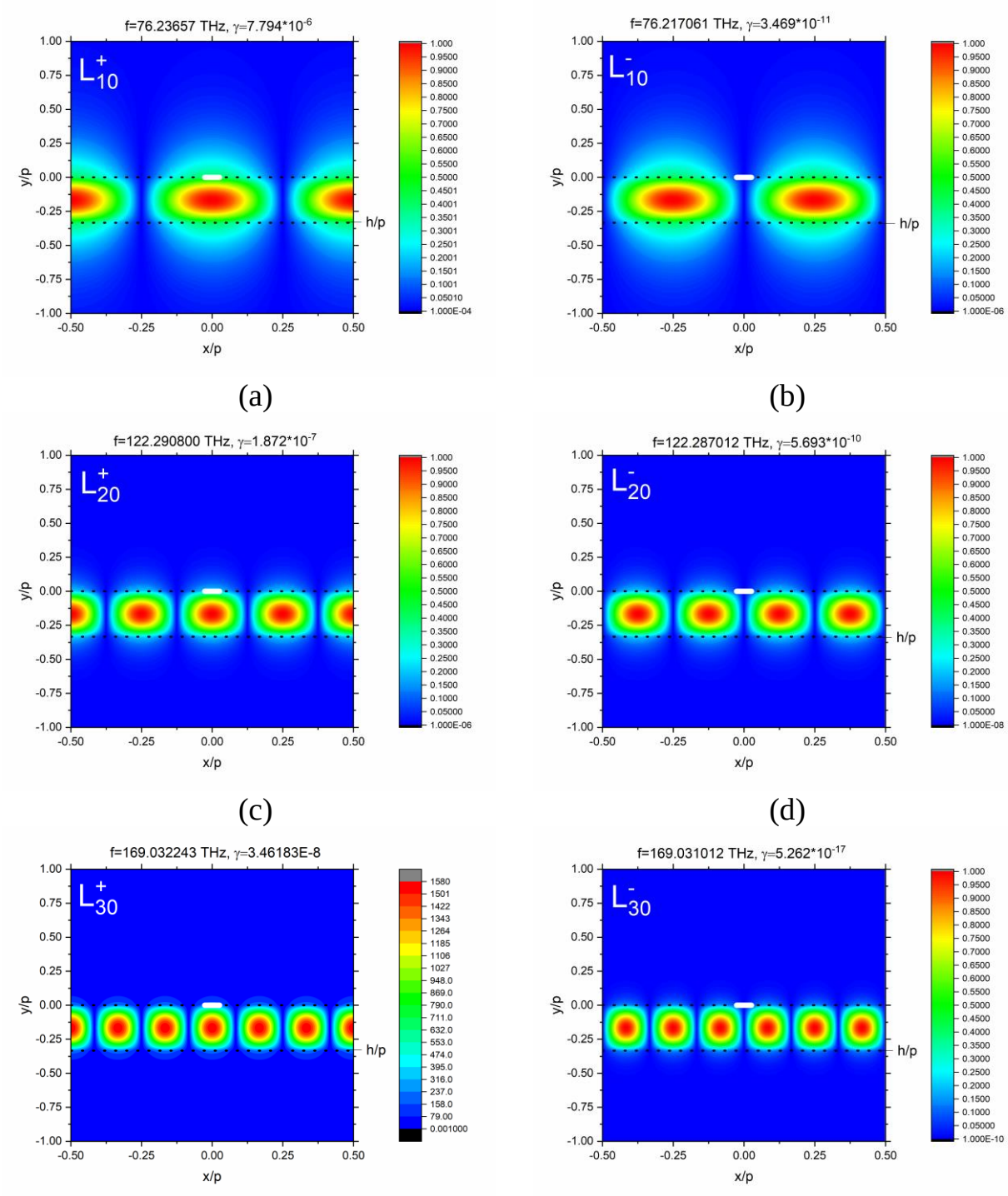

Figure 4.11. Magnetic field patterns on one period for the *x*-even (left column) and *x*-odd (right column) LMs $L_{10}^{\pm}, L_{20}^{\pm}$ and $L_{30}^{\pm}$ for the same grating as in Fig. 4.8 – 4.10.

4.3.2 E-polarized laser modes

In Fig. 4.12, presented are color maps on the plane (f,γ) of inverse condition numbers (4.14), computed for the E-polarization matrices (4.10) with N = 50.

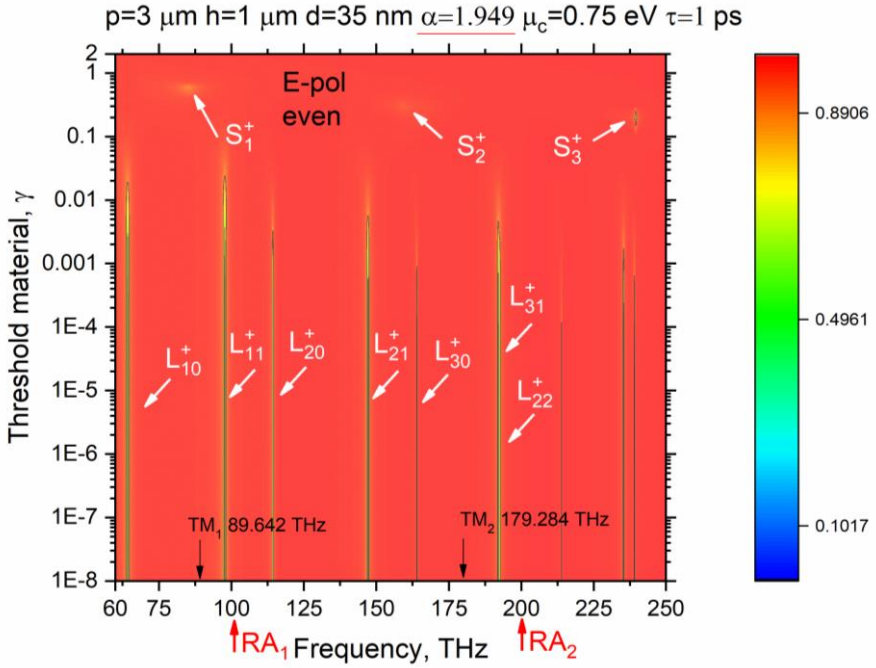

(a)

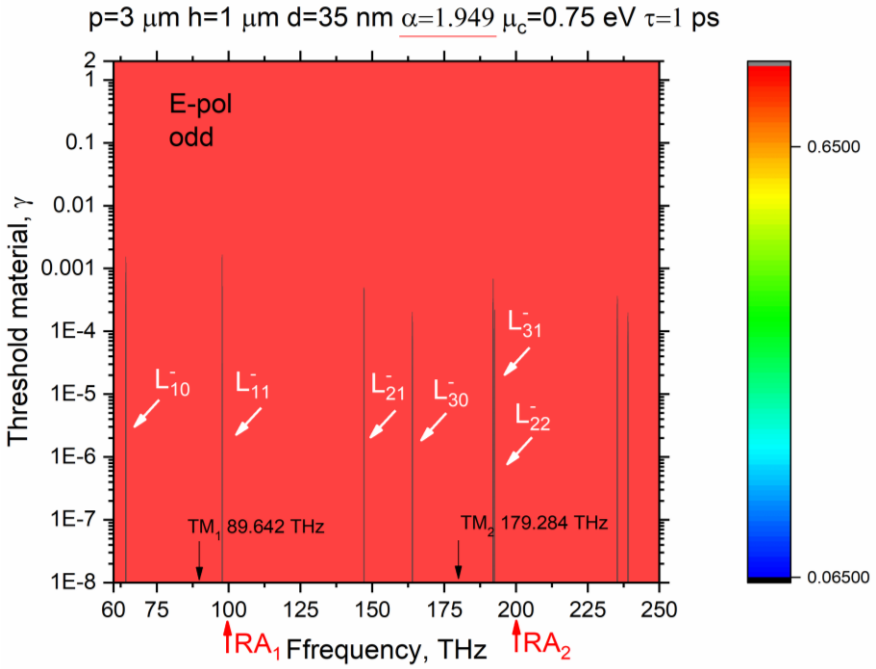

(b)

Figure 4.12. The color map of the LEP inverse condition umber for the *x*-even (a) and *x*-odd (b) E-polarized modes of the laser from Fig. 4.1, on the plane (f,γ). The matrix truncation number is N = 50. Graphene and grating parameters are T = 300 K, τ = 1 ps, μ_c = 0.39 eV, p = 3 μm, d = 1.5 μm, h = 1 μm, α = 1.949.

The minima on the map correspond to the LEP eigenvalues – i.e. the E-polarized modes of the considered laser model. They are taken as initial-guess values. More accurate values for the LEP eigenpairs, plus the corresponding Q-factors, are presented in Table 4.3 after the search using the RIIT algorithm.

Table 4.3. Eigenpairs for LEP in the case of the E-polarization

Mode	Frequency, THz	Threshold gain, γ	Q-factor
$p = 3\,\mu\text{m}, h = 1\,\mu\text{m}, d = 35\text{ nm}, \alpha = 1.949, \mu_c = 0.75\text{ eV}, \tau = 1\text{ ps}$			
L_{10}^{+}	64.317705	6.427*10^{-7}	3.03*10^{6}
L_{10}^{-}	64.311292	2.536*10^{-10}	7.68*10^{9}
L_{11}^{+}	97.785096	5.541*10^{-7}	3.51*10^{6}
L_{11}^{-}	97.778700	6.656*10^{-14}	2.92*10^{13}
L_{20}^{+}	114.347958	7.819*10^{-8}	2.49*10^{7}
L_{20}^{-}	114.345774	1.185*10^{-10}	1.64*10^{10}
L_{21}^{+}	147.153849	1.329*10^{-7}	1.46*10^{7}
L_{21}^{-}	147.149350	1.865*10^{-10}	1.05*10^{10}
L_{22}^{+}	192.111694	9.368*10^{-8}	2.08*10^{7}
L_{22}^{-}	192.108106	1.557*10^{-10}	1.25*10^{10}
L_{30}^{+}	163.995534	2.205*10^{-8}	8.84*10^{7}
L_{30}^{-}	163.994646	6.819*10^{-11}	2.86*10^{10}
L_{31}^{+}	192.638927	4.157*10^{-8}	4.69*10^{7}
L_{31}^{-}	192.636787	1.523*10^{-10}	1.28*10^{10}
S_0	13.155914	1.857	1.0497
S_1^{+}	85.41519	0.569	3.4259
S_2^{+}	159.29152	0.324	6.0165
S_3^{+}	239.513	0.198	9.8452

One can see several high-threshold eigenvalues – these are the lowest SMs, $S_{0,1,2}^{\pm}$, which have very large radiation losses and, hence, high thresholds. In the E-polarization, there are no plasmon modes. However, there are several ultralow-threshold minima on each map, which correspond to the LMs of the whole grating as a periodic

open cavity, of the *x*-even and *x*-odd classes. Note that their thresholds are 5-6 orders lower than those of the SMs.

In Figs. 4.13 to 4.16, we present the LM near E-field patterns computed with N = 50 and the same graphene and configuration parameters as in Fig. 4.12. Here, the graphene strips are marked as white straight boxes and the dielectric-air boundaries are shown as black dotted lines.

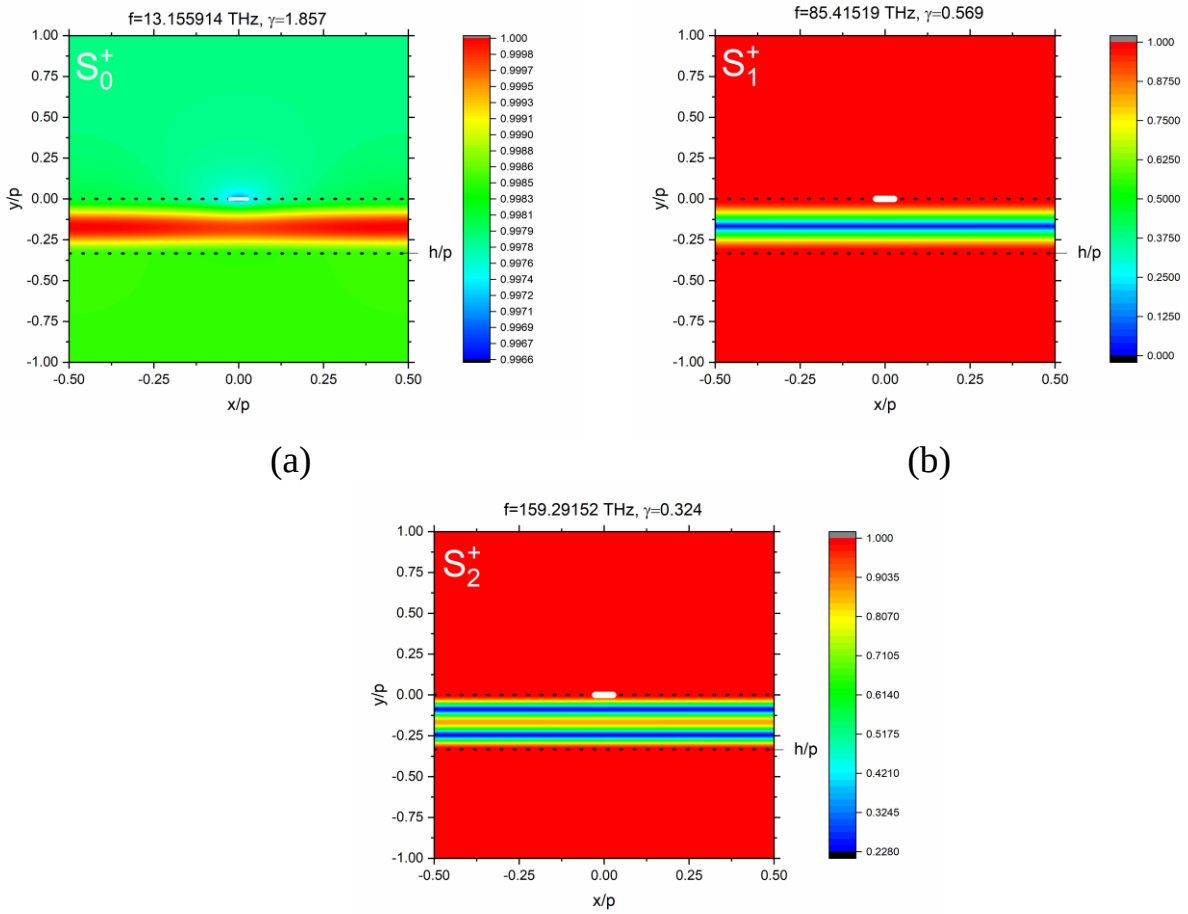

Figure 4.13. Electric field patterns the *x*-even modes S_0^+ (a), S_1^+ (b) and S_2^+ (c).

The patterns show integer number of bright field spots on elementary period ($2m$, along the *x*-axis) and across the substrate (M, along the *y*-axis). The first index corresponds to the "parent" RA number (and hence the resonating Floquet harmonic number) and the second index corresponds to the type of the "parent" natural wave, TE_M, (M = 0,1,2, …) guided by the substrate as an open waveguide. This explains our notations in the LMs identification, $L_{mM}^{\pm E}$.

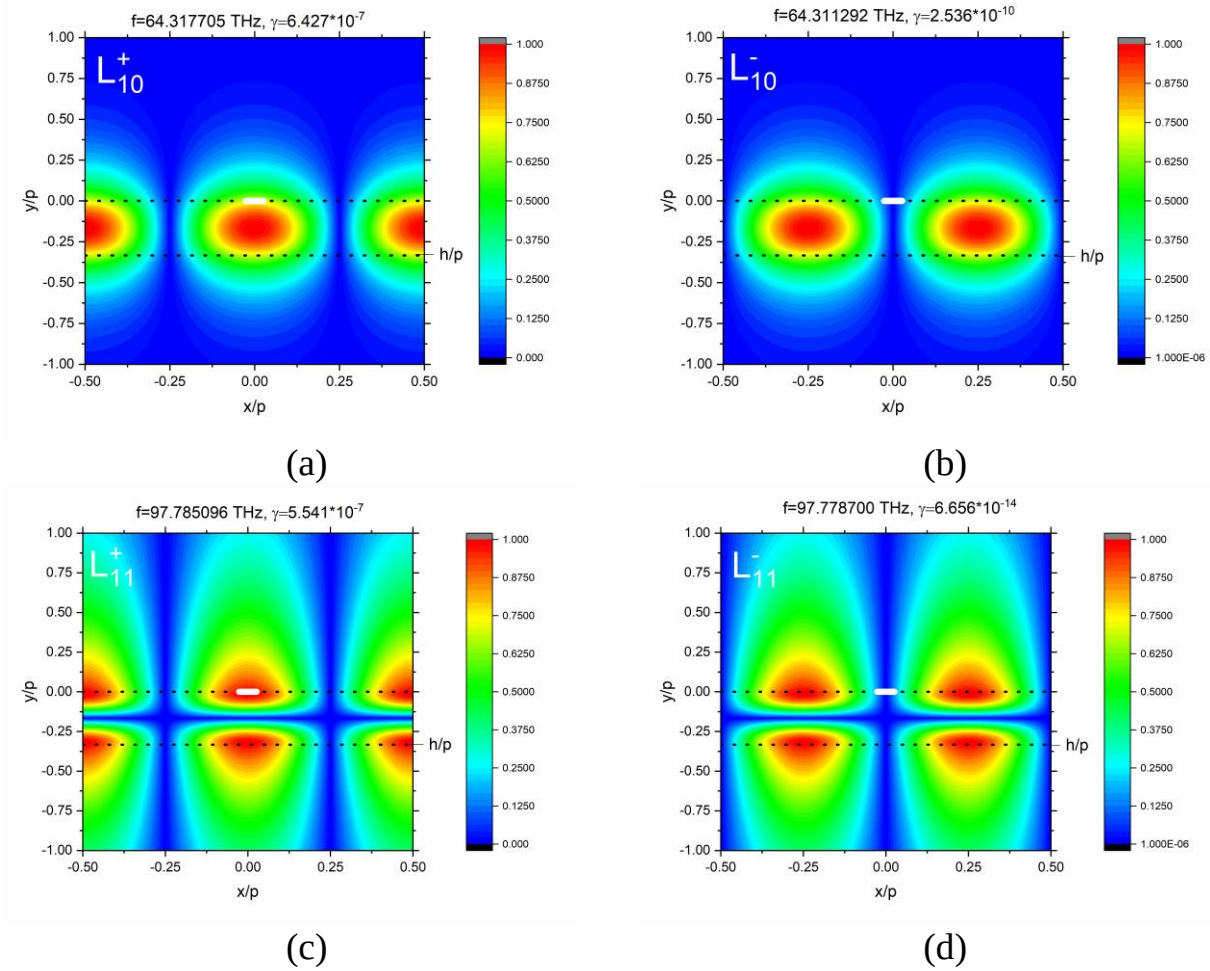

Figure 4.14 Electric field patterns the *x*-even (left column) and *x*-odd (right column) LMs, $L_{10}^{\pm}$ (top row) and $L_{11}^{\pm}$ (bottom row).

In Fig. 4. 14, presented are the near-field patterns of the LMs, created by the principal guided wave of the substrate, TM_0 (M = 0) and the first higher-order wave, TM_1 (M = 1), near the 1-st RA. The higher-order wave of the substrate is responsible for the zero field near the median section of the substrate. Note that the *x*-even and *x*-odd modes of each type have very similar fields, differing by the shift along the x-axis by the quarter of period. Their frequencies of emission are also very close to each other – for the $L_{10}^{\pm}$ modes they are 64.317705 THz and 64.311292 THz, and for the $L_{11}^{\pm}$ modes, they are 97.785096 THz and 97.778700 THz, respectively. However, the threshold gain values are drastically different, for the $L_{10}^{\pm}$ modes they are 10^{-7} and 10^{-10}, and for the $L_{11}^{\pm}$ modes, they are 10^{-7} and 10^{-14}, respectively. This is because for the *x*-even modes the lossy strips are in the E-field maxima, while for the *x*-odd they are in the minima.

In Fig. 4.15, we show the near field patters for LMs, created by the 2-nd RA and three guided waves of the substrate, TM_M with M = 0, 1 and 2, i.e. $L_{20}^{\pm}, L_{21}^{\pm}$ and $L_{22}^{\pm}$.

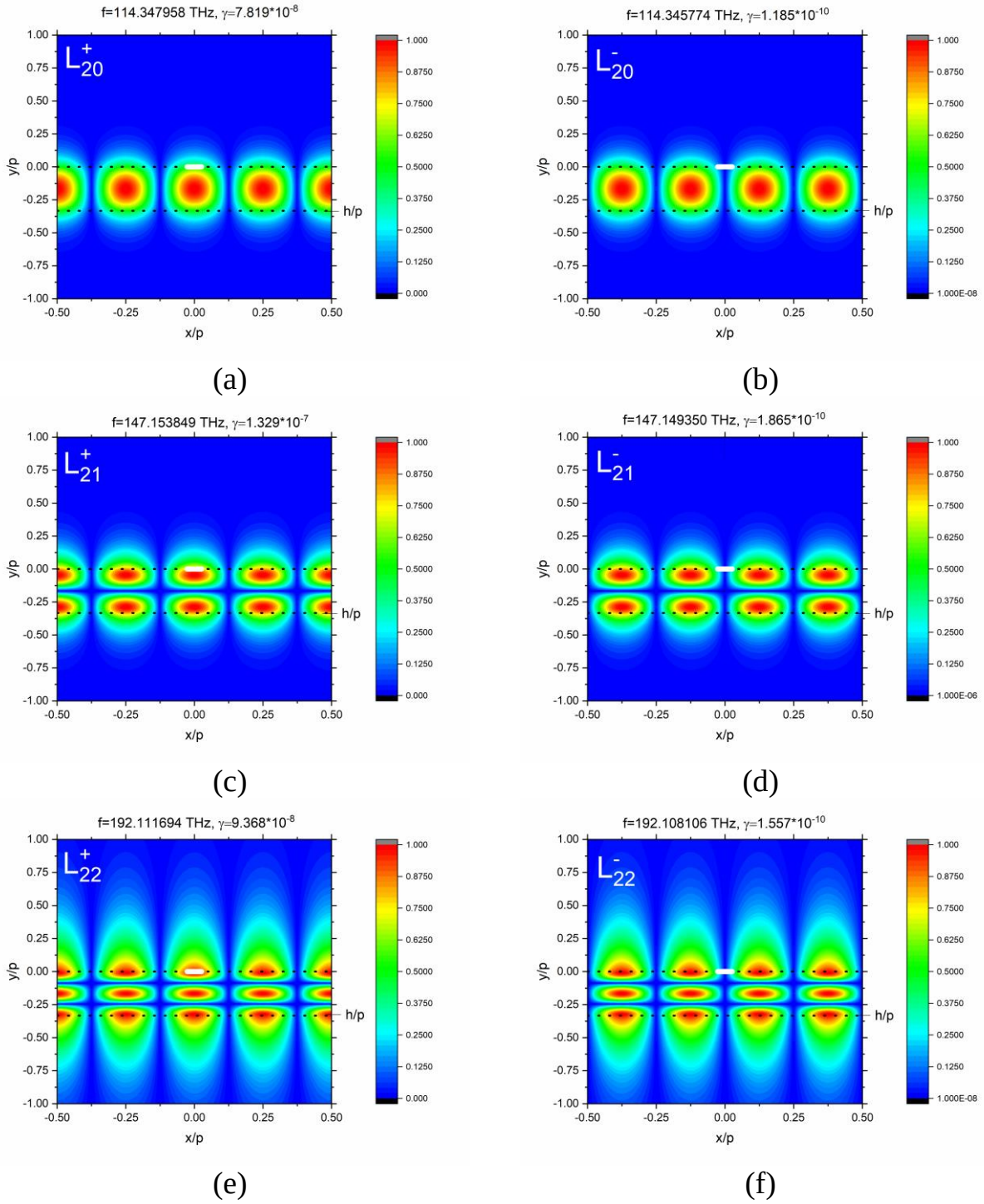

Figure 4.15. E-field patterns of the *x*-even (left) and *x*-odd (right) LMs $L_{20}^{\pm}, L_{21}^{\pm}, L_{22}^{\pm}$.

They show the same regularities: the fields (besides of the $p/8$ shift) and the frequencies of the sister modes of each even-odd doublet are very close to each other, while the gain thresholds are drastically different – 10^{-8} and 10^{-11}, respectively.

Further, in Fig. 4.16, we present the near-field patterns for the even-odd doublets of the modes, created by the 3-rd RA and two guided waves of the substrate, TM_M with M = 0, 1, i.e. $L_{30}^{\pm}$ and $L_{31}^{\pm}$. They display the same regularities as explained above.

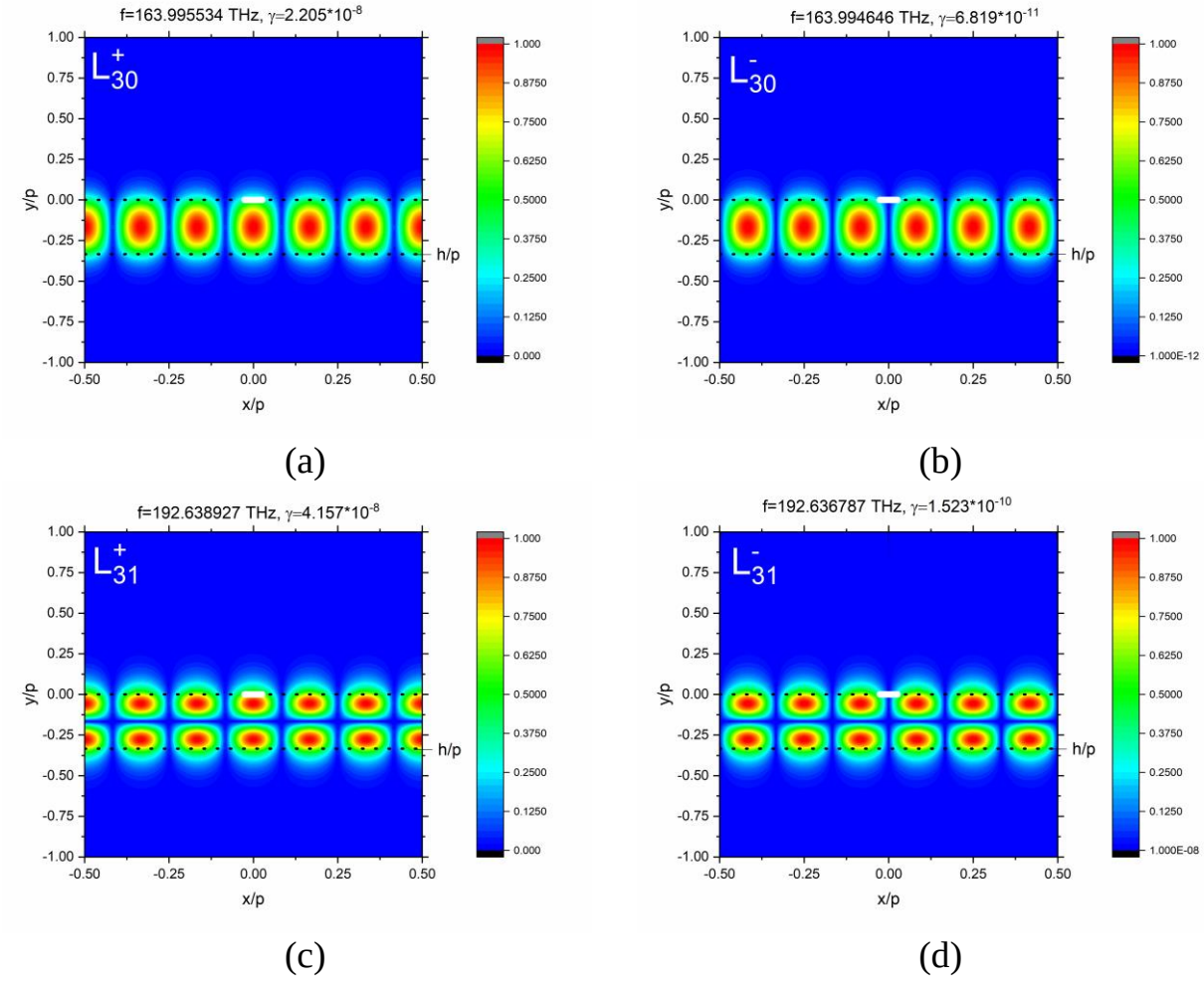

Figure 4.16. E-field patterns of the *x*-even (left) and *x*-odd (right) LMs $L_{20}^{\pm}, L_{31}^{\pm}$.

Finally, we present the results of the computation of the $L_{11}^{\pm}$ frequencies and thresholds as a function of the squared substrate refractive index, α^2 – see Fig. 4.17 and Fig. 4.18 for the x-even and x-odd LM, respectively, and for three values of the substrate thickness.

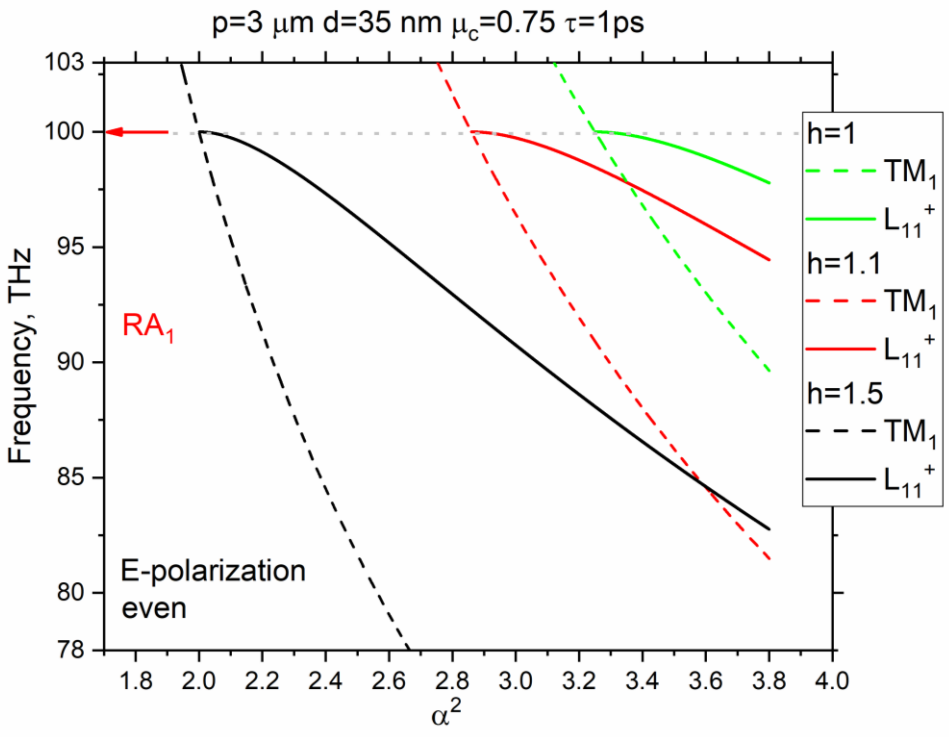

(a)

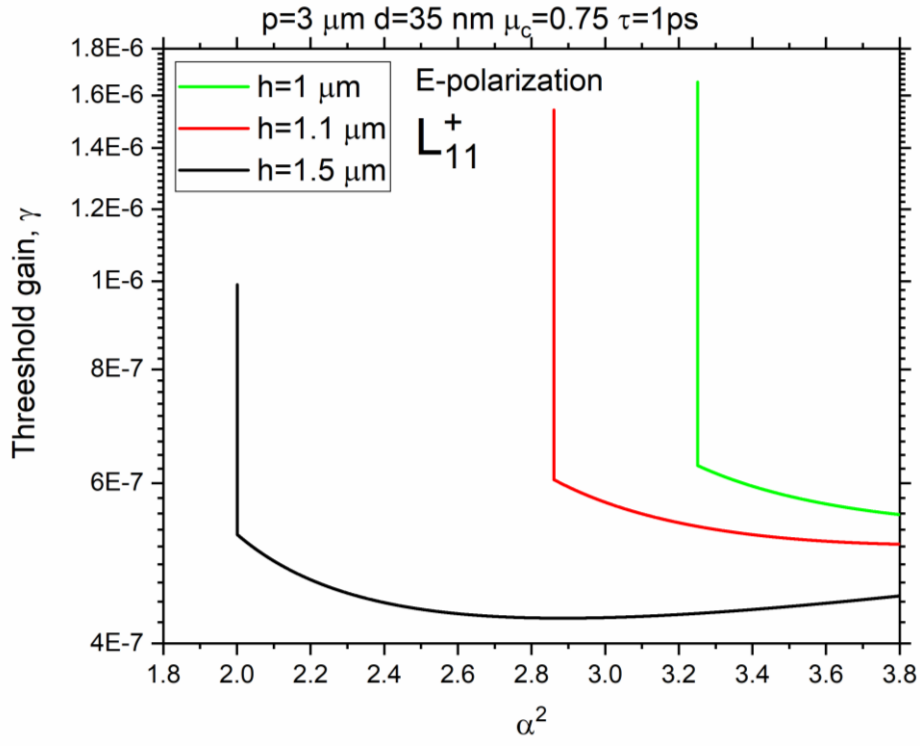

(b)

Figure 4.17. Dependences of the *x*-even LM frequency (a) and threshold gain (b) on the refractive index of the active substrate for three thickness values. Other parameters are as marked. On panel (a), dashed lines show the substrate waves cut-off frequencies and the dotted straight line marks the RA frequency.

Here, the horizontal dotted line at 100 THz marks the 1-st RA (the branch point).

The dashed lines mark the variation of the cut-off frequency of the 1-st higher-order guided wave of the substrate, TM_1.

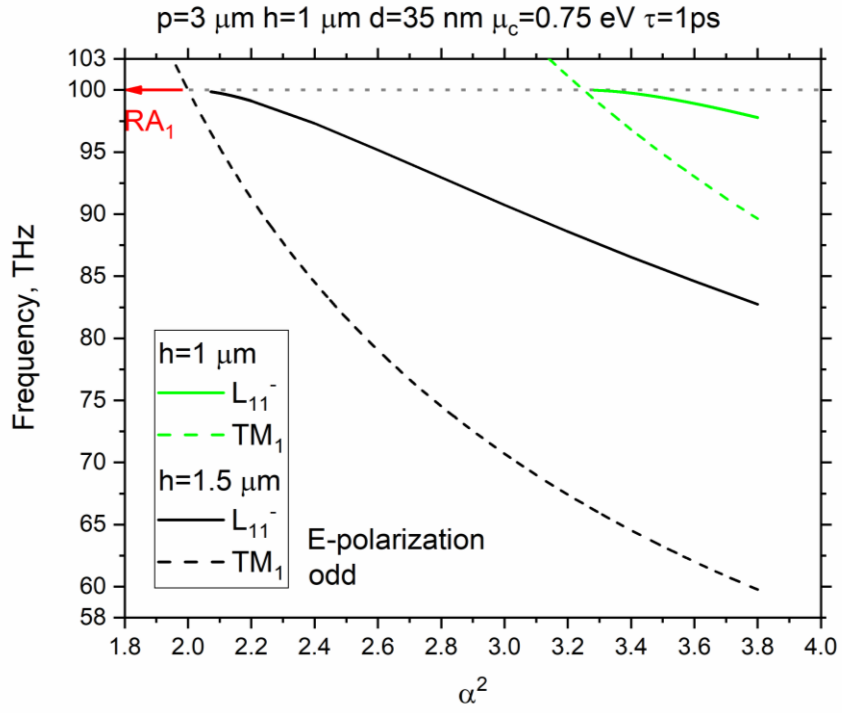

(a)

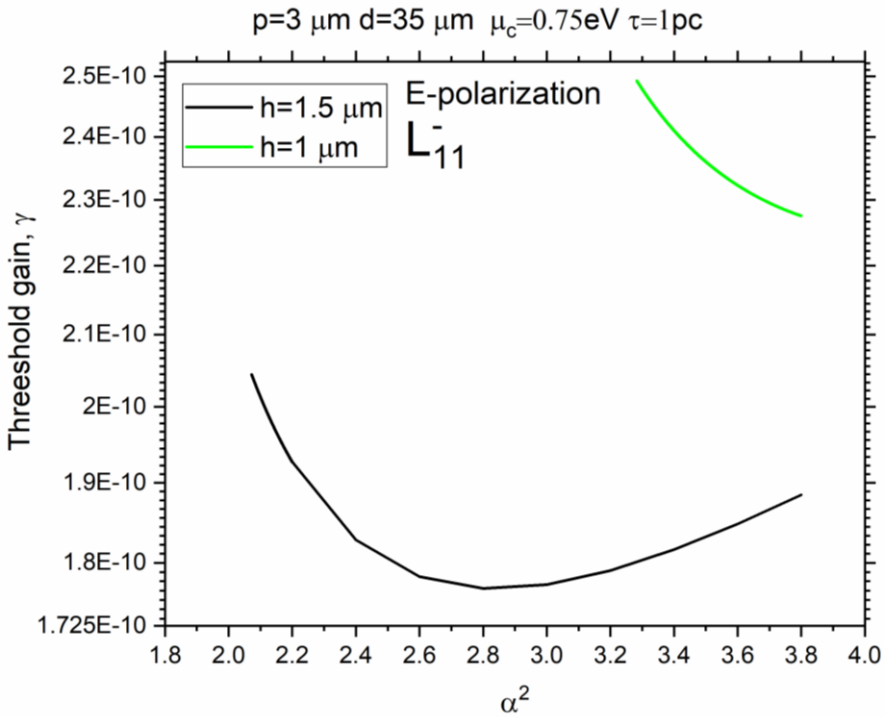

(b)

Figure 4.18. The same as in Fig. 4.17, however, for the *x*-odd LMs.

As visible, if the refractive index of the substrate gets down, the LM frequency grows until it reaches the RA frequency at the same value of the refractive index as the cut-off frequency of the "parent" guided wave, TM_1. The threshold varies little around 10^{-7} and 10^{-10}, respectively (this level is apparently determined by the losses in graphene) until it jumps up by an order in the very close vicinity of the RA.

Conclusions to Chapter 4

We have considered a mathematical model of the H and E-polarized natural modes of the laser built on infinite grating of graphene strips on active (i.e. made of the gain material) substrate, on the threshold of stationary light emission. This model lies entirely in the framework of the classical electromagnetics except the description of the graphene conductivity, which is borrowed from the quantum theory. The corresponding LEPs for the H- and E-polarized modes have been reduced to the determinantal equations. Similar to the wave-scattering problems, our treatment is based on the analytical inversion of the static part of the problems associated with grating in free space with the aid of the RHP and IDFT techniques, respectively. As a result, the matrices, which generate the determinantal equations, are of the Fredholm second kind. This provides a mathematical proof of the convergence of the characteristic numbers of the truncated determinantal equations to the sought-for eigenvalues if the matrix truncation order gets larger. Using the developed algorithms, we have computed the LEP eigenpairs, associated with various lasing modes of the micro or nanolaser shaped as graphene-strip grating on the gain substrate and discussed their characteristics.

In the H-polarization case, we have studied the plasmon modes, which are tunable in wide range with the aid of the chemical potential of graphene (which is proportional to DC bias). This tunability concerns both the PM frequencies and their Q-factors.

The lowest thresholds are found for the lattice modes, which exist in either polarization. The above presented results of LEP analysis, together with the accurate

study of the H- and E-polarized plane-wave scattering from the graphene strip grating on passive dielectric substrate (see Chapter 3), convincingly prove that the LMs (I) do not have “plasmonic” nature (as frequently assumed); instead, it they are caused by the periodicity, and (II) are mediated by the guided waves of the dielectric substrate or, in broader sense, the guided waves of the host medium. The former circumstance yields the main term in the LM frequency – this is the “parent” RA frequency. The latter circumstance yields the main term in the redshift from the RA frequency. In the wave scattering scenario, each LM generates a complex pole of the field as a function of the frequency, either on the physical (top) or non-physical sheet of the square-root Riemann surface; that pole can have ultra-small imaginary part (i.e. ultrahigh Q-factor). In the lasing mode threshold scenario, each LM can have ultralow threshold value of the material gain in the active region.

The results related to Chapter 4 were published as conference papers [A6, A7, A12].

CONCLUSIONS AD RECOMMENDATIONS

- We have considered the H and E-polarized plane wave scattering by an infinite grating of graphene strips on dielectric substrate

- Our treatment is based on the analytical inversion of the problem singular part with the aid of modified RHP technique and IDTF solution, respectively, and yields the Fredholm second kind matrix equations

- Convergence of the resulting numerical algorithm is guaranteed and has been demonstrated

- We have validated our code with the results of other works computed using another convergent algorithm

- Using this extremely fast and reliable numerical code, we have analyzed interplay of the resonances in the THz plane-wave scattering and absorption. Thanks to the tunability of the plasmon modes with the aid of graphene's chemical potential, controlled with electrostatic bias, the metasurface reflectivity can be manipulated in wide range. We have shown, for the first time, that the grating tunability is completely lost at the regimes of the electromagnetically induced transparency, caused by the excitation of the high-Q lattice-mode resonances. This effect should be taken into account when designing the THz and infrared circuit components.

- We have also considered, for the first time, the threshold conditions for the H and E-polarized lasing modes of infinite flat grating of graphene strips lying on gain-material substrate

- We have reduced the LEP eigenvalues, associated with lasing modes of the considered plasmonic nanolaser, to the determinantal equations generated by the Fredholm second kind matrix operators

- The lowest thresholds are found for the lattice modes, while the best tunability is demonstrated by the plasmon modes; besides, we found the substrate modes, which have very high thresholds.

REFERENCES

1. F. J. Garcia de Abajo, "Graphene plasmonics: challenges and opportunities," ACS Photonics, vol. 1, no. 3, pp.135-152, 2014.
2. T. Low and P. Avouris, “Graphene plasmonics for terahertz to mid-infrared applications,” ACS Nano, vol. 8, no 2, pp. 1086-1101, 2014.
3. D. Rodrigo, O. Limaj, D. Janner, D. Etezadi, F. J. García de Abajo, V. Pruneri, and H. Altug, “Mid-infrared plasmonic biosensing with graphene,” Science, vol. 349, no 6244, pp. 165-168, 2015.
4. Z. Ullah, G. Witjaksono, I. Nawi, N. Tansu, M. Irfan Khattak, et al., “A review on the development of tunable graphene nanoantennas for terahertz optoelectronic and plasmonic applications,” Sensors, vol. 20, no 5, art. no 1401, 2020.
5. S. Shukla, S. Y. Kang, and S. Saxena, “Synthesis and patterning of graphene: Strategies and prospects,” Appl. Phys. Rev., vol. 6, no 2, art. no 021311, 2019.
6. S. Thongrattanasiri, F. H. L. Koppens, and F. J. G. De Abajo, “Complete optical absorption in periodically patterned graphene,” Phys. Rev. Lett., vol. 108, pp. 047401/5, 2012.
7. W. Fuscaldo, P. Burghignoli, P. Baccarelli, and A. Galli, “Efficient 2-D leaky-wave antenna configurations based on graphene metasurfaces,” Int. J. Microw. Wireless Techn., vol. 9, no 6, pp. 1293-1303, 2017.
8. D. Rodrigo, A. Tittl, O. Limaj, F. J. Garcia de Abajo, V. Pruneri, and H. Altug, “Double-layer graphene for enhanced tunable infrared plasmonics,” Light: Science Applicat., vol. 6, no. 6, art. no e16277, 2017.
9. Z. Xu, D. Wu, Y. Liu, C. Liu, Z. Yu, L. Yu, and H. Ye, "Design of a tunable ultra-broadband terahertz absorber based on multiple layers of graphene ribbons," Nanoscale Res. Lett., vol. 13, no 1, pp. 143, 2018.

10. J. Homola, “Surface plasmon resonance sensors for detection of chemical and biological species,” Chem. Rev., vol. 108, pp. 462–93, 2008.

11. P. Offermans, M.C. Schaafsma, S.R.K. Rodriguez, Y. Zhang, M. Crego-Calama, S.H. Brongersma, and J.G. Rivas, “Universal scaling of the figure of merit of plasmonic sensors,” ACS Nano, vol. 5, pp. 5151–5157, 2011.

12. O.V. Shapoval, “Comparison of refractive-index sensitivities of optical-mode resonances on a finite comb1like grating of silver nanostrips,” IEEE J. Quant. Electron., vol. 51, art. no 7200108, 2015.

13. B. Vasic, G. Isic, and R. Gajic, “Localized surface plasmon resonance in graphene ribbon arrays for sensing of dielectric environment at infrared frequencies,” J. Appl. Phys., vol. 113, pp. 013110, 2013.

14. O.V. Shapoval and A.I. Nosich, “Bulk refractive-index sensitivities of the THz-range plasmon resonances on a micro-size graphene strip," J. Phys. D: Appl. Phys., vol. 49, no 5, art. no 055105, 2016.

15. M. Kim, et al., “Ultra-compact integrated terahertz modulator based on a graphene metasurface,” Opt. Lett., vol. 46, no 3, pp. 605-608, 2021.

16. G. W. Hanson, “Dyadic Green’s functions and guided surface waves for a surface conductivity model of graphene,” J. Appl. Phys., vol. 103, pp. 064302, 2008.

17. M. Jablan, H. Buljan, and M. Soljacic, “Plasmonics in graphene at infrared frequencies,” Phys. Rev. B, vol. 80, art. no 245435, 2009.

18. A. Fallahi and J. Perruisseau-Carrier, “Design of tunable biperiodic graphene metasurfaces,” Phys. Rev. B, vol. 86, pp. 195408/9, 2012.

19. O. V. Shapoval, et al., "Integral equation analysis of plane wave scattering by coplanar graphene-strip gratings in the THz range," IEEE Trans. Terahertz Science Technol., vol. 3, no 5, pp. 666-673, 2013.

20. T. L. Zinenko, “Scattering and absorption of terahertz waves by a free-standing infinite grating of graphene strips: analytical regularization analysis,” J. Opt., vol. 17, no 5, pp. 055604/8, 2015.

21. V. Gerasik, M. S. Wartak, et al., “Free electromagnetic radiation from the graphene monolayer with spatially modulated conductivity in THz range,” Mod. Phys. Lett. B, vol. 30, pp. 1650185/9, 2016.

22. M.E. Kaliberda, L.M. Lytvynenko, and S.A. Pogarsky, “THz waves scattering by finite graphene strip grating embedded into dielectric slab,” IEEE J. Quantum Electronics, 56(1), art. no 8889383, 2020.

23. T. Oguzer, A. Altintas, and A. I. Nosich, "Focusing of THz waves with a microsize cylindrical reflector made of graphene in the free space," J. European Opt. Soc., vol. 13, art. no 16, 2017.

24. T. L. Zinenko, A. Matsushima and A. I. Nosich, "Surface-plasmon, grating-mode and slab-mode resonances in THz wave scattering by a graphene strip grating embedded into a dielectric slab," IEEE J. Sel. Top. Quant. Electron., vol. 23, no 4, art. no 4601809, 2017.

25. T.L. Zinenko, A. I. Nosich, and Y. Okuno, "Plane wave scattering and absorption by resistive-strip and dielectric-strip periodic gratings," IEEE Trans. Antennas Propagat., vol. 46, no 10, pp. 1498-1505, 1998.

26. S.-H. Kim, et al., “Broadband surface plasmon lasing in one-dimensional metallic gratings on semiconductor,” Sci. Rep., vol. 7, art. no 7907, 2017.

27. D. Rittenhouse, “An optical problem proposed by F. Hopkinson and solved,” J. Am. Phil. Soc., vol. 201, pp. 202–206, 1786.

28. R. W. Wood, “On a remarkable case of uneven distribution of light in a diffraction grating spectrum,” Phil. Mag., vol. 4, no 21, pp. 396-402, 1902.

29. Lord Rayleigh, “On the dynamical theory of gratings,” Proc. R. Soc. London, vol. A-79, pp. 399–416, 1907.

30. A. Maradudin, I. Simonsen, J. Polanco, and R. M. Fitzgerald, “Rayleigh and Wood anomalies in the diffraction of light from a perfectly conducting reflection grating,” J. Optics, vol. 18, art. no 024004, 2016.

31. A. Hessel and A. A. Oliner, “A new theory of Wood’s anomalies on optical gratings,” Appl. Opt., vol. 4, no 10, pp. 1275-1297, 1965.

32. V.P. Shestopalov, L.N. Litvinenko, S.A. Masalov, V.G. Sologub, Wave Diffraction from Gratings, Vyshcha Shkola Publ., Kharkiv, 1973.

33. V.P. Shestopalov, A.A. Kirileko, S.A. Masalov, Y.K. Sirenko, Resonance Scattering of Waves. Diffraction Gratings, Vyshcha Shkola Publ., Kharkiv, 1986.

34. V.P. Shestopalov, Y.K. Sirenko, Dynamic Theory of Gratings, Vyshcha Shkola Publ., Kharkiv, 1989.

35. R. Petit (Ed.), Electromagnetic Theory of Gratings, Springer, 1980.

36. H. Lamb, “On the reflection and transmission of electric waves by metallic grating,” Proc. London Math. Soc. vol. 29, no. 1, pp. 523–545, 1898.

37. V. G. Yampolsky, “Diffraction of a plane electromagnetic wave by an array of metallic strips,” Radio Eng. Electron. Phys., vol. 8, no 4, pp. 564-572, 1963.

38. A. Matsushima and T. Itakura, “Singular integral equation approach to plane wave diffraction by an infinite strip grating at oblique incidence,” J. Electromagn. Waves Applicat., vol. 4, no 6, pp. 505-51, 1990.

39. Z. S. Agranovich, V. A. Marchenko, and V. P. Shestopalov, “Diffraction of a plane electromagnetic wave from plane metallic lattices,” Sov. Phys. Techn. Phys., vol. 7, no 1, pp. 277-286, 1962.

40. V.V. Panasyuk, M.P. Savruk, and Z.T. Nazarchuk, Singular Integral Equations Method in Two-Dimensional Diffraction Problems, Naukova Dumka, Kyiv, 1984.

41. Y. V. Gandel and T. S. Polyanskaya, "Justification of a numerical method for solving systems of singular integral equations in diffraction grating problems," Diff. Equations, vol. 39, no 9, pp. 1295–1307, 2003.

42. J. L. Volakis, Y. C. Lin, and H. Anastassiou, “TE characterization of resistive strip gratings on a dielectric slab using single-mode expansion,” IEE Trans. Antennas Propagat., vol. 42, no. 2, pp. 205–213, 1994.

43. T. L. Zinenko, A. Matsushima, and Y. Okuno, “Scattering and absorption of electromagnetic plane waves by a multilayered resistive strip grating embedded in a dielectric slab,” Trans. IEICE Electron., vol. E82-C, no. 12, pp. 2255–2264, 1999.

44. T. L. Zinenko and A. I. Nosich, “Plane wave scattering and absorption by flat gratings of impedance strips,” IEEE Trans. Antennas Propagat., vol. 54, no 7, pp. 2088-2095, 2006

45. T. L. Zinenko, M. Marciniak, and A. I. Nosich, “Accurate analysis of light scattering and absorption by an infinite flat grating of thin silver nanostrips in free space using the method of analytical regularization,” IEEE J. Sel. Top. Quant. Electron., vol. 19, no 3, art. no 9000108, 2013.

46. O. A. Tretyakov and V. P. Shestopalov, “Electromagnetic wave diffraction by a plane metal grating lying on a dielectric layer,” Izv. VUZov Radiofizika, vol. 6, no 2, pp. 353- 363, 1963.

47. A. Matsushima, T. Fujimura, and T. Itakura, “Scattering of an arbitrary plane wave by an infinite strip grating loaded with a pair of dielectric slabs,” J. Electromagn. Waves Applicat., vol. 7, no 6, pp. 791-809, 1993.

48. A. Matsushima and T. Itakura, “Polarization diplexing by a double strip grating loaded with a pair of dielectric slabs,” IEICE Trans. Electron., vol. E76-C, no 6, pp. 486-495, 1993.

49. Y. K. Cho and U. H. Cho, “TM-polarized electromagnetic scattering from a periodic strip array on a grounded dielectric,” Microwave Opt. Technol. Lett., vol. 11, no 1, pp. 41-45, 1996.

50. F. Medina, F. Mesa, and D. C. Skigin, “Extraordinary transmission through arrays of slits: a circuit theory model,” IEEE Trans. Microwave Theory Techn., vol. 58, no 1, pp. 105-115, 2010.

51. R. Rodriguez-Berral, F. Medina, F. Mesa, and M. Garcia-Vigueras, “Quasi-analytical modeling of transmission/reflection in strip/slit gratings loaded with dielectric slabs,” IEEE Trans. Microwave Theory Techn., vol. 60, no. 3, pp. 405–418, 2012.

52. R.-B. Hwang, “A theoretical design of evanescent wave biosensors based on gate-controlled graphene surface plasmon resonance,” Sci. Rep., vol. 11, art. no 1999, 2021.

53. S. B. Panin and A. Y. Poyedinchuk, “Electromagnetic wave diffraction by a grating with a chiral layer,” Radiophys. Quant. Electron., vol. 45, no 8, pp. 629-639, 2002.

54. S. B. Panin, E. D. Vinogradova, A. Y. Poyedinchuk, and S. I. Tarapov, “Resonant diffraction from a grating on a paramagnetic layer with frequency dispersion,” Progr. In Electromagn. Res., vol. 6, pp. 185-189, 2009.

55. A. Y. Nikitin, F. Guinea, F. J. Garcia-Vidal and L. Martin-Moreno, “Surface plasmon enhanced absorption and suppressed transmission in periodic arrays of graphene ribbons,” Phys. Rev. B, vol. 85, art. no 081405(R), 2012.

56. X. Du, I. Skachko, A. Barker, and E. Y. Andrei, “Approaching ballistic transport in suspended graphene,” Nature Immunology, vol. 3, pp. 491 – 495, 2008.

57. J. Čtyroký, J. Petráček, P. Kwiecien, I. Richter, and V. Kuzmiak, "Graphene on an optical waveguide: comparison of simulation approaches," Opt. Quant. Electron., vol. 52, no 3, art. no 149, 2020.

58. M. E. Kaliberda, L. M. Lytvynenko, and S. A. Pogarsky, "Modeling of graphene planar grating in the THz range by the method of singular integral equations," Frequenz, vol. 72, pp. 277-284, 2018.

59. M.E. Kaliberda, L.M. Lytvynenko, and S.A. Pogarsky, “Singular integral equations analysis of THz wave scattering by an infinite graphene strip grating embedded into a grounded dielectric slab,” J. Opt. Soc. Am. A, 36(10), pp. 1787–1794, 2019.

60. T. L. Zinenko, A. Matsushima, and A. I. Nosich, “Terahertz range resonances of metasurface based on double grating of microsize graphene strips inside dielectric slab,” Proc. Royal Society A, vol. 476, no 2240, art. no 20200173, 2020.

61. V. Lomakin and E. Michielssen, “Transmission of transient plane waves through perfect electrically conducting plates perforated by periodic arrays of subwavelength holes,” IEEE Trans. Antennas Propag., vol. 54, no 3, pp. 970–984, 2006.

62. V. O. Byelobrov, T. L. Zinenko, K. Kobayashi, and A. I. Nosich, “Periodicity matters: grating or lattice resonances in the scattering by sparse arrays of sub-wavelength strips and wires,” IEEE Antennas Propagat. Mag., vol. 57, no 6, pp. 34-45, 2015.

63. V. G. Kravets, A. V. Kabashin, W. L. Barnes, and A. N. Grigorenko, “Plasmonic surface lattice resonances: a review of properties and applications,” Chem. Rev., vol. 118, pp. 5912-5951, 2018.

64. A. D. Utyushev, V.I. Zakomirnyi, and I. L. Rasskazov, “Collective lattice resonances: plasmonics and beyond,” Reviews in Physics, vol. 6, art. no 100051, 2021.

65. V. I. Belotelov, et al., “Enhanced magneto-optical effects in magneto-plasmonic crystals,” Nature Nanotechnol., vol. 6, pp. 370-376, 2011.

66. V. E. Babicheva and A. B. Evlyukhin, "Resonant lattice Kerker effect in metasurfaces with electric and magnetic optical responses,” Laser Photon. Rev., vol. 11, no 6, art. no 1700132, 2017.

67. V. V. Yachin, et al., “Resonance enhancement of Faraday rotation in double-periodic gyromagnetic layers analyzed by the method of integral functional," J. Opt. Soc. Am. B, vol. 35, pp. 851-860, 2018.

68. L. I. Ivzhenko, et al., “Experimental observation of tunable Wood type resonances in an all-ferrodielectric periodical metasurface,” Opt. Lett., vo. 45, no 19, pp. 5514-5517, 2020.

69. A. I. Nosich, “Method of analytical regularization in computational photonics,” Radio Sci., vol. 51, no 8, pp. 1421-1430, 2016.

70. M. Lucido, K. Kobayashi, F. Medina, A. I. Nosich, E. D. Vinogradova, "Guest Editorial: Method of analytical regularisation for new frontiers of applied electromagnetics," IET Microwaves, Antennas and Propagation, vol. 15, no 10, pp. 1127-1132, 2021

71. N. Bonod, J. Neauport, " Diffraction gratings: from principles to applications in high intensity lasers," Advances in Optics and Photonics, 2016, 8 (1), pp.156-199.

72. C. Deeb and J.-L. Pelouard, “Plasmon lasers: coherent nanoscopic light sources,” Phys. Chem. Chem. Phys., vol. 19, 4, pp. 29731–29741, 2017.

73. A. Yang, et al., “Real-time tunable lasing from plasmonic nanocavity arrays,” Nat. Communic., vol. 6, art. no 6939, 2015.

74. M. Ross, et al., “Optical properties of 1, 2, and 3-D arrays of plasmonic nanostructures,” J. Phys. Chem. C, vo. 120, pp. 816−830, 2016.

75. J.-P. Martikainen, et al., “Modelling lasing in plasmonic nanoparticle arrays,” J. Opt., vol. 18, art. no 024006, 2016.

76. T. B. Hoang, et al., “Millimeter-scale spatial coherence from a plasmon laser,” ACS Nano Lett., vol. 17, pp. 6690-6695, 2017.

77. W. Wang, et al., “The rich photonic world of plasmonic nanoparticle arrays,” Materials Today, vol. 21, no 3 pp. 303-314, 2018.

78. R. Li, et al. “Plasmon nanolasing with aluminum nanoparticle arrays, J. Opt. Soc. Am. B, vol. 36, no 7, pp. E-104-E111, 2019.

79. K. Xu, et al., “Compact unidirectional laser based on all-dielectric metasurface with high quality factor,” vol. 13, art. no 1500109, 2021

80. O. V. Shapoval and A. I. Nosich, “Finite gratings of many thin silver nanostrips: optical resonances and role of periodicity,” AIP Advances, vol. 3, no 4, art. no 042120, 2013.

81. D. M. Natarov, et al., “Effect of periodicity in the resonant scattering of light by finite sparse configurations of many silver nanowires,” Plasmonics, vol. 9, no 2, pp. 389-407, 2014.

82. D. M. Natarov, et al., “Seeing the order in a mess: optical signature of periodicity in a cloud of plasmonic nanowires,” Opt. Exp., vol. 22, no 23, pp. 28190–28198, 2014.

83. V. Apalkov and M. I. Stockman, “Proposed graphene nanospaser,” Light: Science Applications, vol. 3, art. no e191, 2014.

84. W. Du, et al., “Nanolasers based on 2D materials,” Laser Photon. Rev., art. no 2000271, 2020.

85. M. Cuevas and R. Depine, “Theoretical study of a low–energy spherical core–shell spaser,” Proc. IEEE Bienn. Congr. Argentina (ARGENCON-2020), 2020.

86. L. Prelat, et al., "Spaser and optical amplification conditions in graphene-coated active wires," J. Opt. Soc. Am B, pp. 2118-2126, 2021.

87. D. O. Herasymova, et al., “Threshold conditions for transversal modes of tunable plasmonic nanolasers shaped as single and twin graphene-covered circular quantum wires,” IOP Nanotechnology, vol. 33, no 49, art. no 495001, 2022.

88. E. I. Smotrova, et al., “Optical theorem helps understand thresholds of lasing in microcavities with active regions,” IEEE J. Quant. Electron., vol. 47, no 1, pp. 20-30, 2011.

89. V. O. Byelobrov and A. I. Nosich, “Mathematical analysis of the lasing eigenvalue problem for the optical modes in a layered dielectric cavity with a quantum well and distributed Bragg reflectors,” Opt. Quant. Electron., vol. 39, no 10-11, pp. 927-937, 2007.

90. E.I. Smotrova, A.I. Nosich, T. Benson, P. Sewell, "Cold-cavity thresholds of microdisks with uniform and non-uniform gain: quasi-3D modeling with accurate 2D analysis,” IEEE J. Sel. Topics Quant. Electron., vol. 11, no 5, pp. 1135-1142, 2005.

91. E.I. Smotrova, A.I. Nosich, T. Benson, P. Sewell, "Optical coupling of whispering-gallery modes in two identical microdisks and its effect on photonic molecule lasing," IEEE J. Sel. Topics Quant. Electron., vol. 12, no 1, pp. 78-85, 2006.

92. E.I. Smotrova, A.I. Nosich, T.M. Benson, P. Sewell, "Threshold reduction in a cyclic photonic molecule laser composed of identical microdisks with whispering-gallery modes," Optics Letters, vol. 31, no 7, pp. 921-923, 2006.

93. E.I. Smotrova, et al., "Spectra, thresholds and modal fields of a kite-shaped microcavity laser," J. Opt. Soc. Am. B, vol. 30, no 6, pp. 1732-1742, 2013.

94. A. O. Spiridonov, et al., "Why elliptic microcavity lasers emit light on bow-tie-like modes instead of whispering-gallery-like modes," Optics Communicat., vol. 439, pp. 112-117, 2019.

95. V. O. Byelobrov, et al., "Low-threshold lasing eigenmodes of an infinite periodic chain of quantum wires," Optics Letters, vol. 35, no 21, pp. 3634-3636, 2010.

96. V. O. Byelobrov, T. M. Benson, and A. I. Nosich, "Binary grating of sub-wavelength silver and quantum wires as a photonic-plasmonic lasing platform with nanoscale elements," IEEE J. Sel. Top. Quant. Electron., vol. 18, no 6, pp. 1839-1846, 2012.

97. D. M. Natarov, et al., "Electromagnetic analysis of the lasing thresholds of plasmon modes of a silver tube nanolaser with active core and active shell," Beilstein J. Nanotechnol., vol. 10, pp. 294-304, 2019.

98. O. V. Shapoval, et al., "Electromagnetic engineering of a single-mode nanolaser on a metal plasmonic strip placed into a circular quantum wire," IEEE J. Sel. Top. Quant. Electron., vol. 23, art. 1501609, 2017.

99. S. Nojima, "Theoretical analysis of feedback mechanisms of two-dimensional finite-sized photonic-crystal lasers," J. Appl. Phys., vol. 98, no. 4, art. no 043102, 2005.

100. A. Mock, “First principles derivation of microcavity semiconductor laser threshold condition and its application to FDTD active cavity modeling,” J. Opt. Soc. Amer. B, vol. 27, no 11, pp. 2262–2272, 2010.

101. S. W. Chang, “Confinement factors and modal volumes of micro- and nanocavities invariant to integration regions,” IEEE J. Sel. Top. Quant. Electron., vol. 18, no 6, pp. 1771–1780, 2012.

102. Y. Huang and Y. Y. Lu, "Efficient method for lasing eigenvalue problems of periodic structures," J. Mod. Opt., vol. 61, no 5, pp. 390–396, 2014.

103. H.-Q. Yu, S.-M. Jiang, and D.-J. Wu, “Efficient surface plasmon amplification in gain-assisted silver nanotubes and associated dimers,” J. Appl. Phys., vol. 117, art. no 153101, 2015.

104. N.L. Tsitsas, C.A. Valagiannopoulos, and A.I. Nosich, “Excitation of guided waves of a lossless dielectric slab by an E-polarized complex-source-point beam,” IEEE Trans. Antennas Propagat., vol. 67, no 8, pp. 5532-5543, 2019.

105. K. T. Carron, et al., “Resonances of two-dimensional particle gratings in surface-enhanced Raman scattering,” J. Opt. Soc. Am. B, vol. 3, no 3, pp. 430-440, 1986.

106. S. Peng and G. M. Morris, "Resonant scattering from two-dimensional gratings," J. Opt. Soc. Am. A, vol. 13, no 5, pp. 993-1005, 1996.

107. A. A. Oliner, "On blindness in large phased arrays," Alta Frequenza, vol. 38, Special Issue, pp. 221-228, 1969.

108. D. M. Pozar, D. H., Schaubert, "Scan blindness in infinite phased arrays of printed dipoles," IEEE Trans. Antennas Propagat., vol.32, no 6, pp. 602-610, 1984.

109. H. Koo and S. Nam, “Mechanism and elimination of scan blindness in a T-printed dipole array,” IEEE Trans. Antennas Propagat., vol. 68, no 1, pp. 242-253, 2020.

110. A. Ludvig-Osipov and B. L. G. Jonsson, “Stored energies and Q-factor of two-dimensionally periodic antenna arrays,” IEEE Trans. Antennas Propagat., vol. 68, no 8, pp. 5989-6002, 2020.

111. J. S. Bellucci, A. Bendziak, O. Vernyhor, and V. M. Fitio, "Phenomenon of electromagnetic field resonance in metal and dielectric gratings and its possible practical applications," Condensed Matter, vol. 5, no 3, art. no 49, 2020.

112. S. V. Dukhopelnykov, R. Sauleau, and A. I. Nosich, “Integral equation analysis of terahertz backscattering from circular dielectric rod with partial graphene cover,” IEEE J. Quant. Electron., vol. 56, no 6, art. no 8500208, 2020.

113. R. S. Varga, “Geršgorin and His Circles” (Springer Series in Computational Mathematics), vol. 36. Berlin, Germany: Springer, 2004.

114. S. Freer, M. Camacho, S. A. Kuznetsov, R. R. Boix, M. Beruete, and M. Navarro-Cia, “Revealing the underlying mechanisms behind TE extraordinary THz transmission,” Photonics Research, vol. 8, no 4, pp. 430-439, 2020.

115. C. L. Garrido and M. A. G. Martinez “Classical analog of electromagnetically induced transparency,” Am. J. Phys., vol. 70, no 1, pp. 37–41, 2002.

116. Y.-C. Liu, B.-B. Li, and Y.-F. Xiao, "Electromagnetically induced transparency in optical microcavities," Nanophotonics, vol. 6, no 5, pp. 789–811, 2017.

117. S. Steinberg, “Meromorphic families of compact operators,” Arch. Rational Mech. Analysis, vol. 31, pp. 372–379,1968.

118. O. Karma, “Approximation in eigenvalue problems for holomorphic Fredholm operator function. II. Convergence rate,” Numerical Functional Analysis and Optimization, vol. 17, no 3-4, pp. 389–408, 1996.

119. A. O. Spiridonov and E. M. Karchevskii, “Residual inverse iteration for the lasing eigenvalue problem,” Proc. Int. Conf. Mathematical Methods in Electromagnetic Theory (MMET*2018), Kyiv, 2018, pp. 129-131, 2018.

120. A. Neumaier, "Residual inverse iteration for the nonlinear eigenvalue problem." SIAM J. Numeric. Analysis, vol. 22, no 2, pp. 914-923, 1985.

APPENDIX A

LIST OF PUBLICATIONS RELATED TO THESIS

Papers in international journals

[A.1] F.O. Yevtushenko, S.V. Dukhopelnykov, Y.G. Rapoport, T.L. Zinenko, R. Sauleau, A.I. Nosich, "Tunability of non-plasmon resonances in the E-polarized terahertz wave scattering from microsize graphene strip-on-substrate grating," Optical Materials Express, vol. 13, vol. 13, no 8, pp. 2274-2287, 2023. **(Q-2)** https://doi.org/10.1364/OME.496037

[A.2] F.O. Yevtushenko, S.V. Dukhopelnykov, Y.G. Rapoport, T.L. Zinenko, A.I. Nosich, “Spoiling of tunability of on-substrate graphene strip grating due to lattice-mode-induced transparency,” Royal Society of Chemistry Advances, vol. 12, pp. 4589–4594, 2022. **(Q-2)** https://doi.org/10.1039/d1ra08287f

[A.3] F.O. Yevtushenko, S.V. Dukhopelnykov, Y.G. Rapoport, T.L. Zinenko, " Electromagnetic characterization of tuneable graphene-strips-on-substrate metasurface over entire THz range: Analytical regularization and natural-mode resonance interplay," IET Microwaves, Antennas and Propagation, vol. 15, 2021 **(Q-2)** https://doi.org/10.1049/mia2.12158

[A.4] F.O. Yevtushenko, S.V. Dukhopelnykov, T.L. Zinenko, "E-polarized plane-wave scattering from a PEC strip grating on a dielectric substrate: analytical regularization and lattice-mode resonances," Journal of Electromagnetic Waves and Applications, vol. 35, no 10, pp. 1388–1405, 2021. **(Q-3)** https://doi.org/10.1080/09205071.2021.1887001

[A.5] F.O. Yevtushenko, S.V. Dukhopelnykov, and A.I. Nosich, "Plane-wave scattering by a PEC strip grating on top of a dielectric substrate: analytical regularization based on

the Riemann-Hilbert Problem solution," Journal of Electromagnetic Waves and Applications, vol. 33, no 4, pp. 483-499, 2020. **(Q-3)**
https://doi.org/10.1080/09205071.2020.1722258

Papers in proceedings of international conferences, indexed in Scopus

[A.6] F.O. Yevtushenko, "Threshold analysis for the modes of microsize graphene strip grating laser," Proc. Int. Conference on Applied Electromagnetics and Communications (ICECOM-2023), Dubrovnik, 2023, pp.

[A.7] F.O. Yevtushenko, S.V. Dukhopelnykov, "Emission frequencies and thresholds for microsize graphene strip grating on gain substrate," Proc. European Microwave Conference (EuMC-2023), Berlin, 2023, pp. 548-55.

[A.8] F. O. Yevtushenko, "Resonance scattering and absorption of the E-polarized plane wave by graphene strip on-substrate grating" International Conference on Electronics and Nanotechnology (ELNANO-2022), Kyiv, 2022, pp. 196-201.

[A.9] F. O. Yevtushenko, S. V. Dukhopelnykov, "Resonances in the E-polarized terahertz wave scattering and absorption by a graphene strip on-substrate grating" Proc. European Microwave Conference (EuMC-2022), Milan, 2022, pp. 736-739.

[A.10] F. O. Yevtushenko, "Role of substrate in the H-polarized terahertz wave scattering and absorption by a graphene strip on-substrate grating," Proc. Int. Conf. EEE International Conference on Information and Telecommunication Technologies and Radio Electronics, Proceedings, (UkrMiCo 2021), Kyiv, 2021, pp. 279-282.

[A.11] F. O. Yevtushenko, "H-polarized terahertz wave scattering from on-substrate graphene strip grating: electromagnetically induced transparency," Proc. Int. Conference Microwaves, Communications, Antennas, and Electronic Systems (COMCAS-2021), Tel Aviv, 2021, art. no 21483684.

[A.12] F. O. Yevtushenko, S. V. Dukhopelnykov, and T. L. Zinenko, "Basic equations of the lasing eigenvalue problem for a graphene strip on-substrate grating, H-

polarization," Proc. IEEE Ukrainian Conference Electrical Computer Eng. (UKRCON-2021), Lviv, 2021.

[A.13] F. O. Yevtushenko, "Convergence study for the method of analytical regularization applied to the E-plane-wave scattering from a PEC strip grating on a dielectric substrate," Proc. Int. Conference Ukrainian Microwave Week (UKRMW-2020), Kharkiv, 2020, pp. 504-506.

[A.14] F. O. Yevtushenko, S. V. Dukhopelnykov, and T. L. Zinenko, “Fano-shape lattice-mode resonances and near fields in the E-polarized wave scattering by a PEC strip grating on a dielectric substrate,” Proc. Int. Conference Ukrainian Microwave Week (UKRMW-2020), Kharkiv, 2020, pp. 516-519.

[A.15] F. O. Yevtushenko and S. V. Dukhopelnykov, "Method of analytical regularization based on the static part inversion in the H-wave scattering by a PEC strip grating on top of a dielectric substrate," Proc. Int. Conference Microwaves, Communications, Antennas, and Electronic Systems (COMCAS-2019), Tel Aviv, 2019, art. no 8958263.

[A.16] F. O. Yevtushenko, S.V. Dukhopelnykov, and A. I. Nosich, "Plane-wave scattering by a PEC strip grating on top of a dielectric substrate: basic equations, regularization, and convergence," Proc. IEEE Ukrainian Conference Electrical Computer Eng. (UKRCON-2019), Lviv, 2019, pp. 797–801.